IMAGING NEURAL CIRCUITS VIA TWO-PHOTON-EXCITED FLUORESCENCE AND SECOND HARMONIC GENERATION MICROSCOPY

A Dissertation

Presented to the Faculty of the Graduate School

of Cornell University

in Partial Fulfillment of the Requirements for the Degree of

Doctor of Philosophy

by

Chun Hay Alex Kwan

August 2009

IMAGING NEURAL CIRCUITS VIA TWO-PHOTON-EXCITED FLUORESCENCE AND SECOND HARMONIC GENERATION MICROSCOPY

Chun Hay Alex Kwan, Ph.D.

Cornell University 2009

A functional neural circuit depends on multiple layers of complexity, from the cellular-level challenge of integrating synaptic inputs to the systems-level problem of deciphering spike patterns. A complete understanding of neural circuits cannot come from a single experimental approach, although laser-scanning microscopy methods promise new advances because optical emissions can potentially provide different kinds of information. As part of this Dissertation, I have developed nonlinear optical methods based on two-photon-excited fluorescence and second harmonic generation that reveal various structural and functional aspects of neural circuits.

Microtubules are the "molecular highways" within neurons and act as the substrate for intracellular trafficking. The polarity of microtubules determines the directions and speeds of cargo-carrying molecular motors. Using second harmonic generation as an optical probe of non-centrosymmetric structures, polarized microtubule arrays were observed within axons and mature apical dendrites, but not within basal and oblique dendrites. This microtubule organization in native brain tissues is age-dependent and different from what is known for dissociated neuronal cultures.

In addition to second harmonic generation, some biological molecules can emit autofluorescence. In transgenic Alzheimer's disease mouse models, both types of intrinsic optical emissions were observed at senile plaques. The utility of these spectrally broad but relatively weak signals was demonstrated by investigating the morphology of polarized microtubule arrays near senile plaques. The appearance, length, and density of

neuronal microtubule arrays are normal even in the presence of pathological lesions, suggesting that apical dendrites may be more tolerant to pathological mechanisms compared to smaller neurites.

Recording calcium transients with fluorescent indicator dyes is an indirect method to simultaneously measure spiking activity in many neurons. Applying two-photon calcium imaging to neonatal mouse spinal cords, one type of excitatory interneuron, defined by the transcription factor Hb9, was found to be fictive locomotion-related. However, these interneurons are not likely to be the rhythm generating kernel for the spinal locomotor circuit because the onset of their activity lags behind the onset of the ipsilateral motor output. Moreover, these interneurons show sparse, uncoordinated activity and may be important for initiating episodic fictive locomotor activity because they are most active immediately following the applied stimuli.

BIOGRAPHICAL SKETCH

Chun Hay Alex Kwan was born on November 23, 1979 in Hong Kong. As a kid, Alex was not the typical budding scientist but instead spent his time like the other kids: reading martial arts serials and playing Nintendo Game Boy. At the age of twelve, Alex immigrated with his family to beautiful British Columbia, Canada. He received an entrance scholarship at the neighboring Simon Fraser University and began training as a video game programmer in the Engineering Science program in 1998. Quickly realizing that game programming is not the same as game playing, he started exploring other career options by spending semesters abroad, initially at Lund University, Sweden as an exchange student and then at Ottawa, Canada and at Villach, Austria as an intern. While waiting for the industry to recover from the dot-com bubble, Alex and his future wife Judy were admitted into Cornell University's Applied Physics doctoral program in 2003. At Cornell, he worked briefly at the Synchrotron and in a low-temperature physics group before serendipitous events led him to study in the laboratory of Watt W. Webb. There, Alex had a crash course in modern biology and started using fancy microscopes to look at brain tissues, which he found to contain remarkable details and mysterious organizational principles. Soon Alex was reading more and more about the brain until one day he realized that it has become his passion. As his friend Ken said, Alex may be "leaving the dark side and joining him in studying the big questions of the day." Alex expects to graduate in 2009 and then continue research as a postdoctoral scholar.

For my parents - who always support their child's choices.

ACKNOWLEDGEMENTS

I thank my mentor, Prof. Watt W. Webb, for his constant encouragement over the last five years. Among his many positive qualities, I was most impressed by his appreciation for all flavors of science. Scientific collaborations are common for the Webb group; they are not for convenience, but people work together to seek greater knowledge. Talking with Prof. Webb is a pleasure because he always shares an active interest in scientific problems that I am working on. This is remarkable because lab members work on topics ranging from membrane biophysics to protein folding and from neurobiology to optical instrumentation. I am sincerely striving to develop a similar kind of scientific zeal and curiosity.

For the last few years, Prof. Ronald Harris-Warrick has constantly provided scientific and career advices. My time with him and his lab members, in particular with Shelby Dietz, Guisheng Zhong and Lola Kadiri, has pushed me to think about the biology while doing experiments. I am very grateful for the opportunity to participate in many of his group meetings and events. I also appreciate help from other committee members, Profs. Joe Fetcho, Joel Brock, and especially Prof. Alex Gaeta, whose diligent work in digging out my missing graduate school application forms late in the recruiting season was the reason why I could come to Cornell.

It was my luck to be part of the Webb group in an exciting time for research. Coffee trips with Jesse McMullen started with the Gimme! truck before Mannible became our usual spot. Science is the usual conversation topic but often his sailing stories would take priority. It is always fun to bug Huimin Chen about the awesome-ness of FCS. Becky Williams and Warren Zipfel had been my go-to gurus for anything lab-related from aligning the legendary Bio-Rad MRC-600 to taking out the the red-bag trash. Moreover, they lent the coffee roaster that officially qualifies me as a coffee snob, one of my proud achievements while at Ithaca. My writing has improved greatly by learning from

Mark Williams' edits. Early in my studies, Dan Dombeck and Sally Kim were the resident geniuses who showed me the ropes. Their dedication to research has been a great example, which I try hard to emulate. I also thank Jie Yao, Elaine Farkas, Huizhong Xu, Lisa Toth, and many others for the good company.

My life in Ithaca was infinitely enhanced by the daily crosswords sessions at lunch, which could not be completed (literally) without the help of Michael Durst, Sara Maccagnano-Zacher, and Jen Lee. I'm sorry, Mike, for always packing lunch and never going to Louie's. Three years living in shabby graduate housing made me realize that Norimasa Yoshimizu is the best roommate that I can have. The Applied Physics and Engineering Society (APES) intramural softball was a blast, especially on those rare occasions when I got a hit. Finally, it's been fun going to the Nine's, before we found out their pizzas use cheeses, with people from David Muller's group.

Judy Cha and I came to Cornell together after three years in Vancouver and then married in Ithaca after another four years. In many ways, our time together has intertwined with our graduate student lives, so we will have fond memories of Ithaca and Cornell. Whereas I am always too serious, Judy balances the mood by being her silly self and bringing joy every day. I am also thankful that she, as a fellow student, can understand the ups and downs of graduate school.

Finally, I thank my family including my dad Kei-Ching Alan Kwan, my mom Mui-Lee Anissa Kwong, my sister Angie and my grandparents. Asian parents often tend to put pressure on their children by deciding the future for them, but my parents were different. They let me choose and then always supported my decisions whole-heartedly, even when things got tough. Thank you for supporting me for many years.

Collaborators

Chapter 2. Dan Dombeck helped me to start the initial experiments and showed me how to image SHG from microtubules. Karl Kasischke and Harshad Vishwasrao taught me how to prepare brain slices. Advice from Warren Zipfel on photon counting and Rebecca Williams on numerical simulation of SHG were essential for detecting and interpreting the weak SHG emissions. Pam Gordnier and Sally Kim shared with me their cell culture experience and helped me in growing dissociated hippocampal cultures.

Chapter 3. Gunnar Gouras and Karen Duff kindly provided the Alzheimer's disease mouse models. Huizhong Xu helped me in setting up the spectrometer. Valerie Anderson supplied amyloid fibrils such that I could check for optical emissions from in vitro aggregations.

Chapter 4. This research was done in close collaboration with Shelby Dietz, who did the intracellular recordings and participated in the imaging experiments. Ronald Harris-Warrick has been the main motivator behind this research. Manuel Diaz-Rios taught me how to make the in vitro spinal cord preparation. Dan Dombeck showed me how to bulk-load with AM-ester fluorescent calcium indicators.

Chapter 5. Ronald Harris-Warrick, Rebecca Williams, Warren Zipfel, and Mark Williams provided valuable comments to the text of this Chapter.

TABLE OF CONTENTS

LIST OF TABLES

LIST OF FIGURES

LIST OF ABBREVIATIONS

5-HT, serotonin

ACSF, artificial cerebrospinal fluid

AD, Alzheimer's disease

AM-ester, acetoxymethyl-ester

AOD, acoustic-optical deflectors

APP(Swe), amyloid precursor protein (with the Swedish mutation)

CA1, *Cornu Ammonis* area 1 of the hippocampus

CA3, *Cornu Ammonis* area 3 of the hippocampus

CPG, central pattern generator

DA, dopamine

DMSO, dimethyl sulfoxide

f/b SHG, forward- over backward-directed second harmonic generation intensities

GFP, green fluorescent protein

HEPES, 4-(2-hydroxyethyl)-1-piperazineethanesulfonic acid

IN, interneuron

LacZ, β-galactosidase

MAP, microtubule-associated protein

MN, motoneurons

NA, numerical aperture

NAD(P)H, reduced nicotinamide adenine dinucleotide (phosphate)

NFT, neurofibrillary tangles

NMDA, N-methyl-D-aspartic acid

P#, postnatal day #

PBS, phosphate buffered saline

PMT, photomultiplier tube

PS1, presenilin 1

RBL, rat basophilic leukemia

SHG, second harmonic generation

TPF, two-photon-excited fluorescence

TTX, tetrodotoxin

YFP, yellow fluorescent protein

CHAPTER 1

INTRODUCTION

Invented almost two decades ago [Denk et al., 1990], two-photon-excited fluorescence (TPF) microscopy and other nonlinear optical techniques have since been applied to many problems in biology, especially in the area of neuroscience. This Chapter will begin with a brief description of the technology and why it is especially suited for studying the brain. Specific applications of nonlinear optical microscopy that arose from my research will be presented in the following Chapters. Chapter 2 describes experiments using second harmonic generation (SHG) microscopy to map the distribution of polarized microtubule arrays in brain slices. This research is extended in Chapter 3 where the interaction between dendritic microtubules and senile plaques was studied in Alzheimer's disease (AD) mouse models. Chapter 4 focuses on using two-photon calcium imaging to characterize the activity of a set of genetically-defined interneurons within the mouse spinal locomotor network. The benefits and pitfalls of the two-photon calcium imaging approach are discussed in more detail in Chapter 5.

1.1 Two-photon-excited fluorescence and second harmonic generation

In fluorescence, a photon-emitting molecule, the "fluorophore," has multiple ground and excited states. Upon excitation by an impinging photon, an electron from the ground state may acquire enough energy to hop onto one of the excited states. A relatively quick relaxation process, e.g. through vibration, ensues such that the excited electron will move to the lowest excited state within $\approx$1 ps. This process is called "internal conversion" [Lakowicz, 1999]. When the electron falls from the lowest excited state to

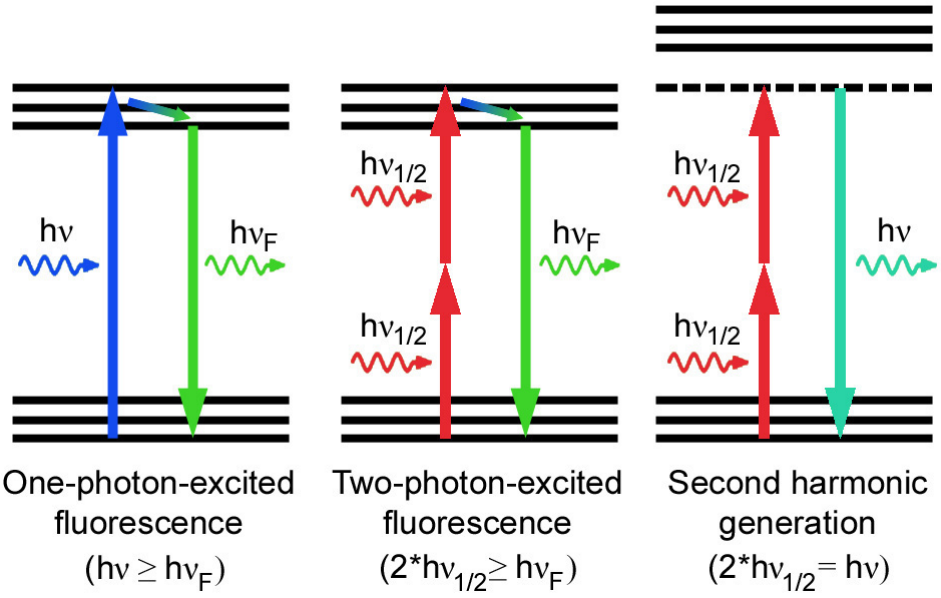

Figure 1.1: Jablonski diagrams for one-photon-excited fluorescence, two-photon-excited fluorescence and second harmonic generation.

the ground state, a fluorescence photon is emitted. Because of internal conversion, the wavelength of the fluorescence photon, c/υ_F, is longer than the exciting photon, c/υ. This is a simplified view of fluorescence generation and can be effectively displayed in a Jablonski diagram (Fig. 1.1).

In the case of TPF, two photons are absorbed by a fluorophore nearly simultaneously, within $\approx$ 1 fs, to excite an electron from the ground state to the excited state and ultimately generate fluorescence. The energies of the two exciting photons sum, therefore the energy of each exciting photon, $h\upsilon_{1/2}$, is half of the excitation energy required for the one-photon process, $h\upsilon$. This type of fluorescence generation leads to advantages when applied to optical microscopy, which are described further in Section 1.2.

SHG, unlike fluorescence, is not an absorption event. When two photons at wavelengths $h\upsilon_{1/2}$ interact with a hyperpolarizable molecule, a nonlinear optical process con-

verts them into one outgoing photon at wavelength $h\upsilon$ [Boyd, 2002]. The SHG process does not require the exciting photon's energy to match the excited state energy levels, although SHG occurring near absorption energies is more efficient. SHG is usually represented in Jablonski diagrams (Fig. 1.1) as an excitation onto a virtual excited state.

To implement a TPF and SHG microscope, there are a few practical issues. Because the probability of two simultaneously absorbed or interacting photons is low, the excitation intensity must be maximized and the fluorescence detection must be efficient. This is achieved by: 1) illuminating with a mode-locked infrared laser such that the peak excitation intensity is high compared to the time-averaged intensity [Wise, 2005]; 2) using high numerical aperture (NA) microscope objectives to collect scattered fluorescence photons [Oheim et al., 2001]; 3) maximizing detection by anticipating the emission's trajectory (e.g. non-descanned photomultiplier tubes (PMTs) for scattered TPF [Oheim et al., 2001] and forward-collecting PMTs for SHG [Zipfel et al., 2003a]). Nonlinear optical microscopes based on these design principles are shown in Fig. 1.2 and were used for experiments described in Chapters 2, 3, and 4. There is also substantial effort by other research groups to improve on this basic design, which is discussed in Chapter 5 and Appendix E.

1.2 Why use nonlinear microscopy to study the brain?

Imaging the brain is challenging because mammalian brain cells, neurons and glial cells, have small cell bodies (diameter of ≈5-20μm) and long, slender cellular processes such as axons and dendrites. Moreover, many interesting neural computation occurs in deeper brain regions, so imaging must probe deeper than the superficial volume of the highly scattering brain tissues. These challenges explain why neuroscientists are early adopters

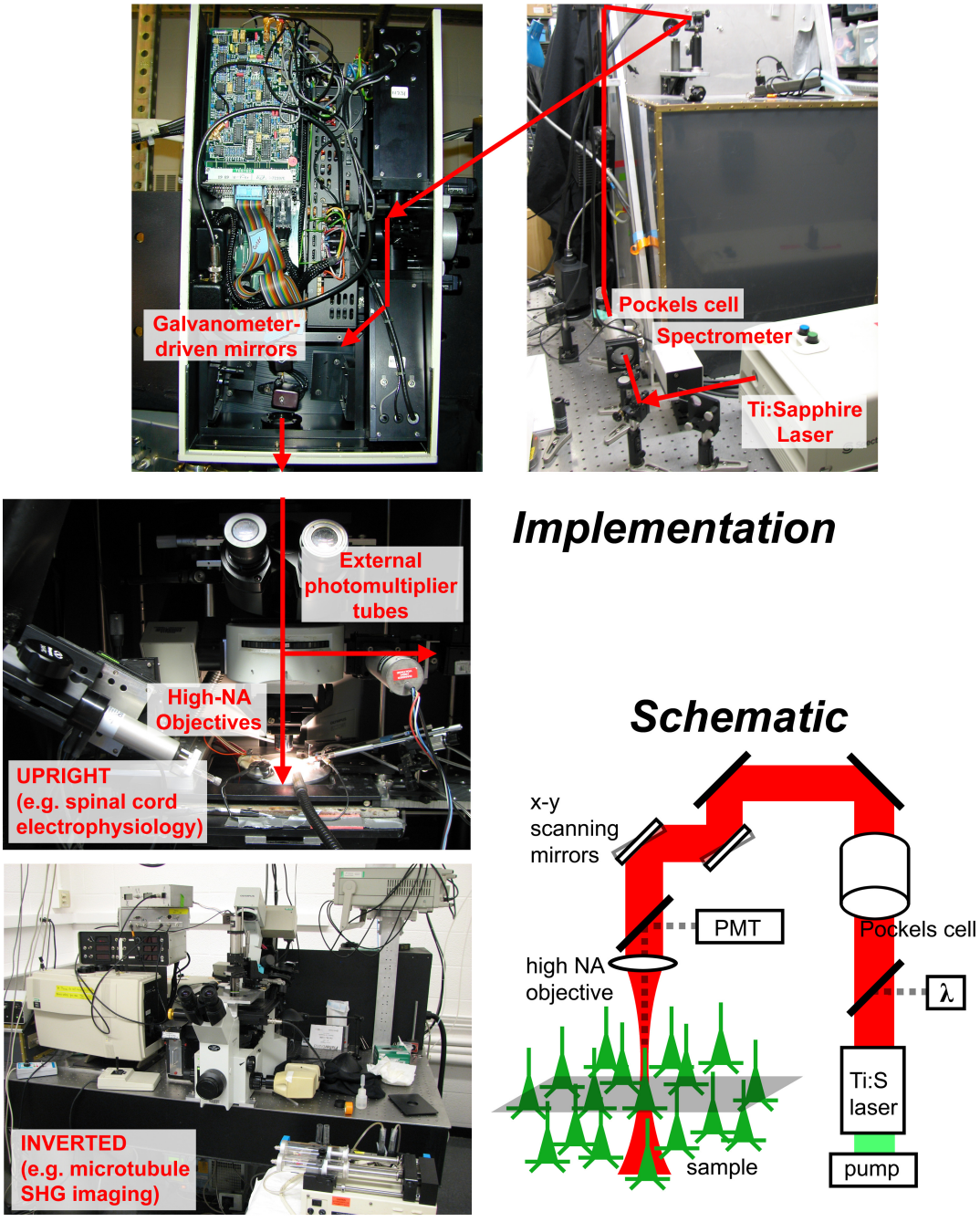

Figure 1.2: Schematics and photographs of two-photon-excited fluorescence and second harmonic generation microscopes.

of TPF and SHG microscopy, nonlinear optical techniques that are suited for imaging deep in scattering tissues with sub-micron spatial resolution. I will describe the enabling advantages of nonlinear optical microscopy by discussing several sample applications.

A major benefit of optical microscopy is its ability to probe cells in a non-invasive manner. TPF microscopy has the added advantage of extending the imaging depth up to $\approx$1 mm [Theer et al., 2003]. Deep-tissue imaging is possible because TPF arises only at the focal volume so all fluorescence photons, ballistic and scattered, contribute as useful signal [Denk & Svoboda, 1997]. In anesthetized small animals, the brain can be made optically accessible by thinning a small region of the skull (see Appendix C). Through this "brain window," neurons and smaller neuronal processes can be watched in their native, *in vivo* environment (Figs. 1.3 and 1.4). Survival surgery permits repeated imaging sessions on the same animal for a time-lapse view of structural plasticity. This approach has led to the observations of sensory experience affecting dendritic spine turnover [Trachtenberg et al., 2002, Grutzendler et al., 2002] and arrested growth of senile plaques in Alzheimer's disease mouse models [Christie et al., 2002].

Functional information can be reported by fluorophores whose optical properties, such as fluorescence quantum efficiency, lifetime, and excitation cross-section, are affected by the local chemical environment. These fluorophores can be inorganic dyes or fluorescent proteins, which is potentially powerful because they can be genetically-specified in transgenic animal models (Fig. 1.5). TPF from these functional fluorophores has been applied to study ion concentration dynamics in various structures, from dendritic spines (diameter of <1 μm) [Sabatini & Svoboda, 2000] to dendritic branches [Svoboda et al., 1996] and from single cell [Kloppenburg et al., 2000] to neuronal population that consists of hundreds of cells [Stosiek et al., 2003]. In particular, calcium-sensitive indicators have been popular because they are bright [Tsien, 1999] and calcium

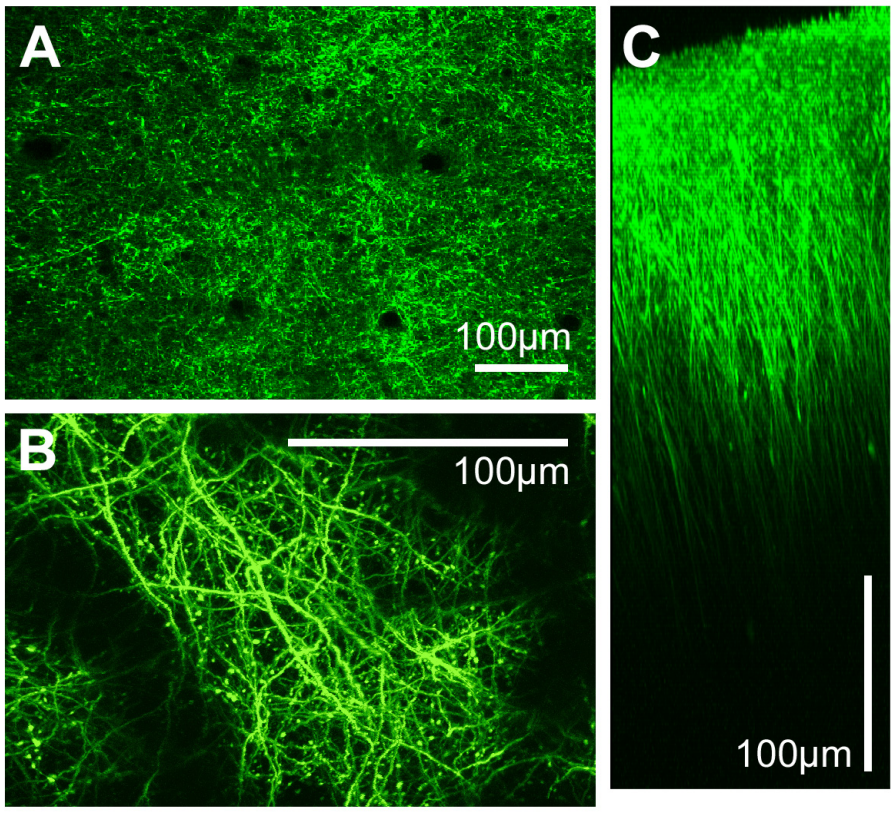

Figure 1.3: *In vivo* transcranial imaging of dendrites and dendritic spines in *Thy1*-YFP line-H mice. (A) Low-magnification view of superficial neocortex reveals a mesh work of neuronal processes. The black holes are presumably penetrating arterioles [Nishimura et al., 2007], large blood vessels that plunge perpendicularly to the cortical surface. (B) Individual dendrites and dendritic spines are clearly visible. (C) *Thy1*-YFP line-H mice selectively label neurons in layer 5, but not in other layers of the neocortex. The *x*-*z* view shows that two-photon-excited fluorescence comes from the apical dendrites, but not the cell bodies, of layer 5 pyramidal neurons that lie $\approx$ 1 mm beneath the neocortical surface.

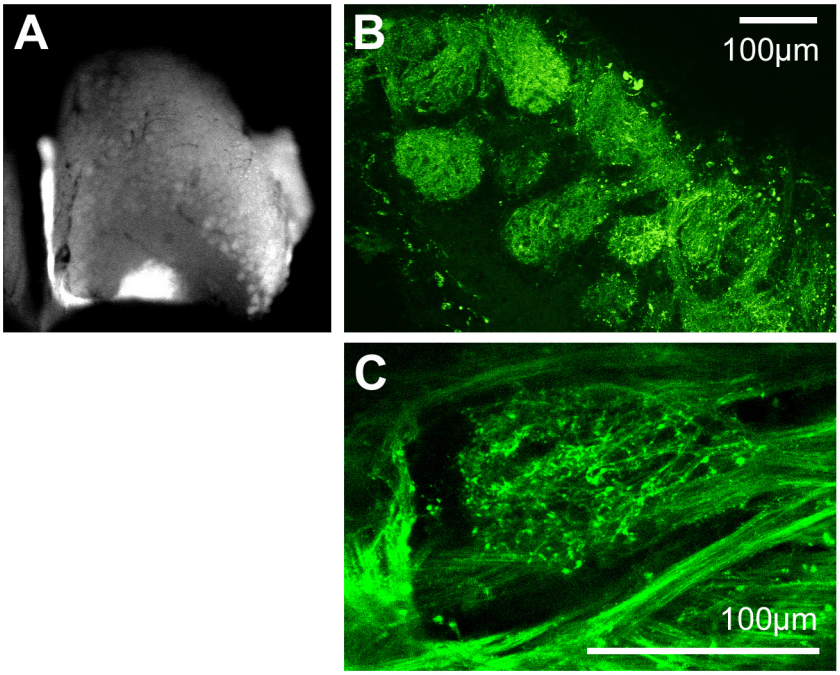

Figure 1.4: Olfactory bulb retrogradely labeled with dextran-conjugated fluorescent dyes shown at multiple length scales. (A) The right olfactory bulb was labeled by microinjection of dextran-conjugated fluorescein into the right nostril 4 days prior to formaldehyde fixation and imaging, using procedures described by [Wachowiak & Cohen, 2001]. Wide-field fluorescence image can barely resolve the labeled glomeruli. (B) Low-magnification two-photon image clearly distinguishes multiple glomeruli, $\approx$ 100 μm in diameter, that lie on the surface of the olfactory bulb. (C) *In vivo* transcranial imaging of an olfactory bulb retrogradely labeled with dextran-conjugated Oregon Green BAPTA-1. Axons from olfactory sensory neurons converged onto a single glomerulus.

influx can be used to infer spiking activity [Kerr et al., 2005], a property that is used in experiments described in Chapter 4.

Autofluorescence and intrinsic SHG emissions can provide additional information about the molecular states and orientations of endogenous proteins [Zipfel et al., 2003a]. For example, autofluorescence from NAD(P)H, an electron carrier used in metabolic pathways, reflects the metabolic state of the cell [Kasischke et al., 2004, Vishwasrao et al., 2005]. SHG from microtubules is emitted only when the tubular array is polarized [Campagnola et al., 2002, Dombeck et al., 2003]. Investigation of optical properties from endogenous biomolecules forms the basis of Chapters 2 and 3. The lack of fluorescence can also be used. For example, blood flow can be measured [Kleinfeld et al., 1998] by imaging the non-fluorescent red blood cells in capillaries that have been filled with dextran-conjugated fluorophores (Fig. 1.6). When combined with laser ablation to clot blood vessels, this approach can be a model for studying stroke and ischemia [Schaffer et al., 2006].

Finally, neuroscience research has been a driving force for innovations in TPF and SHG microscopy. Experimental demands such as direct measurement of action potentials [Dombeck et al., 2005, Sacconi et al., 2006] and delivering molecules at dendritic spines [Duemani Reddy et al., 2008, Harvey et al., 2008] have led to application-specific technical improvements. For example, because behavior is the most biologically relevant output of a neural circuit, there have been many attempts to miniaturize nonlinear microscopes for awake mouse experiments. Making a lightweight microscope presents many challenges, which have resulted in successively better implementations from fiber-coupling of excitation light [Helmchen et al., 2001] to better fibers [Ouzounov et al., 2002] and from gradient-index (GRIN) lens objectives [Levene et al., 2004, Jung & Schnitzer, 2003] to micro-electromechanical systems-

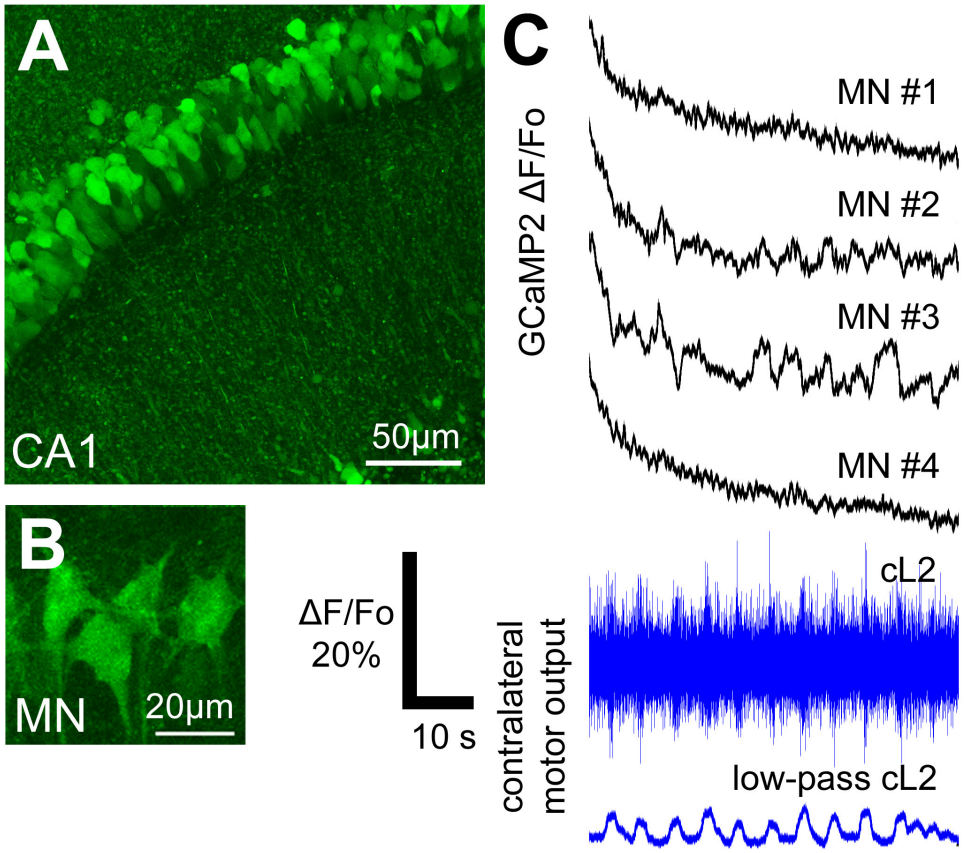

Figure 1.5: Two-photon imaging of a genetically-encoded calcium indicator proteins in the hippocampus and spinal cord. (A) The calcium-sensitive GCaMP2 fluorescent protein was expressed under the *Thy1* promoter. These mice were generated by Dr. Yvonne Tallini in Dr. Michael Kotlikoff's laboratory [Tallini et al., 2006]. In hippocampal brain slices, individual soma within the CA1 cell layer can be clearly distinguished. The neuronal processes contain fluorescence spots, which suggest possible binding of GCaMP2 to intracellular compartments that could reduce the indicator's sensitivity to calcium. (B) GCaMP2 fluorescence in motor neurons within an intact spinal cord. (C) Calcium transients could be recorded within some motor neurons (from B) during fictive locomotion elicited by bath application of serotonin, NMDA, and dopamine.

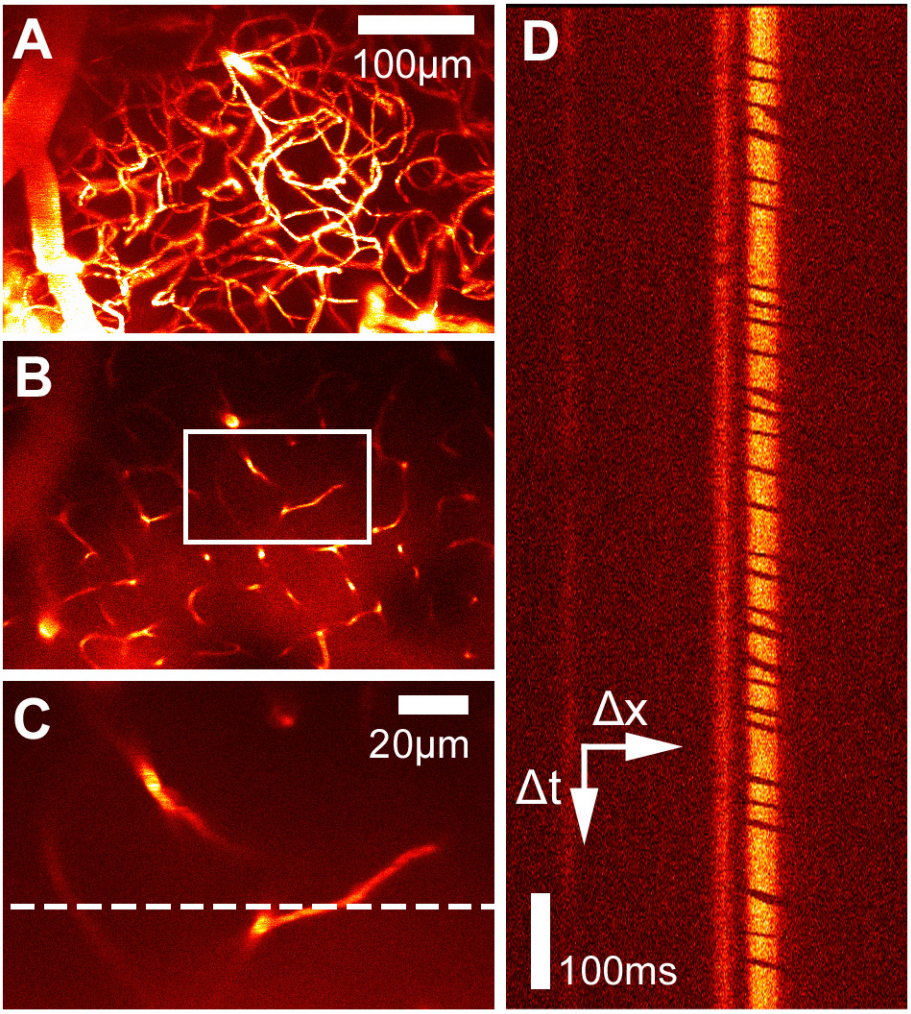

Figure 1.6: *In vivo* transcranial imaging of blood flow using dextran-conjugated fluorescent dyes. (A) A z-projection image of the microvasculatures within the neocortex. The blood was labeled by intraperitoneal injection of fluorescein isothiocyanate (FITC)-dextran. (B) Image at one focal plane within the image stack from A. (C) High-magnification view of a small region that includes several capillaries, 5-10 μm in diameter. (D) Linescan at the location indicated by the dotted line in C. The streaks are due to traversing red blood cells, whose intact plasma membrane excludes the dextran-conjugated dye. By dividing the horizontal distance by the vertical time axes, the velocity of red blood cells within the capillary can be measured.

based scanning mirrors [Piyawattanametha et al., 2006]. Almost all of these improvements were initially demonstrated by applying to brain imaging, although they are now also finding applications in more areas such as medical endoscopy.

CHAPTER 2

POLARIZED MICROTUBULE ARRAYS IN APICAL DENDRITES AND AXONS*

The polarization of microtubules within neurons *in vivo* is crucial in their role of determining the directions and speeds of intracellular transport. More than a decade ago, electron microscopy studies of mature hippocampal cultures indicated that their axons contained microtubules of uniform polarity and that dendrites contained microtubules of mixed polarity. Here, we evaluated polarity distributions in native brain tissues and in cultures by using multiphoton microscopy and second-harmonic generation from microtubules. We confirmed the expected polarized microtubule arrays in axons; however, we also unexpectedly found them ubiquitously in apical dendrites of mature hippocampal CA1 and cortical layer V pyramidal neurons. Some of these organized dendritic microtubule arrays extended for >270 μm with overall polarity of >80%. Our research indicates neurite-specific and age-dependent microtubule organizations that have direct implications for neuronal cargo transport.

2.1 Introduction

Active intracellular transport along microtubules is essential for establishing and maintaining the functions of axons and dendrites. Anterograde transport through neurites delivers cargoes that are produced in the soma, including postsynaptic densities, neurotransmitter receptors, ion channels, and specific mRNAs to dendritic locations, as well as components of presynaptic terminals, adhesion molecules, and mitochondria to axonal locations [Hirokawa & Takemura, 2005, Hirokawa, 1998]. These cargoes are trans-

*Originally published as: Kwan, A. C., Dombeck, D. A., Webb, W. W. (2008). Polarized microtubule arrays in apical dendrites and axons, Proc Natl Acad Sci USA 105, 11370-11375

ported by molecular motors, such as kinesin and dynein, which tread unidirectionally on microtubules. To understand this directional trafficking [Vale, 1996, Davis et al., 1990, Guillaud et al., 2003, Stepanova et al., 2003], it is essential to know both the motor proteins and the microtubule polarities involved. Recently, great progress has been made in elucidating the numerous motor proteins, including the molecular and functional classification of their superfamilies [Hirokawa & Takemura, 2005, Vale, 2003, Kanai et al., 2004], but few studies have characterized the microtubule organization in neurons, particularly in dendritic processes.

Past studies of microtubule polarity used electron microscopy to visualize neurites that were lysed in a tubulin-containing buffer, which would decorate clockwise or counterclockwise "hooks" on microtubules depending on their polarity [Heidemann & McIntosh, 1980]. The hook method, applied on hippocampal cultures [Baas et al., 1989, Baas et al., 1988, Takahashi et al., 2007], indicated that microtubule arrays have uniform polarity (≈100% plus-ends distal from soma) in neurites of nascent neurons, uniform polarity in mature axons, and mixed polarity (≈50% plus-ends and ≈50% minus-ends distal from soma) in mature proximal dendrites. This difference between axons and dendrites of cultured hippocampal neurons had been implicated as a milestone in the establishment of neuronal polarity [Baas, 1999]. However, the requirement of thin, fixed sections for electron microscopy [Baas et al., 1989, Baas et al., 1988] has limited successful application of the hook method to only a few tissue preparations [Burton, 1988, Rakic et al., 1996]. Recently, fluorescently labeled plus-end tracking proteins have been used to estimate microtubule polarity in fruit flies [Rolls et al., 2007] but not yet in mammals.

Second-harmonic generation (SHG) microscopy can image noncentrosymmetric protein structures with high hyperpolarizability, such as collagen and microtubules

[Dombeck et al., 2003, Campagnola & Loew, 2003, Campagnola et al., 2002], but few other known protein structures. SHG, as a nonlinear optical process, occurs in microtubules because tubulin is hyperpolarizable and asymmetric along its longitudinal axis; therefore, adjacent microtubules of the same polarity constitute an array of aligned scattering dipoles that, through constructive interference [Moreaux et al., 2000], emit a coherent optical signal at exactly half the excitation wavelength. Conversely, emitted fields from adjacent microtubules of opposite polarities would destructively interfere and eliminate or degrade the SHG signal. Thus, the SHG signal comes from microtubule arrays that have parallel polarization. However, SHG intensity alone does not distinguish the sign of net orientation between plus- or minus-end-oriented arrays. SHG has been used as an imaging tool in living preparations [Dombeck et al., 2004, Dombeck et al., 2005, Williams et al., 2005, Zipfel et al., 2003b, Brown et al., 2003, Sacconi et al., 2006, Débarre et al., 2006] to identify polarized microtubule arrays in mitotic spindles of RBL cells [Dombeck et al., 2003] and *Caenorhabditis elegans* embryos [Campagnola & Loew, 2003, Campagnola et al., 2002] and in cilia [Dombeck et al., 2003]. Polarized microtubule arrays were also found in hippocampal slices in our earlier research [Dombeck et al., 2003], where we looked at tissues from young rat pups. Here, we extend the research to brain slices of mice of older age groups and show that the microtubule polarity in dendrites is age-dependent, with significant differences between neurons in cultures and in mature brain tissues.

2.2 Materials and Methods

Acute Brain Slices. All preparations were performed in accordance with Cornell University animal use regulations (Institutional Animal Care and Use Committee protocol 00-46-03). Wild-type C57BL/6 (Charles River) or transgenic mice that express YFP

under the *Thy1* promoter (strain B6.Cg-Tg(*Thy1*-YFPH)2Jrs/J); Jackson Laboratories) were purchased and housed in the Laboratory Animal Services. The brain was removed after CO_2 euthanasia of mice older than postnatal day 10 (P10) and decapitation of pups. Transverse hippocampal or coronal cortical slices 400 μm thick were cut in a Vibratome (Campden Instruments) at $\approx$4 °C in artificial cerebrospinal fluid (ACSF) composed of 120 mM NaCl, 2.5 mM KCl, 1 mM NaH_2PO_4, 1.3 mM $MgSO_4$, 25 mM $NaHCO_3$, 10 mM d-glucose, and 2.5 mM $CaCl_2$ and was saturated with 95% O_2 and 5% CO_2. Dissection and cutting were performed quickly to minimize damage. Slices were then incubated in ACSF at 35 °C for 1 hr before imaging. During imaging, slices were held under nylon grid anchors in a flow chamber (Warner Instruments) continuously perfused with oxygenated ACSF at room temperature.

Primary Cultures. Hippocampal cultures were prepared as described in [Dombeck et al., 2003]. For immunohistochemistry, cultured neurons were fixed in 3.7% paraformaldehyde in PBS containing 15% sucrose at 4 °C. Neurons were stained overnight with primary antibodies for Tau-1 (mouse, dilution 1:400; Chemicon) and MAP-2 (rabbit, 1:500; Chemicon) and then with secondary antibodies (Alexa Fluor 488 anti-mouse and Alexa Fluor 568 anti-rabbit, both from Invitrogen, 1:40). The samples were mounted in Vectashield antifade solution (Vector Laboratories) and imaged with a Bio-Rad MRC1024 confocal microscope equipped with an argon/krypton laser for excitation at 488 and 568 nm.

Imaging. For multiphoton and SHG imaging, we used a Bio-Rad MRC1024 scan head mounted on an inverted Olympus IX-70 microscope. Excitation was provided by a mode-locked Tisapphire laser (Spectra-Physics Tsunami). Beam intensity was controlled with a Pockels cell with flyback synchronization, and polarization was modified with a Berek compensator (New Focus). The excitation was focused with an Olym-

pus UApo/340 20X/NA 0.7 water-immersion objective, and the forward emission was collected with an Olympus XLUMPlanFl 20X/NA 0.95 dipping objective. The average excitation laser intensity was 10 to 100 mW. SHG and fluorescence were collected in the forward and backward directions by bialkali photomultiplier tubes (Hamamatsu HC125-02) after infrared blocking filters (Semrock or Chroma Technology) and narrow bandpass filters with bandwidth of 10 nm (Semrock). Unless specified, images were obtained with SHG collected in the forward direction. SHG was verified by tuning the excitation wavelengths and observing the emission shift using narrowband filters. Because SHG intensity was weak, signal-to-noise was improved by averaging three to five scans that exposed the tissue for ≈6 to 10 s or by lowering the illumination intensity and then collecting in photon counting mode for 30 to 60 s. Quantitative image analysis was done with MATLAB and Alice (Perceptive Informatics).

SHG Intensity Ratio Measurements. Several drops of PBS mixed with 6-μm-diameter fluorescent beads (Fluoresbrite YG; Polyscience) were added to the culture dish by transfer pipette. Microtubules were imaged at a depth ≈10 μm below the beads. We measured the forward- and backward-directed SHG by photon counting at each pixel. To correct for background, we subtracted autofluorescence measured from adjacent empty regions. System detection efficiency was calibrated by measuring fluorescence of the beads. For acute slices, fluorescent beads were added to a transverse hippocampal or coronal slice 250 μm thick before the slice was placed between two glass coverslips so that, as in making wet-mount microscope slides, surface tension-induced adhesive forces would naturally draw the cover glasses together to yield a final inter-glass thickness of 30 to 50 μm. Thin slices were critical for reducing backscattered SHG [Zipfel et al., 2003a, Débarre et al., 2006]. Flattening might cause tissue damage, but a favorable comparison between normal tissues (Fig. 2.1A) and flattened tissues (Fig. 2.7A) showed that the effect on microtubules is tolerable within the <10 min of time of

individual imaging experiments. After flattening tissues, the SHG signal tends to endure for ≈30 min, whereas in normal tissue, SHG can be seen in acute slices for >4 hr.

Numerical Simulation. Numerical simulation of SHG in the regime of focused laser beam that has been described [Moreaux et al., 2000, Williams et al., 2005] is applied to microtubules in this research (see Section 2.5 for details).

2.3 Results

Polarized Microtubule Arrays Are Localized to Apical Dendrites and to Axons in Adult Mice. To investigate regional differences of microtubule polarity, we imaged acute brain slices with SHG microscopy. In the hippocampus of a 5-month-old mouse, we found the expected SHG in the axonal mossy fiber, which we had seen in younger animals [Dombeck et al., 2003], but surprisingly the CA1 stratum radiatum also generated SHG (Fig. 2.1A), which was not seen before. This finding was unexpected because stratum radiatum is known to be predominantly dendritic [Johnston & Amaral, 2004].

To identify more accurately the types of neurites that contain polarized microtubule arrays, we used multiphoton microscopy [Denk et al., 1990, Zipfel et al., 2003b] and SHG microscopy to image acute slices of 4- to 12-month-old transgenic mice that express YFP controlled by *Thy1*-promoter (*Thy1*-YFP line-H) [Feng et al., 2000]. This strain labels neurons exclusively, enabling us to compare SHG with neuronal morphology. The SHG was seen to localize to proximal apical dendrites of CA1 pyramidal neurons (Fig. 2.2B and C). In adult mice (n = 5; >4 months old), we found that 41 of 45 (91%) YFP-labeled pyramidal neurons emitted SHG. Because not all neurons expressed YFP, we also observed SHG from apical dendrites of unlabeled pyramidal neurons. The number of all SHG-emitting dendrites is comparable with the expected number of CA1

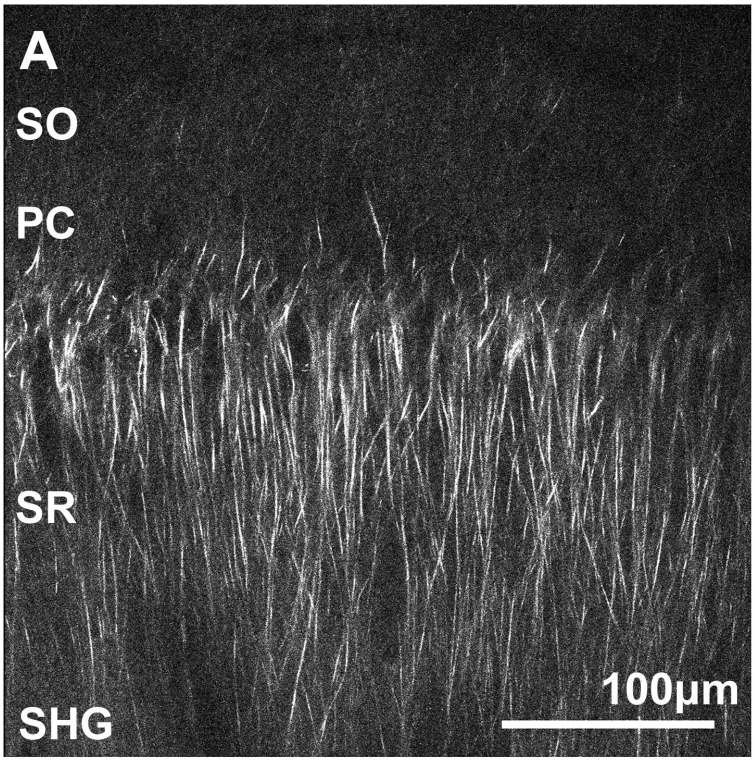

Figure 2.1: Polarized microtubule arrays in acute brain slices of adult wild-type and *Thy1*-YFP mice (Part 1). (A) SHG in area CA1 of an acute hippocampal slice of a 5-month-old wild-type mouse. Subregions stratum oriens (SO), pyramidal cells (PC), and stratum radiatum (SR) can be identified by autofluorescence (data not shown). The image is a z-projection of optical z-sections taken 10 μm apart with laser excitation at 774 nm that has linear polarization oriented along the apical dendrites.

neurons in adult mice [Calhoun et al., 1998]. These data suggest that virtually all apical dendrites contain polarized microtubule arrays. We also observed SHG in the region stratum oriens. Because these signals were sparse, we reasoned that they did not originate from basal dendrites, which are ubiquitous in the region, but instead came from CA1 axons that could project laminarly for a short distance before descending to the subiculum [Johnston & Amaral, 2004]. Because there are no immature neurons in area

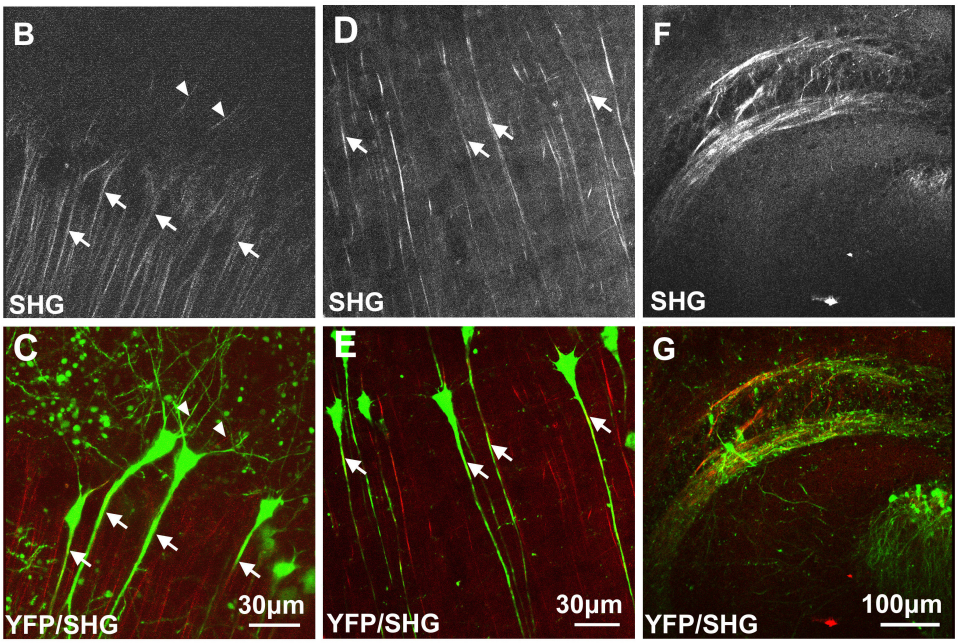

Figure 2.2: Polarized microtubule arrays in acute brain slices of adult wild-type and *Thy1*-YFP mice (Part 2). (B) SHG in area CA1 of a 5-month-old *Thy1*-YFP mouse. (C) Composite image of multiphoton-excited YFP fluorescence (green) and SHG (red) at the same location as B. Polarized microtubule arrays colocalize with apical dendrites of CA1 pyramidal neurons (arrows). SHG also appears in stratum oriens and is likely caused by axons (solid triangles). (D and E) SHG and composite image in neocortex of an acute coronal cortical slice of an 11-month-old *Thy1*-YFP mouse. Polarized microtubule arrays colocalize with apical dendrites of layer V pyramidal neurons (arrows). (F and G) SHG and composite image in area CA3 of a 5-month-old Thy1-YFP mouse. Polarized microtubule arrays colocalize with the dense axonal bundle that forms the mossy fiber. All images are projections of three to six optical z-sections taken 10 μm apart with laser excitation at 774 nm that has linear polarization oriented along the apical dendrites.

CA1 of the adult hippocampus [Lledo et al., 2006], we conclude that the SHG there comes from apical dendrites of mature CA1 pyramidal neurons. In the neocortex (Fig. 2.2D and E), we found colocalization of YFP fluorescence and SHG in 36 of 41 (88%) layer V pyramidal neurons in adult mice (n = 2). Polarized microtubule arrays in apical dendrites extended to 270 μm, with an average distance of 201±37 μm, toward upper cortical layers. In contrast, basal and oblique dendrites did not generate detectable SHG. In area CA3 (Fig. 2.2F and G), SHG was emitted from the mossy fiber, an unmyelinated axonal bundle. Our data in the hippocampus and in the neocortex of adult mice suggest that polarized microtubule arrays exist not only in axons, but also in large stretches of apical dendrites of pyramidal neurons.

Distribution of Polarized Microtubule Arrays Depends on Age. To determine whether the distribution of polarized microtubule arrays in native brain tissue depends on development, we imaged hippocampi of mice 1 week to >18 months old (Fig. 2.3; n = 27 mice) and found consistent trends among mice of same age groups. For axons, the mossy fiber contained polarized microtubule arrays in young mice and maintained polarity into late adulthood. Additional SHG signals were often seen in neurites lining the CA3 and dentate gyrus cell layers that funnel into the mossy fiber in mice <1 month old. For CA1 apical dendrites, polarized microtubule arrays existed but were relatively sparse and short in young mice (Fig. 2.3B). At 1 month old, arrays became discernible and increased in both density and length, initially in the CA1 pyramidal cell layer and subsequently in the stratum radiatum (Fig. 2.3E). These polarized microtubule arrays grew to ≈90 μm long until the mice were 4 months old and then did not change significantly (Fig. 2.3H). The observed changes could be caused by either a polarity change in the existing microtubule array or the addition of new polarized microtubules. Polarized microtubule arrays in area CA1 were seen in ages up to the oldest mice investigated (18 months old). The developmental change in the structure of these microtubule arrays is

quantified by data plots in (Fig. 2.4). Our data show that polarized microtubule distribution in neuronal processes is dynamic within a period of rapid learning and development in the lifetime of the mouse.

Numerical Simulation of SHG from a Microtubule Array. To estimate quantitatively the microtubule polarity, numerical simulations calculated the amount of SHG generated from a microtubule array. The physics of SHG is well understood, and studies [Moreaux et al., 2000, Williams et al., 2005] have derived the theory for excitation by a focused laser beam (see Section 2.5).

The absolute SHG intensity depends on the laser power and the hyperpolarizability, number density, spacing, and polarity of the microtubules. Microtubule number density and spacing can be estimated because we have two pieces of a priori knowledge about the spatial arrangement of the dipoles: (i) The dipoles, presumably tubulins, line up in helical arrays to form a microtubule; (ii) The mean distance between microtubules in neurites is set by microtubule-associated proteins (MAPs), as has been measured by electron microscopy [Chen et al., 1992]. Furthermore, we assumed the extent of the tubule array to be approximately the size of a typical neurite [Fiala & Harris, 1999]. With these parameters, we calculated forward- and backward-directed intensities of SHG caused by single neurites (Fig. 2.5A) for increasing microtubule polarity. It is illuminating to compare the simulated forward-directed SHG intensities (Fig. 2.5B, circles) with simple quadratic equations (Fig. 2.5B, solid lines) that consider interference and SHG as a second-order process. The fits are best near uniform polarity and deviate slightly at mixed polarity because the microtubules are spatially distributed and therefore their SHG fields do not exactly cancel destructively. This quadratic dependence makes signal intensity a good qualitative indicator of microtubule polarity because a small decline in polarity would cause a large drop in intensity.

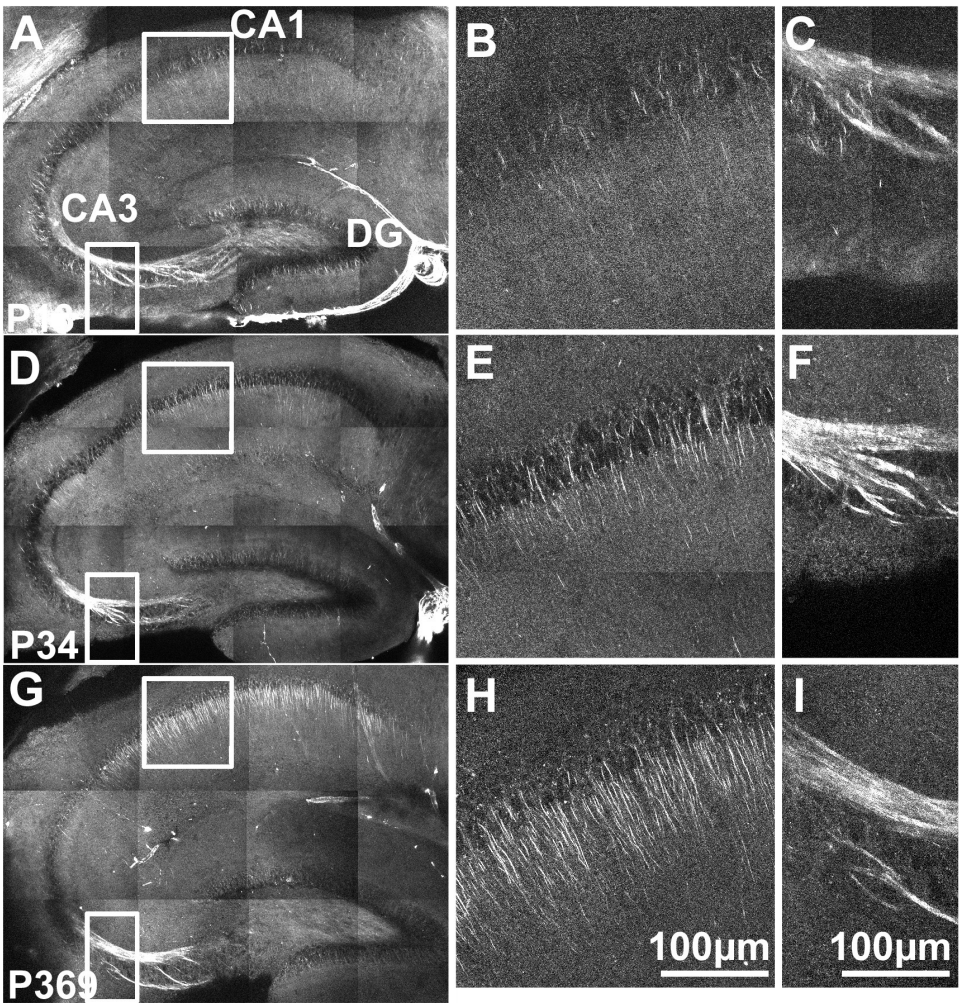

Figure 2.3: Polarized microtubule arrays in acute hippocampal slices of young, juvenile, and adult mice. (A) SHG in hippocampus of a postnatal day 13 (P13) mouse. The patchy background is caused by weak autofluorescence that is picked up by the SHG detector. (B and C) Magnified SHG views of the area CA1 and the mossy fiber from the boxed areas in A. (DF) Same as A to C of a P34 mouse. (GI) Same as A to C of a P369 mouse. Images are mosaics of 12 projections of optical z-sections at 15 μm apart with laser excitation at 774 nm that has linear polarization oriented along the apical dendrites.

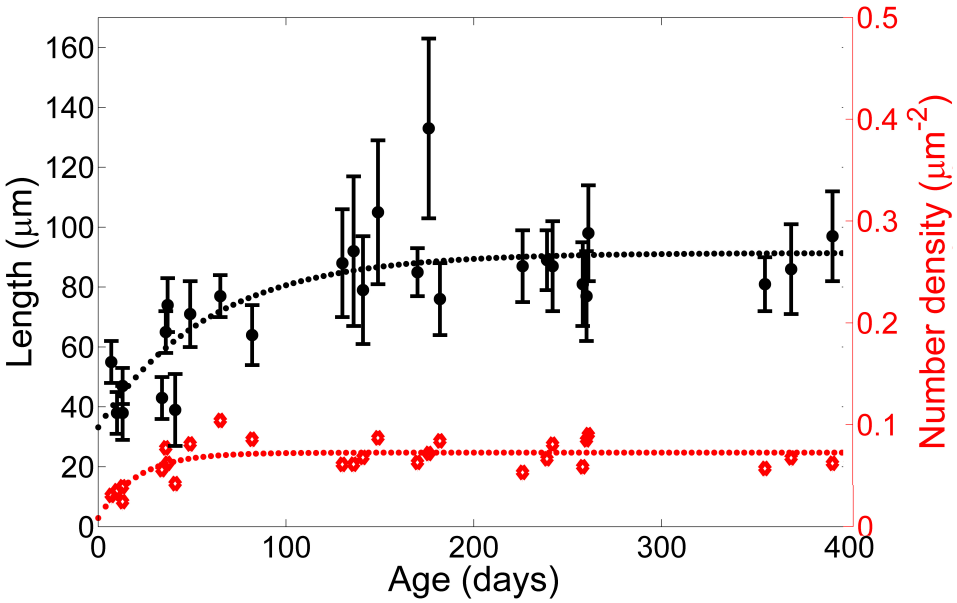

Figure 2.4: Age dependence of length and number density of polarized microtubule arrays in area CA1. The length of polarized microtubule arrays is the extent to which SHG-emitting neurites extend from the pyramidal cell layer in area CA1. Each point is an average of 10 neurites, and the error bars are ±SD. An exponential fit illustrates the trend. The number density counts the number of SHG-emitting neurites within an image and divides that number by the length of the CA1 cell layer and the depth of an optical section, which is ≈2 μm. In adult mice, our measured density of 0.07 μm^{-2} would yield $\approx 2 \times 10^5$ CA1 pyramidal neurons in one hippocampus that is 1.5 mm thick with a 2-mm-long CA1 cell layer.

Further examination of the theory (see Section 2.5) shows that laser power and hyperpolarizability scale linearly with forward- and backward-directed SHG intensities; thus, they do not affect the ratio of forward- over backward-directed SHG intensity (f/b SHG ratio). Therefore, given assumptions about the microtubule number density and spacing, the f/b SHG ratio can be directly related to microtubule polarity (Fig. 2.5C). In practice, the f/b SHG ratio is also easier to measure than absolute SHG intensity because it is difficult to determine sample hyperpolarizability.

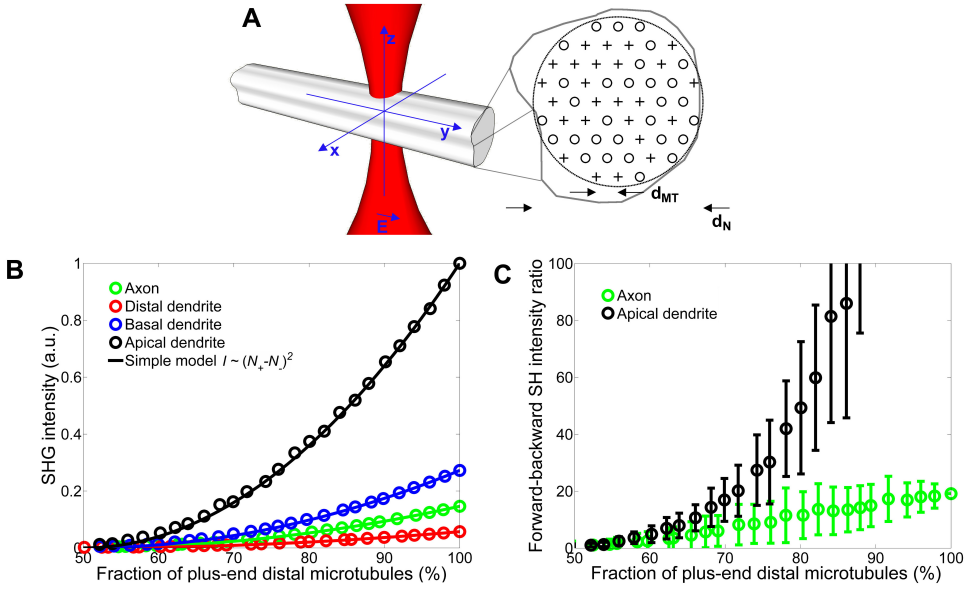

Figure 2.5: Numerical simulation of SHG generated by a microtubule array.(A) Schematic drawing of the simulation model. A focused laser beam impinges on a neurite with diameter d_N that contains a hexagonal packed array of plus- or minus-end distal microtubules with inter-microtubule spacing d_{MT}. SHG intensities were calculated in the forward and backward directions for four classes of neurites: apical dendrites (d_{MT} = 64 nm, d_N = 3 μm), basal dendrites (d_{MT} = 64 nm, d_N = 1 μm), distal dendrites (d_{MT} = 64 nm, d_N = 0.5 μm), and axons (d_{MT} = 22 nm, d_N = 0.17 μm). (B) Simulated forward-directed SHG intensities generated by each type of neurite (circles). Polarity is defined as the number of plus-end distal microtubules divided by the total number of microtubules in the simulated neurite. The simulated intensities were compared with a simple model (solid line) where SHG intensity $\approx[N_+ - N_-]^2$, where N_+ and N_- are the numbers of plus- and minus-end distal microtubules. Backward-directed signals are too small to be shown in the same vertical scale. (C) Simulated fb SHG intensity ratio. The error bars are ±SD. Uncertainty is caused by the possible variety of microtubule distributions that can be arranged within a neurite.

Measuring the Polarity of Microtubule Arrays Within Neurites. To verify the validity of our approach of using the f/b SHG ratio to estimate microtubule polarity, we made measurements in hippocampal cultures, where published values of polarity exist based on the hook method. Immature and mature neurons were identified separately by staining for Tau-1 and MAP-2. After 23 days in culture, developing neurons possessed multiple minor processes and sometimes had nascent axons, which all contained polarized microtubule arrays (Fig. 2.6 A to C). In cultures >7 days old, we distinguished axons and dendrites of mature neurons by using MAP-2 as a specific marker for dendrites [Ferreira et al., 1987]. Polarized microtubule arrays were found in axons (Fig. 2.6 E to H) but were absent in the dendrites that could be clearly distinguished. Measurements from Tau-1-stained axons produced an f/b SHG ratio of 20±2, which translates to a microtubule polarity of ≈100% (+0%, -22%) (see Section 2.5 for error analysis). In comparison, past studies with the hook method found polarities of 57±4% for dendrites and 99±4% for axons in mature neurons. Our observations of developmental changes agree with past observations [Baas et al., 1988, Baas et al., 1989] that, in cultures, protoprocesses of immature neurons and axons of mature neurons have uniform polarity microtubules, whereas dendrites have mixed polarity microtubules.

Using the same methods, we quantified microtubule polarity in acute brain slices that were flattened to 30 to 50 μm thick to minimize backscattered signal. From axons in the hippocampal mossy fiber of adult mice, we measured an f/b SHG ratio of 27±5, which corresponds to mean microtubule polarity of ≈100% (+0%, -17%). The f/b SHG ratio of axons in acute slices was higher than expected from the simulation, a difference that could be caused by a higher packing density of microtubules in axons in acute slices. From apical dendrites, in the area CA1 of adult mice (Fig. 2.7) we found mean polarity of 81% (+7%, -9%), and in the layer V cortex, mean polarity of 80% (+6%, -6%), which correspond to f/b SHG ratios of 53±27 and 50±12, respectively.

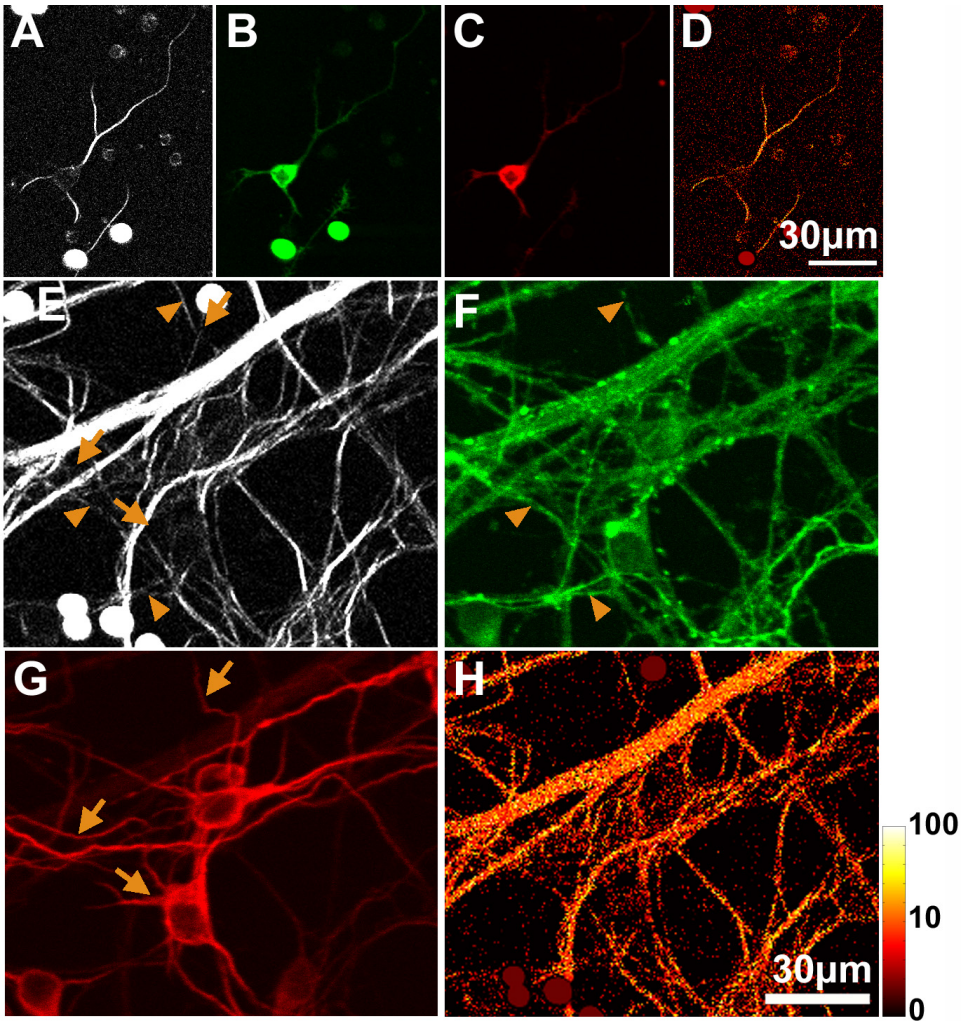

Figure 2.6: Measuring microtubule polarity in dissociated hippocampal cultures. (A) SHG from neurons 3 days in culture. Protoprocesses in neurons at this stage contain polarized microtubule arrays. The solid circles with saturated fluorescence signal are beads added to calibrate the SHG detectors. (B and C) The same neuron fixed and stained for Tau-1 (green) and MAP-2 (red), which were localized to the soma in immature neurons. (D) Pixel-by-pixel forwardbackward intensity ratios calculated from A. (E to H) Same as A to D but from neurons 9 days in culture. SHG and Tau-1 were present in the axons (solid triangles), but SHG was absent in the dendrites, which contains MAP-2 (arrows). The SHG images were taken with circularly polarized excitation at 854 nm.

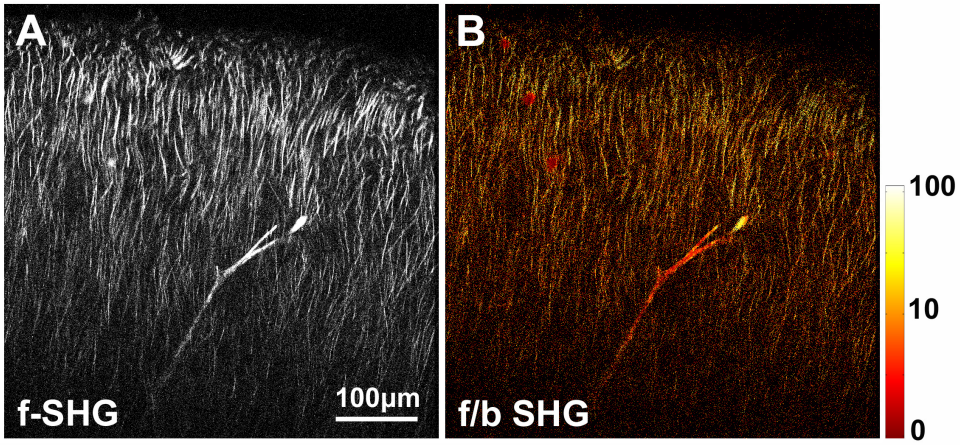

Figure 2.7: Measuring microtubule polarity in acute brain slices. (A) Measured forward-directed SHG (f-SHG) images in area CA1 of an 8-month-old wild-type mouse. A Y-shaped blood vessel is visible. (B) Pixel-by-pixel f/b SHG ratios calculated from A. Image was taken with laser excitation at 854 nm that has linear polarization oriented along the apical dendrites.

Importantly, the f/b SHG ratio is not strictly a result of strong SHG; it depends on the spatial distribution of the scatterers. This is shown by SHG from the collagen matrix surrounding blood vessels (Fig. 2.7), which exhibit a modest f/b SHG ratio of ≈4 [Williams et al., 2005]. Although basal dendrites did not produce detectable SHG, we found by comparing the intensities recorded from the neuropil in the apical and basal sides of the CA1 cell layer that our detection sensitivity places an upper limit of ≈65% on the microtubule polarity in basal dendrites, indicating that the basal dendrites could contain microtubules with <65% overall polarity.

2.4 Discussion

Comparison of Methods for Measuring Microtubule Polarity. There is strong evidence that the optical signal in SHG imaging of brain tissues reported here originates from polarized microtubules. SHG is rare in biology, occurring only in asymmetric, optically nonlinear structures, hyperpolarizable with large-scale order; therefore, only a few biological systems (e.g., collagen, membrane labeled with noncentrosymmetric dyes) are known to emit SHG. The microtubule origin of SHG is effectively shown in intact brain slices by noticeable loss of signal after application of the microtubule-depolymerizing drug nocodazole ([Dombeck et al., 2003]; see also Fig. 2.8). Moreover, SHG from MAPs seems unlikely because SHG is seen in many microtubule-containing structures, e.g. axons, cilia, and mitotic spindles, with differing MAP compositions [Dombeck et al., 2003, Campagnola et al., 2002]. Finally, the requirement of same polarity is supported by the inherent physical requirement for constructive interference, the lack of SHG signal in the overlapping zones in mitotic spindle [Dombeck et al., 2003, Campagnola et al., 2002], and the axondendrite difference in hippocampal cultures.

Currently, there are two other techniques for establishing microtubule polarity, the hook method and fluorescently labeled plus-end tracking proteins. The hook method uses electron microscopy, which provides sufficient resolution for counting individual microtubules. It requires fixation and is quantitatively uncertain because of a large "unhooked" fraction from unstained microtubules. Using fluorescently labeled plus-end tracking proteins requires transgenic specimens or cells accessible to transfection because fluorescent proteins must be introduced. Quantification is indirect because it assumes that the trafficking patterns of plus-end tracking proteins reflect the polarity of

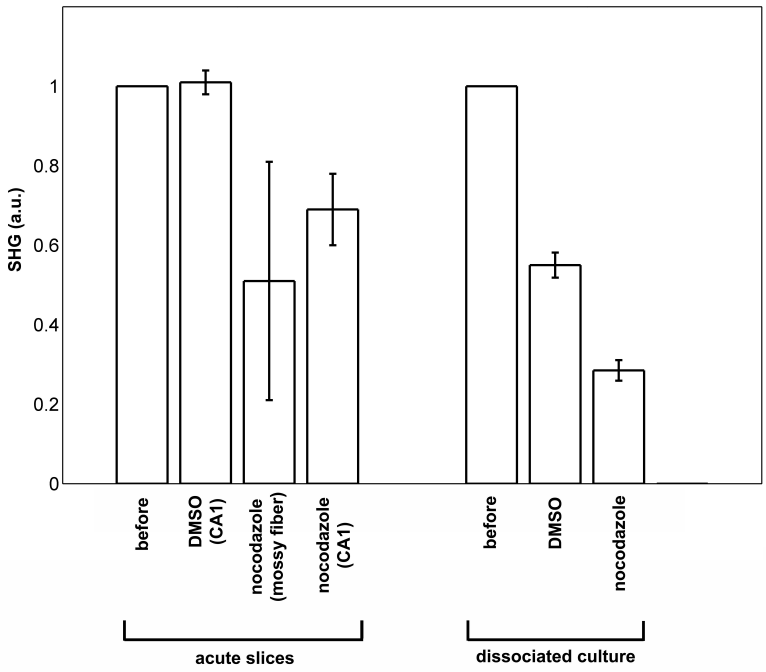

Figure 2.8: Effect of nocodazole on SHG from acute slices and dissociated culture. Large losses in SHG imply the observed signal originates from microtubules. The signal losses were partial in acute slices (n=2 for each case) possibly due to insufficient penetration of nocodazole, but also could be due to stabilized microtubules in neurites, as described in [Baas et al., 1993]. In cultures (n=4), SHG loss was more pronounced but DMSO also had an adverse effect. The experiment was performed in room temperature as described in Section 2.5.

the whole microtubule array, thus risking biased preference for actively polymerizing microtubules.

Because SHG microscopy requires no external perturbation, it can determine microtubule polarity in native tissues where fixation or transfection is prohibitive. However, the method has two limitations: quantification and determination of the sign of polarity. As shown here, polarity can be quantified by f/b SHG ratio measurements. Our culture experiments confirmed the simulation results with positive (uniform polarity in

axons) and negative (mixed polarity in dendrites) tests. Further tests at intermediate polarity values would require artificial assemblies of microtubule bundles with specific spacing and polarity. The SHG quantification of polarity requires knowledge of the spatial arrangement of microtubules, which must be estimated with electron microscopy [Chen et al., 1992] or superresolution immunohistochemistry [Bates et al., 2007]. Measuring the weak backward-directed SHG and estimating structural quantities can be subject to rather large uncertainties. Such structural parameters as dendrite thickness and microtubule packing density can influence SHG intensity, although the main determinant is polarity. For example, SHG intensity would drop by $\approx$70% if the polarity changed from 100% to 75% in a 3-μm-diameter neurite, but the same intensity drop would require a 9-fold shrinkage in cross-sectional area (Fig. 2.5B, solid lines). Determining the absolute sign of the microtubule polarity requires determination of the phase of emitted SHG relative to a reference sample or complementary information from transport studies.

Implications for Dendritic Transport. Our research reveals that polarized microtubule arrays are found both in axons and in a substantial subset of mature dendrites in native brain tissue (Table 1). Although axons generally contain polarized microtubule arrays throughout development, the microtubule distribution in apical dendrites is age-dependent, showing mixed polarity at early ages and increasing overall polarity up to 4 months of age. These results contrast with the usual interpretation of the known information on microtubule polarity inferred from cultured neurons where only axons and the distal dendritic tips contained polarized microtubule arrays in mature neurons. Furthermore, our result is consistent with previous research [Dombeck et al., 2003] using young rat pups where SHG was observed in axons. Therefore, our research indicates a critical revision of the canonical model of microtubule organization in specific fractions of dendrites *in vivo*.

Table 2.1: Microtubule polarity distribution within identified neurite groups

Neurite type	Region in the brain	Measured f/b SHG ratio	Microtubule polarity (uncertainties)
Axons	Mossy fiber from dentate gyrus to CA3	27±5	100% (+0%, -17%)
Axons	Hippocampal culture	20±2	100% (+0%, -22%)
Apical dendrites	CA1	53±27	81% (+7%, -9%)
Apical dendrites	Layer V neocortex	50±12	80% (+6%, -6%)
Basal dendrites	CA1	N/A	<65%

The concept that apical dendrites contain polarized microtubule arrays suggests that either plus-end- or minus-end-directed motor proteins, but not both types, are responsible for anterograde movement during transport, because plus-end- and minus-end-directed motor proteins would move in opposite directions. SHG imaging alone does not provide the sign of the polarity of the microtubule arrays; studies have shown that kinesin is responsible for anterograde cargo movement in dendrites [Hirokawa & Takemura, 2005], which indicates that microtubules in proximal apical dendrites are uniformly plus-end distal from the soma.

On average, proximal apical dendrites of CA1 and cortical layer V pyramidal neurons extend for ≈100 μm and ≈200 μm, respectively, before bifurcating, the same lengths found to contain polarized microtubule arrays. The benefit of such a uniaxial array is speed: primarily unidirectional transport of anterograde cargoes is thought to be

more efficient. A biophysical model of active transport [Smith & Simmons, 2001] has predicted that the anterograde flux in unidirectional transport is ≈10 times faster than in bidirectional transport for a 100-μm-long neurite because in unidirectional transport, cargoes spend more time actively moving toward the destination. *In vivo*, cargo delivery is slowed further by MAPs that obstruct and reduce motor protein processivity [Seitz et al., 2002]. An order of magnitude difference in transit time can be critical for time-limited processes, such as activity-dependent transport of newly expressed mRNAs from the soma [Steward & Worley, 2001, Grooms et al., 2006], where local protein synthesis can participate in long-term synaptic plasticity, but only in a narrow time window during or shortly after induction [Sutton & Schuman, 2006]. Therefore, modification of microtubule organization, for example, caused by aging as our work shows, could be regulating these time-limited processes.

A series of trafficking experiments in conjunction with measurements of microtubule polarity could further elucidate the transport mechanisms within dendritic subtypes. Our observation that dendrites can have differential microtubule organization can be useful for interpreting time-lapse trafficking studies, where past reports found differential RNA transport velocities for long versus short dendrites [Davis et al., 1990], primarily anterograde kinesin-based transport in apical dendrites [Guillaud et al., 2003], and primarily distal end-directed displacements of plus-end tracking proteins [Stepanova et al., 2003]. Application of our results to research on the neuronal microtubule network should help to contextualize the flourishing number of motor protein and trafficking studies.

2.5 Supporting Information Methods

Primary culture preparation. Hippocampal cultures were prepared as described previously [Dombeck et al., 2003] from hippocampi of embryonic day 18 Sprague/Dawley or Fischer 344 rats (BrainBits LLC). Tissues were dissociated with Papain (Worthington Biochemicals, Lakewood, NJ) and mechanical trituration. The cultures were incubated in 5% CO_2 at 37 °C and half of the media was exchanged every 4 days. The media consist of 2% B-27 supplement in phenol red-free Neurobasal medium with 1mM GlutaMAX-1 (all from Invitrogen). Before imaging, the media was replaced with a buffer solution containing (in mM): NaCl, 135; KCl, 5; $MgCl_2$, 1; $CaCl_2$, 1.8, and HEPES, 20.

Nocodazole. For experiments with nocodazole, acute hippocampal slices were held under nylon grid anchors in an ACSF-filled glass-bottom dish (World Precision Instruments). During treatment, nocodazole was dissolved in DMSO (1% of ACSF volume) and added to the dish yielding a final concentration of 25 μM. Control slices were immersed in ACSF with only the DMSO solvent. The dish sat in room temperature and was continuously bubbled with 95% O_2 and 5% CO_2. Average SHG intensities were obtained from images obtained 10 min before and 40 min after drug application. Background estimated from adjacent empty regions was subtracted.

Numerical simulation. The second harmonic field $E_{2\omega}$ at a location (θ, ϕ, R) generated by dipoles lying parallel to the y-axis is described [Moreaux et al., 2000, Williams et al., 2005] by,

$$E_{2\omega}(\theta,\phi,R) \propto \beta E_{\omega}^{2}\frac{\sin\psi\vec{\psi}}{R}\int\int\int dx\,dy\,dz\,C(x,y,z)\,exp(i\,2\,\xi\,k_{\omega}\,z)$$
$$exp(\frac{-2(x^2+y^2)}{w^2}-\frac{2z^2}{w_z^2})exp(-ik_{2\omega}(z\cos\theta+x\sin\phi\sin\theta+y\cos\phi\sin\theta)) \quad (2.1)$$

where β is the dipole hyperpolarizability, ψ is the angle subtended from the y-axis, k is the wave vector, E_{ω} is the excitation field strength, w is the beam waist, ξ is the Gouy phase shift parameter, and *C(x,y,z)* is the spatial concentration of the second harmonic-generating dipoles. The term *C(x,y,z)* can be either positive or negative, depending on the orientation of the dipoles. In this formalism, the microtubule arrays lie along the y-axis and the excitation propagates along the z-axis. Forward-directed second harmonic intensity, the observable during most imaging experiments, would be proportional to the integral of $E_{2\omega}$ from $\theta = 0$ to $\pi/2$. This is an approximation because objectives do not collect all forward-directed second harmonic intensity. We have examined the far-field SHG intensity distribution (Fig. 2.9), which shows that most of the signal is emitted along the z-axis and thus would be collected by objectives with relatively high numerical apertures.

To interpret the second harmonic field, we note that intensity of the emitting field will depend on 1) the number of microtubules within the focal volume (reflected by the spatial integration of scatterer distribution *C(x,y,z)* and beam intensity profile exp(-$2(x^2+y^2)/w^2$-$2*z^2/w_z^2$)) and 2) the spatial arrangement of the microtubules (reflected by the spatial integration of *C(x,y,z)* and the Gouy phase anomaly exp(i*2*ξ*k*z)) especially if the spatial length scale is comparable to the wavelength, as in the case for microtubule spacings in neurites. Furthermore, because the excitation field strength E_{ω} and the hyperpolarizability β appear only outside the integral, ratios of intensities, $(E_{2\omega})^2$ would cancel these constants. This observation is useful for measurements because in situ determination of E_{ω} and β is difficult.

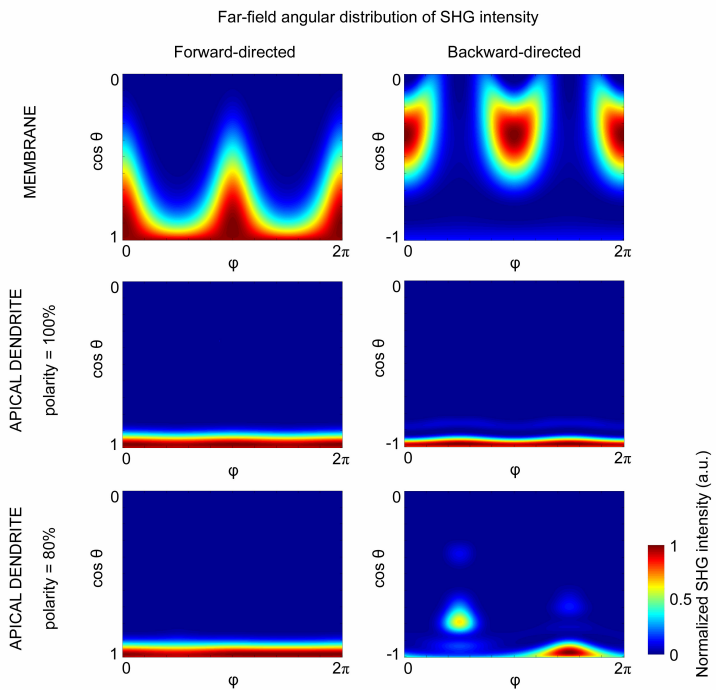

Figure 2.9: Simulated far-field angular distribution of SHG intensity for dipoles arranging in membrane and in dendrite configurations. The coordinate system is the same as described in Fig. 2.5A. Membrane is approximated as hexagonally-packed dipoles spaced 20 nm apart over a flat circular sheet with a diameter of 400 nm. In the forward-directed distribution, two peaks can be seen at $\theta = 22°$ and $\phi = 0°$ or 180°. This is in close agreement with $\theta = 28°$ obtained from analytical calculations by Moreaux et al. [Moreaux et al., 2000]. The difference can be explained by the numerical aperture of the excitation objective, 0.7, used in our simulation. Most of the forward- and backward-directed intensities are directed along the path of excitation. In the case of 80%-polarized apical dendrite, the angular distribution of backward-directed intensity is asymmetric and shows a side lobe. The asymmetry is due to uneven assignment of plus- and minus-end distal microtubules by computer during the simulation. In another simulation run, which would lead to a different assignment, the side lobe will be located at a slightly different θ.

To estimate E_ω and w, the excitation was approximated as a focused laser beam that has a Gaussian intensity profile and a Gouy phase shift across the focal plane [Moreaux et al., 2000]. We use numerical values obtained by fits to exact field calculations [Zipfel et al., 2003b]. The numerical aperture of the excitation objective, 0.7, is used for calculating w.

To approximate $C(x,y,z)$, a microtubule array was defined as a hexagonal close-packed grid of microtubules, each modeled as a linear array of dipoles. The inter-microtubule spacing was 22 nm for axons and 64 nm for dendrites [Chen et al., 1992]. The inter-dipole distance was 8 nm, the same as the longitudinal length of individual tubulin subunits. To verify that the result is insensitive to our structural assumptions, we performed simulations with shorter inter-dipole distances, with microtubule modeled as a ring of linear dipole arrays, analogous to protofilaments, and with arrays of square close-packed grid. These modifications yielded similar results so we opted for the simple geometry as described.

The calculation was implemented in MATLAB. We defined four classes of neurites: apical dendrites (spacing 64 nm, diameter 3 μm), basal dendrites (spacing 64 nm, diameter 1 μm), distal dendrites (spacing 64 nm, diameter 0.5 μm), and axons (spacing 22 nm, diameter 0.17 μm). The neurite diameters were obtained from literature [Fiala & Harris, 1999, Shephard & Harris, 1998]. In the case of apical dendrites, we confirmed the neurite diameter by measuring in the hippocampus and in the neocortex of adult *Thy1*-YFPH and obtained values of 2.7±0.5 μm and 2.9±0.4 μm respectively. For each type of neurite, we simulated and calculated the second harmonic intensity for a particular microtubule distribution. The distribution depends on the polarity, which the program used to set the orientation of each microtubule, plus-end or minus-end distal,

probabilistically. We repeat the simulation 100 times for each neurite type at polarity intervals of 5%.

The numerical simulation assumes that plus- and minus-end distal microtubules are randomly located within the neurite. However, it is also possible that there may be a bias for the locations of microtubules depending on their polarity. For example, if all the plus-end distal microtubules are located in the center of the neurite, whereas the minus-end distal microtubules are in the periphery, then the calculated SHG intensities will be drastically different. So far, studies [Chen et al., 1992, Takahashi et al., 2007] on the spatial organization of microtubules within neurites seems to suggest a hexagonally packed distribution with no strong bias on polarity, but this has not been verified in most types of neurons, especially from native tissues..

Error analysis. We determine the uncertainties when estimating the microtubule polarity. There are two sources of uncertainties: f/b SHG ratio measurement and numerical simulation. The uncertainty in the f/b SHG ratio measurement is estimated by the standard deviation of f/b SHG ratio (f/b ratio $\pm SD_{meas}$) measured from >10 neurites across the field of view. The uncertainty in the numerical simulation (Sim ratio $\pm SD_{sim}$) results from differing simulated f/b ratio in the various possible spatial distributions of microtubules. Both of these uncertainties are then propagated to estimate the error bounds of the polarity values using Fig. 2.5. We estimated that the upper error bound is the value when (Sim ratio SD_{sim}) is equal to (f/b ratio + SD_{meas}). Similarly, the lower error bound is the value when (Sim ratio + SD_{sim}) is equal to (f/b ratio SD_{meas}). Because of the nonlinear dependence of polarity on f/b SHG ratio, the error bounds are asymmetric.

CHAPTER 3

OPTICAL VISUALIZATION OF ALZHEIMER'S PATHOLOGY VIA MULTIPHOTON-EXCITED INTRINSIC FLUORESCENCE AND SECOND HARMONIC GENERATION*

Intrinsic optical emissions, such as autofluorescence and second harmonic generation (SHG), are potentially useful for functional fluorescence imaging and biomedical disease diagnosis for neurodegenerative diseases such as Alzheimer's disease (AD). Here, using multiphoton and SHG microscopy, we identified sources of intrinsic emissions in *ex vivo*, acute brain slices from AD transgenic mouse models. We observed autofluorescence and SHG at senile plaques as well as characterized their emission spectra. The utility of intrinsic emissions was demonstrated by imaging senile plaque autofluorescence in conjunction with SHG from microtubule arrays to assess the polarity of microtubules near pathological lesions. Our results suggest that tissues from AD transgenic models contain distinct intrinsic emissions, which can provide valuable information about the disease mechanisms.

3.1 Introduction

Alzheimer's disease (AD) is a prevalent neurodegenerative disease for which there is no known cure. Patients usually suffer from dementia, along with other behavioral changes, so examinations on memory and cognitive abilities are standard tests for diagnosing AD. However, confirming the initial diagnosis of the actual cause of dementia is often difficult. Definitive confirmation is possible with post-mortem autopsy, where histology on brain tissues reveals senile plaques and neurofibrillary tangles

*Originally published as: Kwan, A. C., Duff, K., Gouras, G. K., Webb, W. W. (2009). "Optical visualization of Alzheimer's pathology via multiphoton-excited intrinsic fluorescence and second harmonic generation," Opt Express 17, 3679-3689

(NFT), the two hallmark pathological lesions in AD. As a result, there are strong incentives to develop reliable methods for early diagnosis of AD. To address this need, new approaches are being developed. Positron emission tomography (PET) imaging of Pittsburgh Compound-B has been shown to bind amyloid-beta deposits in human patients *in vivo* [Ikonomovic et al., 2008]. Optical imaging with amyloid-beta deposit-specific near-infrared optical probes is being developed and has generated some successes in transgenic mouse models [Hintersteiner et al., 2005]. These new imaging approaches use exogenous compounds that can selectively label pathological lesions and therefore enhance signal-to-noise. Alternatively, endogenous optical signals may also provide contrast between AD and normal tissues. For example, one recent study [Hanlon et al., 2008] reports that transmission and reflectance spectra in near-infrared region from unstained *in vitro* tissue slab samples may be useful in distinguishing AD from normal tissues, although the molecular origin of this observation was not specified. Interpreting this type of studies is difficult due to a lack of information about intrinsic emissions from AD tissues, which has only been recently investigated in detail in normal tissues [Zipfel et al., 2003a].

It is generally known that brain tissues contain various endogenous proteins that can generate autofluorescence and/or second harmonic emissions. It is possible that these endogenous optical signals can provide contrast between normal and AD tissues. Moreover, if applied to AD tissues, intrinsic emissions may provide functional information that is useful in understanding the disease mechanisms. For example, fluorescence from NAD(P)H, an electron carrier that is crucial in metabolic pathways, has been used to investigate the dynamics of functional brain energy metabolism [Kasischke et al., 2004, Vishwasrao et al., 2005]. Second harmonic generation (SHG) emitted from microtubules has been used to map the distribution of polarized microtubule arrays in acute brain tissues from mice of various ages [Dombeck et al., 2003, Kwan et al., 2008].

There have been several reports on autofluorescence from AD-related lesions. An early paper from Dowson [Dowson, 1981] described autofluorescence from senile plaque in the brain tissues from human patients. Using tissues embedded in paraffin wax and sectioned thinly, he described a blue autofluorescence (greater than 430 nm) from senile plaques that were excited with ultraviolet light. This observation was confirmed by a more recent study [Thal et al., 2002], which also studied human AD tissues. For transgenic mouse models, one study [Diez et al., 2003] has reported that a particular mouse model that overexpresses human mutant amyloid precursor protein (APP) contain intrinsically fluorescent senile plaques. Lastly, several years ago, our group and collaborators have reported that NFTs in human AD brain tissues can generate a blue autofluorescence that has an emission peak at ≈460 nm [Zipfel et al., 2003a].

Because the previous studies used wide-field [Dowson, 1981, Thal et al., 2002] or confocal microscopy [Diez et al., 2003] on post-mortem or fixed brain tissues, they are restricted to superficial areas or thinly-sectioned preparations. Furthermore, dead or fixed tissues lose intrinsic emissions that could originate from live cells, such as autofluorescence from NAD(P)H and SHG from microtubules. Here, we use multiphoton microscopy [Denk et al., 1990, Zipfel et al., 2003b] to investigate the various sources of intrinsic emissions, including from senile plaques, from transgenic AD mouse models. We demonstrate the utility of these intrinsic emissions by assessing the polarity and morphology of dendritic microtubule arrays near senile plaques and finally, discuss how endogenous signals may be useful for AD diagnosis.

3.2 Materials and Methods

TPF and SHG microscope. Imaging was performed on a custom-built TPF microscope based on a commercial laser beam scanning unit (Bio-Rad MRC 1024) and an inverted microscope (Olympus, IX-70). Trains of laser pulses at 80 MHz and ≈100 fs duration were generated by a mode-locked Ti:Sapphire laser (Spectra-Physics Tsunami), which was pumped by a 5 W diode laser (Spectra-Physics Millennia). Intensity and polarization were controlled by a Pockels cell (Conoptics 350-50) and a Berek compensator (New Focus 5540). The beam was focused onto the sample by an Olympus UApo/340 20X/NA 0.7 water immersion objective, which also collected the epi-fluorescence. The transmitted SHG was collected by an Olympus XLUMPlanFl 20X/NA 0.95 dipping objective. The average power after the objective was ≈70 to 130 mW. For imaging, samples were excited at 774 nm and signals were detected with bi-alkali PMTs (Hamamatsu HC125-02). SHG was collected behind a focusing lens, an IR-blocking short-pass dichroic and a narrowband emission filter, centered at 387 nm (Semrock FF720 and FF01-387/11). Autofluorescence was collected from 400 to 550 nm behind a blue glass filter (Chroma BGG22). Emission spectra were obtained using a liquid nitrogen-cooled CCD spectrometer (Jobin Yvon Spex270M). The spectrometer was coupled to the microscope via an optical fiber replacing the usual bi-alkali photomultiplier in the transmission-direction. To collect one spectrum, a small square area ≈50 μm wide was continuously scanned at high zoom for 10 s. To reduce photodamage, excitation wavelength was set at 830 nm and average power was reduced to ≈25 mW. Dark counts were subtracted by acquiring a blank spectrum with shutter closed. The spectrometer was calibrated with collagen SHG spectra collected from a rat tendon sample.

Tissue preparation. Acute brain slices were prepared from 12 mice, including one with APP Swedish mutation [Hsiao et al., 1996] (obtained from G. K. Gouras), two

with APPSwe/PS1 double mutations [Borchelt et al., 1997] (ordered from Jackson Laboratory), two with APPSwe/TauJNPL3 double mutations [Lewis et al., 2001] (obtained from K. Duff), and three with APPSwe/PS1/Tau triple mutations [Oddo et al., 2003] (obtained from G. K. Gouras), and four wild-type mice. All mice were at least 1-year old. All preparations were performed in accordance with Cornell University animal use regulations (Institutional Animal Care and Use Committee protocol 00-46-03).

To prepare acute slices, we removed the brain following CO_2 euthanasia. Immediately, the brain was dipped in iced artificial cerebrospinal fluid (ACSF) composed of (in mM): NaCl, 120; KCl, 2.5; NaH_2PO_4, 1; $MgSO_4$, 1.3, $NaHCO_3$, 25; D-glucose, 10; $CaCl_2$, 2.5, that was saturated with 95% O_2 and 5% CO_2. Transverse hippocampal slices 300 to 400 μm thick were cut using a vibratome (Campden Instruments). Slices were then incubated in oxygenated ACSF at 35 °C for 1 hr. During imaging, slices were held under nylon grid anchors in a flow chamber (Warner Instruments) and perfused with oxygenated ACSF at room temperature.

After imaging the intrinsic emissions from unstained brain slices, AD pathology was verified by Thioflavin-S or BTA-1 staining of senile plaques. Brain slices were fixed in 4% paraformaldehyde in PBS in the refrigerator overnight. Next the slices were incubated for 1-2 hours in Thioflavin-S (Sigma, 0.0005-0.001% by weight in PBS), or 40 μM BTA-1 (Sigma, 40 mM in DMSO then diluted 1:1000 in PBS), and then rinsed three times in PBS. During imaging, the slices were placed in 35 mm glass-bottom dishes (Warner Instruments).

3.3 Results

Autofluorescence and SHG in acute brain slices of AD mouse models. Acute hippocampal slices from transgenic AD mouse models show a distinct pattern of autofluorescence and SHG emissions (Fig. 3.1). Four sources of emissions can be identified by morphology: senile plaques, lipofuscins, microtubules, and blood vessels. Senile plaques appear as spherical objects with diameter ≈30-70 μm that emit a diffuse autofluorescence. Lipofuscin is small, bright, and densely packed along the pyramidal cell layers. Microtubules are only visible in the SHG channel and are most visible in regions adjacent to the cell layers [Dombeck et al., 2003, Kwan et al., 2008]. Blood vessels are sparse and tend to branch with Y-shaped junctions [Kwan et al., 2008]. When comparing AD mouse models to wild-type mice, autofluorescence from senile plaques is unique to the transgenic models.

Previous studies have reported senile plaque autofluorescence in thin tissue slices, including from both native and fixed "smear preparations" from human brain [Thal et al., 2002] or 10 to 20 μm-thick sections prepared for immunohistochemistry [Dowson, 1981, Diez et al., 2003]. Here we found autofluorescence from senile plaques in 400 μm-thick native brain slices, a much thicker sample, by using multiphoton microscopy, which is more suited for imaging in highly scattering tissues [Denk et al., 1990]. We used acute slices that were prepared fresh from transgenic animal models, perfused continuously with oxygenated ringer, and used within ≈5 hr; therefore, this preparation represents an *ex vivo* tissue model that most accurately resembles *in vivo* tissues. Because acute slices preserve healthy neurons, they are the standard *ex vivo* preparation for experiments such as patch-clamp recordings of neurons [Sakmann & Stuart, 1983]. Intrinsically fluorescent senile plaques were observed

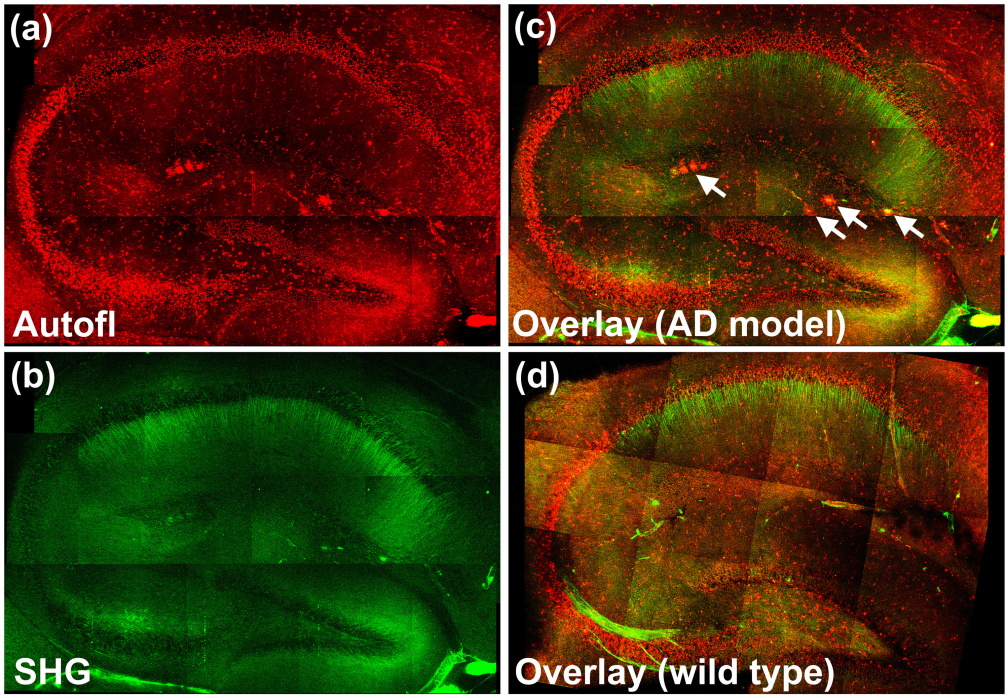

Figure 3.1: Autofluorescence and second harmonic emissions from acute hippocampal brain slice of transgenic Alzheimer's disease mouse models. (a) Autofluorescence, (b) second harmonic emissions, (c) and their overlay of the hippocampus of a 17-month old APPSwe/TauJNPL3 mouse. Senile plaques emit autofluorescence (white arrows) that were morphologically distinct from other sources of intrinsic emissions and were missing from wild-type animals, as shown in (d). Each panel is a mosaic of z-projections of a 50 μm thick image stack acquired in 10 μm steps. Multiphoton excitation wavelength = 774 nm, circular polarization.

in acute slices from all transgenic mouse models examined. Moreover, this type of autofluorescence can be observed in acute slices >100 μm below the surface.

To confirm the identity of the intrinsically fluorescent structures that morphologically resemble senile plaques, after imaging we fixed the brain slices and stained with plaque-specific dyes Thioflavin-S or BTA-1. Figure 3.2 compares unstained and stained plaque-burdened regions to show that the autofluorescence originates from senile plaques. Interestingly, a small amount of SHG emission was also seen to be generated by senile plaques.

The number density of intrinsically fluorescent senile plaques is highly variable between different mice, possibly due to the variable stages of disease progression. All mice showed substantial numbers of intrinsically fluorescent senile plaques in the entorhinal cortex and a lesser amount in the neocortex. Senile plaques tend to be sparse or absent in area CA1 in the hippocampus, although a fair number of plaques could be seen in an 18-month-old APPSwe2756/PS1 mouse that was probably in an advanced disease state.

We tested whether our preparation methods could affect the quality of autofluorescence. Senile plaque autofluorescence was seen in slices that were imaged immediately following dissection, i.e. without the 1-hour incubation period. Moreover, the autofluorescence persists after overnight fixation in formaldehyde.

Lipofuscins appeared as small, bright specks in all areas of the brain, but were especially numerous along the CA1 and CA3 layers in the hippocampus. We compared the number density of lipofuscins between transgenic and wild-type mice at similar ages, but found no statistically significant differences (data not shown), which agrees with a published study [Drach et al., 1994]. Finally, our group has previously reported [Zipfel et al., 2003a] that NFTs in human AD brain tissues are intrinsically fluorescent,

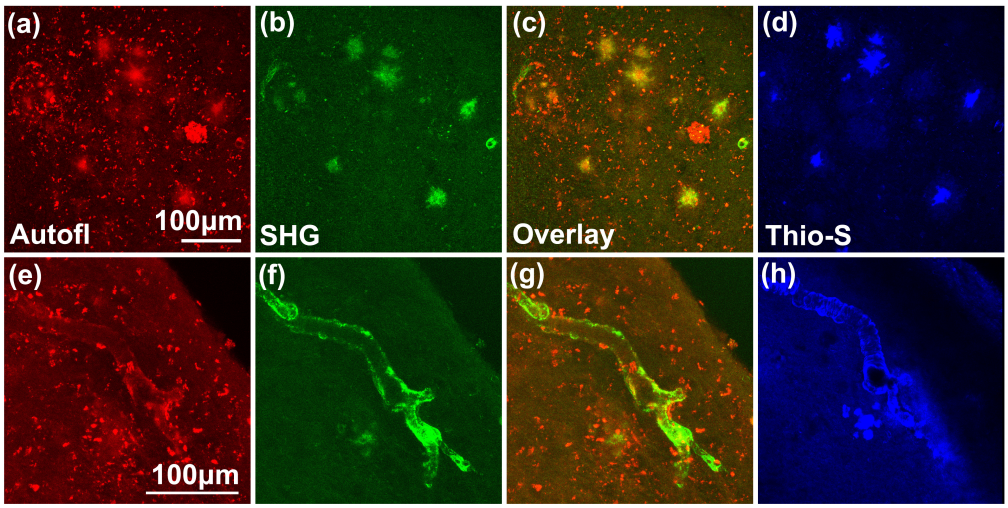

Figure 3.2: Senile plaques emit autofluorescence and second harmonic signal. (a) Autofluorescence and (b) second harmonic emissions detected in the entorhinal cortex in acute slices of a 22-month old APP-Swe/TauJNPL3 mouse. (c) Overlay of (a) and (b) shows the same large, round structures (appears as yellow in the overlay) emit both the autofluorescence and second harmonic signals, which were then identified to be senile plaques when (d) this brain slice was subsequently fixed and stained with the plaque-specific dye Thioflavin-S. The small, bright specks were lipofuscins, which did not generate second harmonic emission. (e-h) Autofluorescence and second harmonic signal, of unknown molecular origin, were also detected near a blood vessel that was affected by cerebral amyloid angiopathy. Signal could be emitted from a source similar to that in senile plaque or from collagen. Each panel is a z-projection of a 40 to 60 μm thick image stack acquired in 3 or 4 μm steps. Multiphoton excitation wavelength = 774 nm, circular polarization.

but we have not been able to find such examples in our APPSwe/PS1/Tau transgenic models that have been reported to contain NFTs [Oddo et al., 2003]. The lack of autofluorescence here does not necessarily imply a negative result: the mice examined in this work could be at relatively early stages of disease, or they may lack particular tangle pathologies when compared to human tissues. These ideas are addressed in detail in Section 3.4.

Emission spectrum of autofluorescence from individual senile plaques. The emission spectrum of senile plaque autofluorescence has not been determined before, presumably because the structures are relatively small and bulk tissues contain other sources of intrinsic emissions. We overcome these problems by relying on multiphoton microscopy's micron-scale axial and lateral spatial resolution, which enable us to scan a single plaque and obtain a clean emission spectrum of the autofluorescence (Fig. 3.3). The emission spectrum is broad and peaks at ≈525 nm. This measurement agrees with general statements about "blue autofluorescence" from previous reports [Dowson, 1981, Thal et al., 2002, Diez et al., 2003]. Qualitatively, we observed that the senile plaque autofluorescence can be multiphoton-excited from ≈720-860 nm. Moreover, a second emission peak can be seen at exactly half of the excitation wavelength. The wavelength and the narrow width imply that this second emission peak is due to SHG. The second harmonic nature of this emission peak was confirmed by a corresponding blue shift when the excitation wavelength was lowered.

In an adjacent region with no plaque, the detected emission is significantly weaker and seems to contain multiple broad peaks. It is likely that lipofuscins contribute to emissions at higher wavelengths and possibly NAD(P)H or flavins contribute to emissions below 500 nm (cf. [Zipfel et al., 2003a]). Comparing the spectra obtained at senile plaques and from adjacent regions showed that autofluorescence can be distinguished

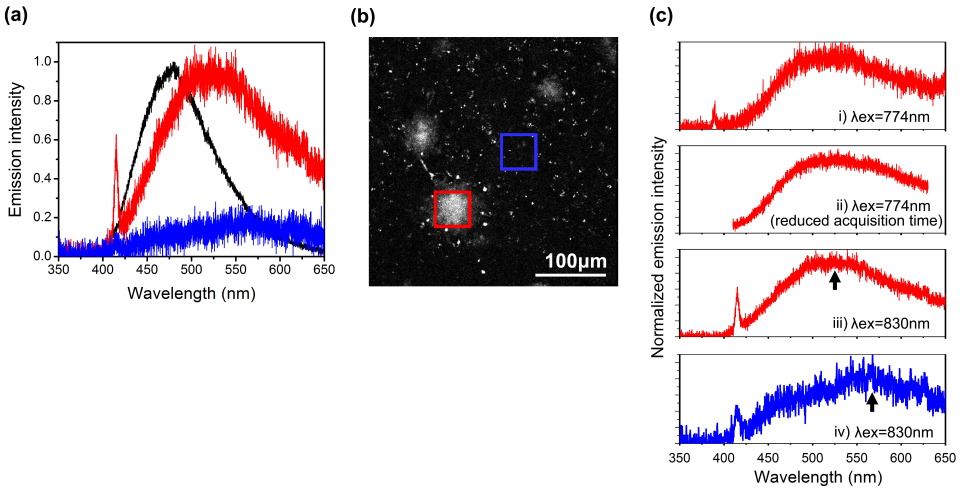

Figure 3.3: Typical emission spectra of senile plaque autofluorescence. (a) The emission spectra of a senile plaque (red trace) and of an adjacent plaque-free region (blue trace) were measured 50 μm beneath the surface of an acute slice from an 18-month-old APPSwe mouse. A typical emission spectrum of the senile plaque autofluorescence, excited at 830 nm, peaked at ≈520 nm and showed detectable SHG emissions at 415 nm. After acquiring the spectra, this brain slice was fixed and stained with Thioflavin-S. Emission spectrum of one Thioflavin-S-stained senile plaque, obtained at ≈10 times less power and 10 times less acquisition time as the autofluorescence, is shown (black trace, normalized) for comparison. (b) The region in the neocortex of the acute slice where the spectra (red and blue boxes) were taken for (a). (c) The emission spectra for four different conditions recorded from the same mouse: i) emission spectrum at senile plaque, excited at 774 nm; ii) emission spectrum at a different senile plaque, excited at 774 nm, but with quick acquisition to reduce photodamage; iii) emission spectrum at another senile plaque, excited at 830 nm; iv) emission spectrum at a plaque-less location, dominated by autofluorescence, presumably from lipofuscin because of the high emission wavelength. Second harmonic peak in iv) is exaggerated because emission intensity was re-scaled. Arrows indicate the locations of the peak emission wavelengths for the autofluorescence.

from the background by the emission spectrum. We also obtained the emission spectra of senile plaques that were stained with Thioflavin-S following formaldehyde fixation. The Thioflavin-S fluorescence has a relatively narrow spectrum that peaked at ≈480 nm, which is distinct from the autofluorescence emission obtained from unstained brain slices. Thioflavin-S fluorescence in stained brain slices was significantly brighter than the autofluorescence in unstained brain slices. There was significant difference between the peak emission wavelength and spectral shape of the emissions recorded at plaques from Thioflavin-S-stained and unstained brain slices. This difference confirms that the autofluorescence in unstained brain slices is not fluorescence resulting from Thioflavin-S contamination.

Functional imaging of intrinsic emissions in AD mouse models. To demonstrate the utility of intrinsic emissions, we imaged SHG emissions from polarized microtubules and autofluorescence from senile plaques to investigate whether the polarity or the morphology of microtubule arrays are affected in AD mouse models. Tau, a microtubule-associated protein, has been implicated as a possible cause for neurodegeneration [Ballatore et al., 2007]. Electron microscopy studies have shown that tau can accumulate in postsynaptic locations [Takahashi et al., 2002, Takahashi et al., ress], and therefore can possibly affect microtubule organization in the dendrites. In neuronal culture models of AD, manipulation of tau expressions or mutations show that microtubules can be depolymerized [Li et al., 2007, Qiang et al., 2006], or be forming a star-shaped aster array after reversing polarity [Shemesh et al., 2008]. Such modifications to the microtubule arrays as formation of a star-shaped structure should drastically alter morphology and be directly observable by our imaging technique because SHG emission is a good qualitative indicator of the polarity and number density of microtubules in single neurites [Dombeck et al., 2003, Kwan et al., 2008].

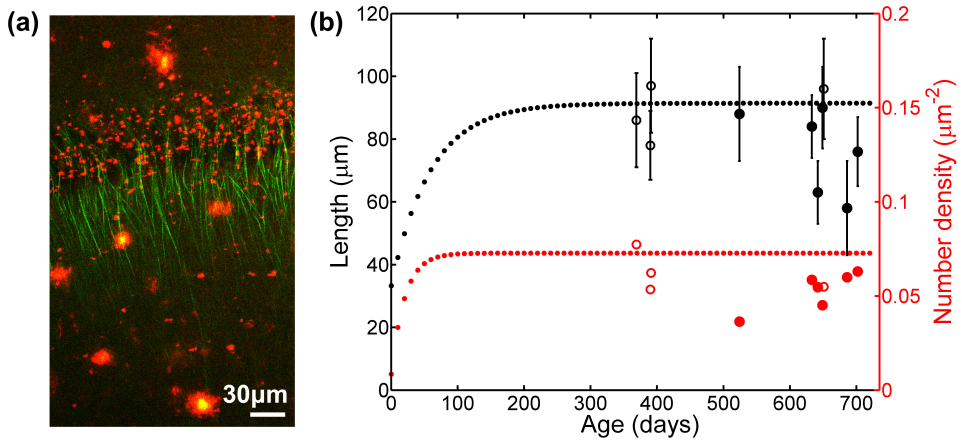

Figure 3.4: Length and number density of polarized microtubule arrays in area CA1 in Alzheimer's disease mouse models. (a) Typical autofluorescence (red) and second harmonic emissions (green) in area CA1 from an acute slice of a 21-month-old APPSwe/PS1 mouse. This image is a z-projection of an 18 μm thick image stack acquired in 3 μm steps. Multiphoton excitation wavelength = 774 nm, linear polarization. (b) The length and number density of polarized microtubules in area CA1 of Alzheimer's disease mouse models (solid dots) and of wild-type mice studied that were over 1 year old (hollow dots). The dotted lines show the trend based on data from a larger set of wild-type mice from our previous study [Kwan et al., 2008].

We initially tested whether it is possible to observe SHG emissions from microtubules near senile plaques stained with Thioflavin-S or BTA-1. We found that even a small amount of plaque-specific dye would emit too much fluorescence, and therefore obscures intrinsic emissions. Therefore, in all of the following imaging experiments, we chose to use unstained brain slices. In unstained acute slices, we were able to image simultaneously intrinsic emissions from polarized microtubules in apical dendrites in area CA1 and senile plaques (Fig. 3.4). We measured the length and number density of polarized microtubules in this region, using a previously described procedure [Kwan et al., 2008]. We found that the length of polarized microtubule arrays

is 77±13 μm (n=6 transgenic AD models) versus 89±9 μm (n=4 wild-types) and the number density is 0.053±0.010 μm^{-2} versus 0.062±0.011 μm^{-2}. These differences are not statistically significant, although our sample size is small. Interestingly, the three mice that showed the shortest microtubule arrays were the mice with the triple APP-Swe2756/PS1/Tau mutations. However, those same mice were also older than most of the mice examined and there were only data from one wild-type littermate of similar age.

When focusing on a single senile plaque, we can resolve the polarized microtubule arrays within individual apical dendrites of CA1 pyramidal neurons (Fig. 3.5). There have previously been studies [Spires et al., 2005, Tsai et al., 2004, Grutzendler et al., 2007, Alpár et al., 2006] on the morphology of axons and dendrites near a senile plaque. Reported abnormal features in neurite morphology include loss of dendritic spines [Spires et al., 2005, Tsai et al., 2004], shaft atrophy [Grutzendler et al., 2007], varicosity and sprouting [Tsai et al., 2004]. Axons and dendrites seem to be affected differently such that axons frequently have varicosities, which are not seen as often in dendrites [Grutzendler et al., 2007]. Moreover, there have been conflicting observations as to whether the length or diameter of dendrite shafts are affected [Tsai et al., 2004, Alpár et al., 2006]. One common theme is that the amount of abnormal features tends to increase dramatically within a ≈15-40 μm-diameter region around the senile plaque [Tsai et al., 2004].

Our observations found that SHG emissions from polarized microtubule arrays in apical dendrites are mostly unaffected by the presence of a senile plaque. We did not find polarized microtubules that traverse through the central core of the plaque, but most apical dendrites were unaffected at the periphery of the autofluorescence. In contrast, unhealthy dendrites, with a zigzag trajectory, could be found near the tissue surface due

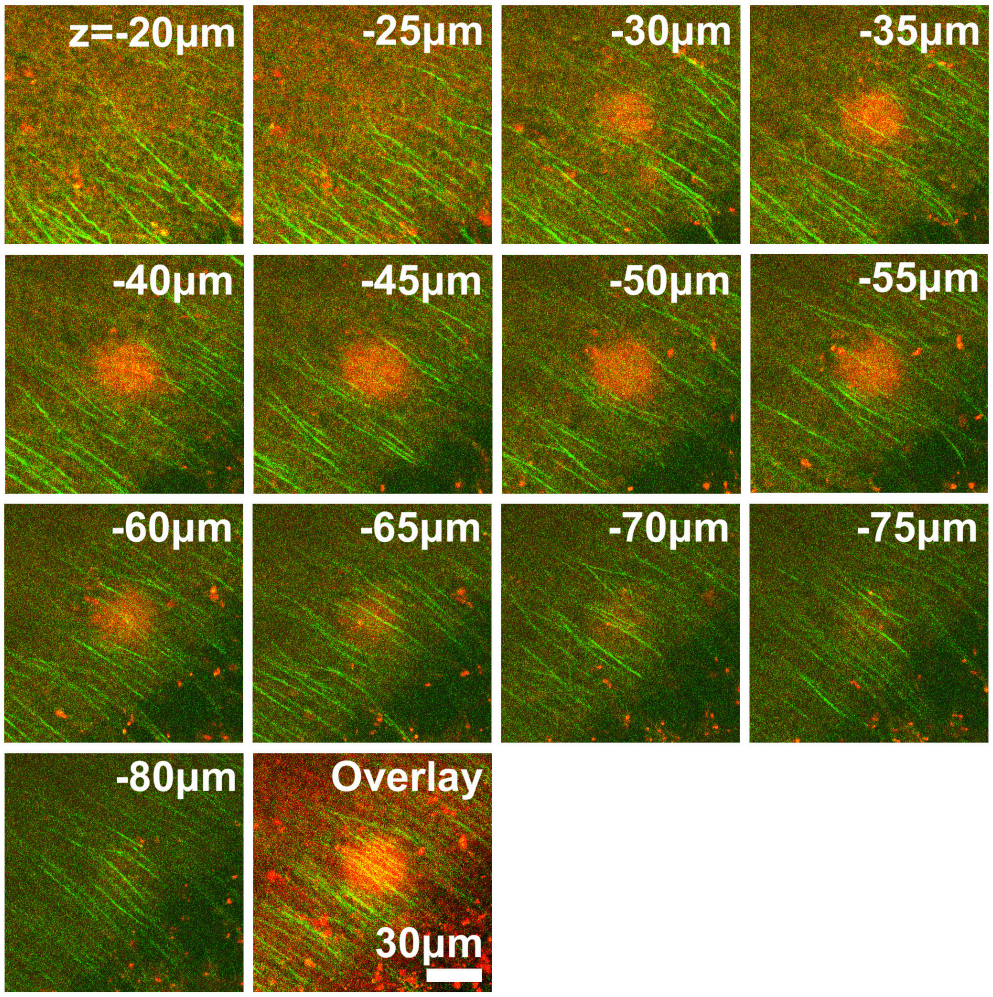

Figure 3.5: Polarized microtubules in apical dendrites near a senile plaque. A series of images shows second harmonic emissions from polarized microtubules of apical dendrites (green) near an autofluorescent senile plaque (red). The z value denotes the distance to the slice surface. The senile plaque was located in the area CA1 in the hippocampus in an acute slice from a 17-month old APPSwe/TauJNPL3 mouse. Multiphoton excitation wavelength = 774 nm, circular polarization.

to damage during sample preparation (z=-20 μm in Fig. 3.5). We attempted to look at SHG emissions from axonal microtubules, which have been observed before in the mossy fiber [Dombeck et al., 2003, Kwan et al., 2008], but in all of our experiments, we failed to find a senile plaque in that region. Moreover, we found no significant difference in the intensity of dendritic SHG emissions near or far from the senile plaques. Taken all together, our observations suggest that the polarity and the morphology of dendritic microtubule arrays do not seem to be affected adversely in these transgenic AD mouse models. However, apical dendrites are relatively thick ($\approx$3 μm in diameter), so they may be more tolerant to the kind of damages that were seen in previous studies.

3.4 Discussion

We have shown that autofluorescence and SHG emissions can be excited and imaged by multiphoton microscopy in acute brain slices of transgenic AD mouse models. More specifically, we confirmed that senile plaques exhibit autofluorescence with a distinct emission spectrum and also weakly generate SHG. This autofluorescence was seen in all four of the transgenic mouse models examined; therefore suggesting this type of intrinsic emission is a general property. This ability to identify senile plaques by their autofluorescence enables an array of possible functional studies using other intrinsic emissions, which we demonstrated by imaging SHG from dendritic microtubule arrays near senile plaques.

Previous studies that use multiphoton microscopy in AD mouse models focus on imaging dye-stained senile plaques. In a pioneering study [Christie et al., 2002], Christie et al. developed a thinned skull preparation in mouse that allows for imaging of senile plaques over several months. This success was followed by other *in*

vivo time-lapse studies, which use other complementary techniques such as neurite tracing [Spires et al., 2005, Tsai et al., 2004], calcium imaging [Eichhoff et al., 2008], astrocyte stains [Takano et al., 2007], or direct application of drugs and antibodies [Bacskai et al., 2001] to obtain additional insights on the disease. Here, we showed that weaker intrinsic emissions can also be imaged effectively in AD mouse tissues. This opens the door for new approaches for functional imaging of other intrinsic emissions, such as NAD(P)H metabolic imaging, to be used to study the pathological mechanisms of AD.

Although not demonstrated here, it may be possible to use autofluorescence as a diagnostic tool for *in vivo* studies in transgenic mouse models. Our study shows that autofluorescence from senile plaques is weak but clearly detectable and has a characteristic multiphoton-excited emission spectrum. One possible diagnostic method deep within the brain is to use gradient-index (GRIN) lenses [Zipfel et al., 2003b, Jung & Schnitzer, 2003] or optical fiber bundles [Gobel et al., 2004] to excite and collect autofluorescence from a small volume within the brain. Imaging may not be required, since spectral information will be the key for distinguishing AD versus normal tissues.

In our imaging-only results, senile plaques and lipofuscin have broad emission spectra so we distinguish them by morphology. In terms of size, senile plaques have diameters $\approx$10 times larger than lipofuscin. This size difference can be clearly resolved in multiphoton microscopy images, which have sub-micron spatial resolution within scattering tissues. In some cases, lipofuscin can "clump" together to form larger structures. However, in those cases, multiphoton microscopy images can still clearly resolve individual, smaller-diameter lipofuscins (see Fig. 4a in [Zipfel et al., 2003a]). On the other hand, it is unlikely to find small, nascent plaques. Plaques grow quickly *in vivo* within

1-3 days to their full size [Christie et al., 2002, Meyer-Luehmann et al., 2008]. Therefore, finding nascent plaques is a rare occurrence even in animal models with significant plaque load [Meyer-Luehmann et al., 2008].

We have characterized the emission spectrum of senile plaque autofluorescence. Previous studies [Dowson, 1981, Thal et al., 2002, Diez et al., 2003] have used excitation and detection at a variety of wavelengths, so knowledge of the emission spectrum will be useful for more sensitive detection. As a quick test to find the molecular origin of this autofluorescence, we tested solutions of A-beta fibrils, in which fibrils were verified with transmission electron microscopy, and saw no one-photon-excited fluorescence in a standard fluorimeter. This initial observation suggests that senile plaque autofluorescence is unlikely to originate from A-beta, which is the principal component of senile plaques [Atwood et al., 2002]. Many other materials are known to exist within senile plaque [Atwood et al., 2002] and can contribute to the intrinsic emission.

Autofluorescence from NFTs has been described before in post-mortem human tissues [Zipfel et al., 2003a], but was not observed in the APPSwe/PS1/Tau models in this study. A previous report [Oddo et al., 2003] has shown that these mice are capable of generating Thioflavin-S-positive Tau-related lesions. The absence of autofluorescence from NFTs in our work could be due to two reasons: One, the previous report [Oddo et al., 2003] observed Thioflavin-S-positive lesions in 12-month old homozygous mice, which may be at a more advanced stage of AD than our ≈20-month old heterozygous mice. This argument is supported by the observation that Thioflavin-S did not stain any structures that resemble Tau-related lesions in our acute slices. Two, it is possible that the only types of human Tau pathology that exhibit autofluorescence have no analogs in the APPSwe/PS1/Tau transgenic mouse model. To distinguish between these possibilities, more research would be required on characterizing autofluorescence and

immunoreactivity from various kinds of Tau-related lesions in human and transgenic mouse model tissues.

Intrinsic emissions such as autofluorescence and SHG are useful indicators for detecting the presence of pathological lesions. Changes in the intensity and spectrum of intrinsic emissions have previously been studied as possible diagnosis methods for tumors [Zhu et al., 2008] or skin pathology [Palero et al., 2006], and can potentially also be useful for neurodegenerative diseases. Here we have demonstrated that intrinsic emissions, particularly that of senile plaques, can be detected from relatively thick, native tissues. Furthermore, the senile plaque emission spectrum is distinct from the background to possibly further enhance detection sensitivity. We anticipate that this work will be useful for interpreting future studies that aim to use endogenous optical signals as a diagnostic tool or as functional fluorescent indicators.

CHAPTER 4

ACTIVITY OF HB9 INTERNEURONS DURING FICTIVE LOCOMOTION IN MOUSE SPINAL CORD*

Hb9 interneurons (Hb9 INs) are putative components of the mouse spinal locomotor central pattern generator (CPG) and candidates for the rhythm-generating kernel. Recent studies in slices and hemisected spinal cords showed that Hb9 INs display TTX-resistant membrane potential oscillations, suggesting a role in rhythm generation. To further investigate the roles of Hb9 INs in the spinal locomotor CPG, we used two-photon calcium imaging in the intact mouse neonatal spinal cord to record the activity of Hb9 INs, which were subsequently stained for unambiguous genetic identification. We elicited fictive locomotion by transmitter application or by electrically stimulating the caudal tip of the spinal cord. While most Hb9 INs were rhythmically active during fictive locomotion, their activity was sparse and they failed to fire with each cycle of the episode. If Hb9 INs are the principal pacemakers of the CPG, they should direct the firing of motor neurons with their activity preceding that of the ventral roots. Instead, during each cycle, onset of Hb9 IN activity lagged behind the onset of the ipsilateral ventral root burst by a mean phase of 0.21 during electrical stimulation and 0.28 during transmitter application (each locomotor cycle normalized in phase from 0 to 1). Whole-cell recordings from GFP+ cells in intact and hemisected spinal cords confirmed the imaging results. Our data suggest that Hb9 INs participate in fictive locomotion, but the

*To be submitted as: Kwan, A. C., Dietz, S. B., Webb, W. W., Harris-Warrick, R. M. (2009). "Activity of Hb9 interneurons during fictive locomotion in mouse spinal cord."

delayed onset of activity relative to ipsilateral motoneurons suggests that Hb9 INs are unlikely to be the sole rhythm generating kernel of the CPG.

4.1 Introduction

Central pattern generators (CPGs) are neural networks that produce a regular rhythmic output to drive a repetitive motor activity [Marder & Bucher, 2001]. Interneurons that coordinate the rhythm and pattern of motoneuron outputs are components of the CPG. In vertebrate systems, the motor pattern for locomotion can be elicited in isolated spinal cords in vitro [Grillner, 2003, Kiehn, 2006]. This "fictive locomotion" can be evoked by transmitter application or electrical stimulation, and recorded as motoneuron burst firing in the ventral nerve roots. The cellular components of the locomotor CPGs have been characterized in vertebrates including lamprey, *Xenopus*, and zebrafish [Grillner, 2003, Roberts, 1998, Sillar, 1998, Fetcho et al., 2008], but the same level of detail has not been reached in mammals due to the difficulty of identifying cell types. However, transgenic mouse strains now make it possible to visualize and record from putative CPG neurons that express fluorescent proteins driven by promoters of different transcription factors [Kiehn, 2006].

The Hb9 interneurons (Hb9 INs) are a set of excitatory, ventromedial interneurons expressing the Hb9 transcription factor [Thaler et al., 1999, Wichterle et al., 2002, Hinckley et al., 2005, Wilson et al., 2005]. They have several rhythmogenic characteristics: they fire rhythmically in phase with the ipsilateral ventral root during chemically-induced rhythmic activity in the isolated hemicord [Hinckley et al., 2005], and display TTX-resistant, voltage-dependent membrane potential oscillations in the presence of NMDA, serotonin (5-HT) and dopamine in spinal cord slices [Wilson et al., 2005, Gordon & Whelan, 2006, Ziskind-Conhaim et al., 2008]. Because they were the first

genetically identified neurons that have oscillatory properties in the spinal cord, Hb9 INs are attractive candidates for participation in the rhythm generating kernel of a pacemaker-driven CPG [Hinckley et al., 2005, Wilson et al., 2005, Kiehn, 2006, Wilson & Brownstone, 2008, Ziskind-Conhaim et al., 2008]. However, these results were not obtained in whole spinal cords with intact locomotor networks.

Calcium imaging can monitor the activity of neurons in an intact cord during fictive locomotion [Bonnot et al., 2002, Bonnot et al., 2005]. In collaboration with the Brownstone group, we have shown that ventromedial interneurons can be labeled with membrane-permeant calcium indicator dyes, and their activity monitored relative to the ventral root bursts [Wilson et al., 2007a, Wilson et al., 2007b]. In this Chapter, we have studied the activity of identified Hb9 INs during fictive locomotion evoked by both transmitter application and electrical stimulation of the caudal tip of the spinal cord [Kjaerulff & Kiehn, 1996, Jiang et al., 1999, Whelan et al., 2000, Lev-Tov et al., 2000]. We have also developed a staining technique for distinguishing Hb9 INs from ectopically labeled cells in the intact spinal cord, allowing us to confirm the genetic identity of the imaged cells. We found that while the majority of Hb9 Ins are rhythmically active during fictive locomotion, the mean onset phase of Hb9 activity trails that of the ipsilateral ventral roots, both when a bout of fictive locomotion starts and on a cycle-by-cycle basis during fictive locomotion. Hb9 INs also fire sparsely, and usually fall silent during a continuing bout of electrically stimulated fictive locomotion. Our results argue against a model of Hb9 INs as the sole pacemaker cells for the locomotor CPG.

4.2 Materials and Methods

In vitro spinal cord preparation. Hb9-GFP (*mHB9-gfp 1b*) and Hb9-lacZ (*Hb9nlsLacZ*/+) transgenic mice were generated by Dr. Thomas Jessell (Columbia University) and donated to us by Dr. Robert Brownstone (Dalhousie University), then bred in mouse facilities at Cornell University. Crossing of the two heterozygous transgenic lines led to Hb9-GFP/lacZ mice that express both GFP and LacZ. These mouse lines were described previously [Arber et al., 1999, Wichterle et al., 2002, Wilson et al., 2005]. All preparations were performed in accordance with Cornell University Institutional Animal Care and Use Committee and National Institutes of Health guidelines. Neonatal (P1-P3) Hb9-GFP and Hb9-GFP/lacZ mice were used in this study. Mice were euthanized by decapitation and their spinal cords were removed by laminectomy [Kudo & Yamada, 1987, Jiang et al., 1999] in ice-cold (4 °C), oxygenated (95% O_2 / 5% CO_2) sucrose-based Ringer's solution (in mM: 206 sucrose, 2 KCl, 2 $MgSO_4$, 1.25 NaH_2PO_4, 1 $CaCl_2$, 1 $MgCl_2$, 26 $NaHCO_3$, 10 D-glucose) or low-calcium Ringer's solution (in mM: 111 NaCl, 3.08 KCl, 25 $NaHCO_3$, 1.18 KH_2PO_4, 3.8 $MgSO_4$, 0.25 $CaCl_2$, 11 D-glucose). The ventral meninges were removed near the midline in segments T11 to L3 while leaving the ventral roots intact. The cord was pinned, ventral-side up, in a Sylgard-filled dish and superfused with oxygenated (95% O_2 / 5% CO_2) normal mouse Ringer's solution (in mM: 111 NaCl, 3.08 KCl, 1.25 $MgSO_4$, 2.52 $CaCl_2$, 25 $NaHCO_3$, 1.18 KH_2PO_4, 11 D-glucose) at a flow rate of ≈6 mL/min. After dissection, the cord was incubated at room temperature for 1 hr prior to whole-cell recording or calcium indicator dye loading and imaging.

Fictive locomotion and ventral root recordings. Fictive locomotion was elicited using one of two methods: bath application of transmitters or electrical stimulation of the caudal tip of the spinal cord. In the chemical stimulation method, transmitters or

their agonists (9 μM NMDA, 12 μM 5-HT, 18 μM DA, unless otherwise specified) were added to the superfusing normal Ringer's solution. In the electrical stimulation method, a blunt, fire-polished stimulation electrode was used to suck up the caudal tip of the spinal cord including the coccygeal roots, and stimulated using a battery-operated stimulus isolator (A365, World Precision Instruments, Sarasota, FL) driven by a 30 s, 1 Hz train of 1 ms-duration square pulses generated using a function generator (DS345, Stanford Research Systems, Sunnyvale, CA). The threshold current to reliably elicit fictive locomotion episodes was empirically determined, typically 10-50 μA, and the cord was allowed to rest for at least 3 min between consecutive stimulation episodes. To record motoneuron activity extracellularly from the ventral roots, suction electrodes were attached onto two ventral roots, typically left and right L1 or L2. Electrical signals were sent to an AC amplifier (1700, A-M Systems, Carlsborg, WA), filtered between 100 Hz to 1 kHz, and recorded by a digitizer (Digidata 1322A, Axon Instruments) using the pCLAMP 8 software (Axon Instruments).

Calcium indicator dye loading. A dye solution of Fluo-3 AM was prepared as described by Garaschuk et al. [Garaschuk et al., 2006]. Briefly, a solution of 10 mM Fluo-3 AM (Invitrogen) and Pluronic F-127 (20% by weight, Invitrogen) was prepared in DMSO (Sigma-Aldrich). This solution was diluted 10-fold with a HEPES-based buffer solution (in mM: 150 NaCl, 2.5 KCl, 10 HEPES, at pH 7.3), filtered with a 0.22 μm centrifugal filter unit (Ultrafree-CL, Millipore), and backfilled into glass pipettes (outer diameter 1.5 mm, with filaments, Sutter Instruments, 1-4 MΩ). To label the spinal cord, a pipette was inserted 100-200 μm under the ventral surface using a micromanipulator (Burleigh) and under visual guidance using oblique illumination. During entry, a holding pressure of 4 psi was controlled by a Picospritzer (PV820, World Precision Instruments). To eject dye, 10-second pressure puffs at 10 psi were repeated 4-8 times. A total of 6-12 injection sites labeled the ventromedial region between T13 and L2. An

optimal labeling pattern was typically observed after 1 hr, when imaging began, and persisted for >6 hrs.

Two-photon microscopy. Our two-photon microscope is based on a Bio-Rad Radiance 2000 scan head mounted on an upright microscope (BX50WI, Olympus). Excitation was focused with an Olympus 40X/NA 0.8W-IR objective. The average excitation laser intensity was 20-40 mW. Epifluorescence was separated into two channels by a long-pass dichroic mirror (DCLP500, Chroma) and emission filters (BGG22 and 575/150, Chroma). Fluorescence below 500 nm was detected by a bialkali photomultiplier tube (HC125-02, Hamamatsu) and fluorescence above 500 nm was detected by a GaAsP photomultiplier tube (H7422, Hamamatsu). We used a method previously described to distinguish Fluo-3 from GFP fluorescence [Wilson et al., 2007b]. Briefly, to image calcium transients, both Fluo-3 and GFP fluorescence were excited at 800 nm and collected in the >500 nm channel. The change in Fluo-3 fluorescence would therefore reflect only qualitative changes in intracellular calcium concentration but could be easily imaged because GFP expression in these mice was relatively low. To identify GFP-labeled cells, the laser was tuned to 900 nm, where the two-photon action cross-section of Fluo-3 is low, and GFP fluorescence is collected exclusively in the <500 nm channel. Cascade blue was excited at 800 nm and detected using a different emission filter (390/60, Chroma). In time-lapse imaging, the field of view was reduced to 128-by-128 pixels to facilitate a scan rate of 4 to 9 Hz. To synchronize the images with electrical recordings, we used pCLAMP software to record TTL pulses that were generated by the Radiance control unit after each image frame was acquired.

Whole-mount staining of neurons that express LacZ. GFP expression in the Hb9-GFP line is leaky, with expression not only in Hb9-expressing motoneurons and interneurons, but also in ectopically labeled interneurons that do not themselves express

Hb9 [Hinckley et al., 2005, Wilson et al., 2005]. The Hb9-lacZ mouse is a homologous recombinant such that β-galactosidase (LacZ) expression is confined only to Hb9-expressing neurons [Arber et al., 1999]. To confirm the identity of the true Hb9 interneurons, after photographing the GFP fluorescence, the whole spinal cord from Hb9-GFP/lacZ double transgenic mice was stained for LacZ activity. An iron buffer solution (in mM: 5 potassium ferricyanide crystalline, 5 potassium ferricyanide trihydrate, 2 magnesium chloride, in PBS) was prepared and stored in a light-protected container at 4 °C. A stock X-gal solution (20 mg/ml X-gal, in dimethylformamide) was prepared and stored at -20 °C. Both stock solutions were warmed to 37 °C prior to use. To make the staining solution, the stock X-gal solution was diluted 1:10 in the iron buffer solution (final X-gal concentration: 2 mg/mL) and sodium deoxycholate (0.01% by weight) and NP-40 Substitute (0.02% by weight) were added. The cord was covered with a lid to reduce evaporation and incubated in the staining solution overnight at room temperature to let the X-gal penetrate the whole spinal cord. Optimal staining occurred after 6 - 18 hrs. This staining resulted in cell-sized, blue precipitates that were clearly visible up to 200 μm below the ventral surface. We have tried other methods to stain LacZ-expressing cells in whole cord by pressure-injecting or incubating with fluorescent LacZ substrates (ImaGene Red or ImaGene Green, Invitrogen), or by replacing the iron buffer solution with nitroblue tetrazolium, all of which resulted in too much background staining. To correlate GFP and LacZ expression patterns, before X-gal staining we took a mosaic image of the GFP fluorescence, with depths in 10 μm increments and an overall width of at least 2 lumbar segments, using two-photon microscopy. Next, without moving the cord, the X-gal staining solution was added. Later, the X-gal reaction was imaged with a color CCD camera (CV-S3200, IAI, Israel) at different depths in the same lumbar regions. One-to-one correspondence of GFP and LacZ expressions could be determined

by comparing the mosaic projection images. Sometimes, cells would overlap in projection images and in those cases, the depth information was used to resolve the ambiguity.

Whole-cell recordings. Whole-cell recordings were made from spinal cords dissected as above. In some preparations, cells were exposed in a hemicord by cutting the entire cord along the midline as described by Hinckley et al [Hinckley et al., 2005]. Patch recordings were made with standard techniques as described by Zhong et al [Zhong et al., 2007]. Briefly, borosilicate glass pipettes with a tip resistance of 5-7 MΩ were filled with an internal solution containing (in mM): 138 K-gluconate, 10 HEPES, 5 ATP-Mg, 0.3 GTP-Li, and 0.0001 $CaCl_2$, pH 7.4 with KOH. Pipettes were visually guided to GFP+ cells identified by fluorescence illumination. A Multiclamp 700A amplifier and Clampex pClamp 9 software (Molecular Devices, Palo Alto, CA) were used. Fictive locomotion was evoked as in the imaging preparation. We attempted to identify the authentic Hb9 neurons in these recordings using the criteria suggested by Han et al. [Han et al., 2007]. However, as they also found, these criteria do not clearly fractionate the neurons into two groups, and we found that neurons that were identified as Hb9-like or non-Hb9-like had similar rhythmic properties. Thus, we present data on all the GFP-labeled interneurons.

Data analysis. Analysis of imaging data was performed with routines written in MATLAB (MathWorks). All fluorescence traces shown in the Figures are unfiltered raw traces. Fluorescence data from Bio-Rad-formatted images and electrophysiology recordings from Axon data files were imported as data arrays. Using the recorded TTL trigger signals from the Radiance control unit, time-lapse fluorescence data were interpolated and matched in time to the electrophysiological data. Cells were outlined manually based on their Fluo-3 and GFP fluorescence. The fluorescence of a cell, F(t), was the sum of all pixel values within the cell outline. The change in fluorescence,

$\Delta F/F_o$, was calculated as (F(t) - F_o)/F_o where F(t) is the fluorescence at time t, and Fo is the mean of baseline fluorescence from the first 10 imaging frames of the time-lapse series. For each cell, calcium signal peaks were identified by a routine that checks for rising fluorescence edges which increase in fluorescence by more than 3 standard deviations (SD) over the baseline fluorescence. This peak-picking routine can produce false positives, so edges that did not resemble a sharp rise followed by an exponential decay were manually deleted from analysis. In ≈5% of the data, we had to correct for lateral motion of the images in the *x*-*y* plane by thresholding the time-lapse fluorescence images into black-and-white frames and then finding the *x*-*y* shifts between consecutive frames that gave maximum cross-correlation. Motion correction for time-lapse images never exceeded ±5 pixels for *x*-*y* shifts, or the data set was discarded. None of the figures in this paper show motion-corrected fluorescence images or traces, although those data were included in calculating population statistics.

To analyze the temporal relationship between calcium activity and fictive locomotor activity recorded from the ventral roots, we used a double normalization procedure [Berkowitz & Stein, 1994, Zhong et al., 2007] to generate circular plots. Ventral root recordings were rectified and then smoothed with a time constant of 750 ms. The beginning of a fictive locomotor cycle, 0.0 on the circular plot, was defined as the moment when the ipsilateral ventral root activity became stronger than the contralateral ventral root activity. Similarly, the middle of a fictive locomotor cycle, 0.5 on the circular plot, was the moment when ipsilateral ventral root activity became weaker than the contralateral root activity. Using this double-normalized time scale, onsets of calcium peaks or action potentials from a single cell were plotted over the range from 0 to 1. An arrow represents the vector whose direction was the mean phase of spiking activity and whose length reflected the r-value: this is a measure of correlation between the timing of onsets of calcium peaks or action potentials, which indicates

whether the activity is significantly rhythmic and coordinated with the ventral root bursts [Kjaerulff & Kiehn, 1996, Zar, 1994].

Whole-cell recording results were analyzed using custom routines written in MATLAB (MathWorks, Cambridge, MA), Clampfit (Molecular Devices, Palo Alto, CA) and Spike2 (Cambridge Electronic Design, Cambridge, UK), as in Zhong et al. [Zhong et al., 2007]. Ventral root bursts were defined and the phase of each action potential calculated as in the imaging preparation.

Statistics. All statistical tests are taken from Zar [Zar, 1994]. We classified imaged cells as rhythmically active if they showed an n of at least six calcium peaks over four locomotor episodes, had $r>0.5$, and $p<0.05$ in the Rayleigh test using the approximation equation for p described by Zar [Zar, 1994]. All intracellularly recorded cells had an n of hundreds of action potentials, and the cells were classified as rhythmic if they had $r>0.5$, and $p<0.05$ in the Rayleigh test. Mean phase angles of many cells were averaged, and the resulting population mean angles were compared using the two-sample Hotelling test for whether the two population means are significantly different, with a confidence level of $p<0.05$. Errors for phase angles are expressed with 95% confidence limits calculated by Batchelets test for second-order mean angles. Statistical significance of some distributions was measured with a Wilcoxon signed-rank test. All errors are expressed as the standard error of the mean, unless otherwise specified.

4.3 Results

Hb9 interneurons can be positively identified in Hb9-GFP/LacZ double transgenic mice. Past studies of the role of Hb9 INs in the spinal locomotor network (e.g. [Hinckley et al., 2005, Wilson et al., 2005, Han et al., 2007]) used the

Hb9-GFP transgenic mouse line [Wichterle et al., 2002], in which the Hb9 promoter drives expression of green fluorescence protein (GFP). However, immunocytochemical co-labeling for Hb9 protein revealed that in this strain, GFP is expressed not only in Hb9 INs but also ectopically in other cells that do not express the Hb9 transcription factor [Hinckley et al., 2005, Wilson et al., 2005]. As a result, whole-cell recordings from a GFP-labeled cell may reflect activity of an Hb9 IN or an ectopically labeled cell that is genetically undefined. To distinguish between these two possibilities, numerous electrophysiological criteria for Hb9 IN have been suggested [Wilson et al., 2007a, Han et al., 2007, Ziskind-Conhaim & Hinckley, 2008, Brownstone & Wilson, 2008]. However, it is not clear which set of criteria is best or whether they can discriminate between the Hb9-expressing and ectopic populations of neurons [Han et al., 2007]. An alternate strategy for identifying Hb9 INs is to use an Hb9-lacZ transgenic mouse line where the knocked-in transgene produces LacZ. It has been demonstrated using Hb9 antibody staining that all of the LacZ-expressing cells are Hb9+ [Arber et al., 1999]. Therefore, by cross-breeding Hb9-GFP and Hb9-lacZ transgenic lines, it is possible to identify Hb9 INs via GFP fluorescence and subsequent LacZ stains. Indeed, this Hb9-LacZ approach works well in thin slices for immunohistochemistry [Wilson et al., 2005], although for electrophysiological whole-cell recordings, washout of the cytosolic LacZ into the pipette prevented identification in cells that were recorded for more than half an hour [Hinckley et al., 2005].

We have further pursued the GFP/LacZ strategy by staining for LacZ activity in whole spinal cords from Hb9-GFP/LacZ mice (Fig. 4.1A). Our optimized staining protocols, based on an overnight incubation with X-gal, resulted in round, cell-sized, blue precipitates across multiple thoracic and lumbar segments. The stained Hb9-expressing cells included the columns of motoneurons as well as clusters of Hb9 INs located in the ventromedial region of the T12-L2 segments. Cells located as deep as $\approx$200 μm

below the ventral surface were stained and imaged with a color CCD camera. By comparing image mosaics of the X-gal stain with the GFP fluorescence captured prior to LacZ staining (Fig. 4.1B, C), we can identify which GFP-expressing cells are also LacZ+ and therefore are true Hb9 INs (Fig. 4.1D, red circles). We found no correlation between cell size and identity. There were more Hb9 INs near the midline, but some ectopically labeled cells were in the same region. In one representative stain of 2 ipsilateral lumbar segments centered at L1 in a P2 Hb9-GFP/LacZ mouse, we found that 59% (40/68) of the GFP-labeled cells were Hb9 INs. This percentage is comparable to the numbers reported in two previous studies (≈55%, [Wilson et al., 2005]; 74%, [Hinckley et al., 2005]) and highlights the importance of avoiding the numerous ectopically labeled cells in Hb9-GFP mice.

Rhythmic calcium transients can be recorded from multiple Hb9 INs during fictive locomotion in the intact spinal cord. Earlier experiments studied putative Hb9 INs in slices or in hemisected spinal cords [Hinckley et al., 2005, Wilson et al., 2005] because the cells lie relatively deep beneath the ventral surface and cannot be visualized with wide-field fluorescent microscopy. Here, we used two-photon laser-scanning microscopy [Denk et al., 1990, Zipfel et al., 2003b, Wilson et al., 2007b] to image interneurons 50-200 μm deep within whole spinal cords (Fig. 4.2A). Multiple bolus injections of the membrane-permeant calcium-sensitive fluorescent dye Fluo-3 AM at sites along the midline in T13-L2 segments labeled hundreds of cells in the ventromedial region. Fluo-3 AM was chosen because a previous survey in our group found that this dye showed the most uniform labeling pattern and fluorescence responses with good signal-to-noise ratios [Wilson et al., 2007b]. Time-lapse images recorded calcium transients from the internalized AM-ester dye, which have previously been shown to reflect action potential activity with high accuracy [Kerr et al., 2005, Sato et al., 2007].

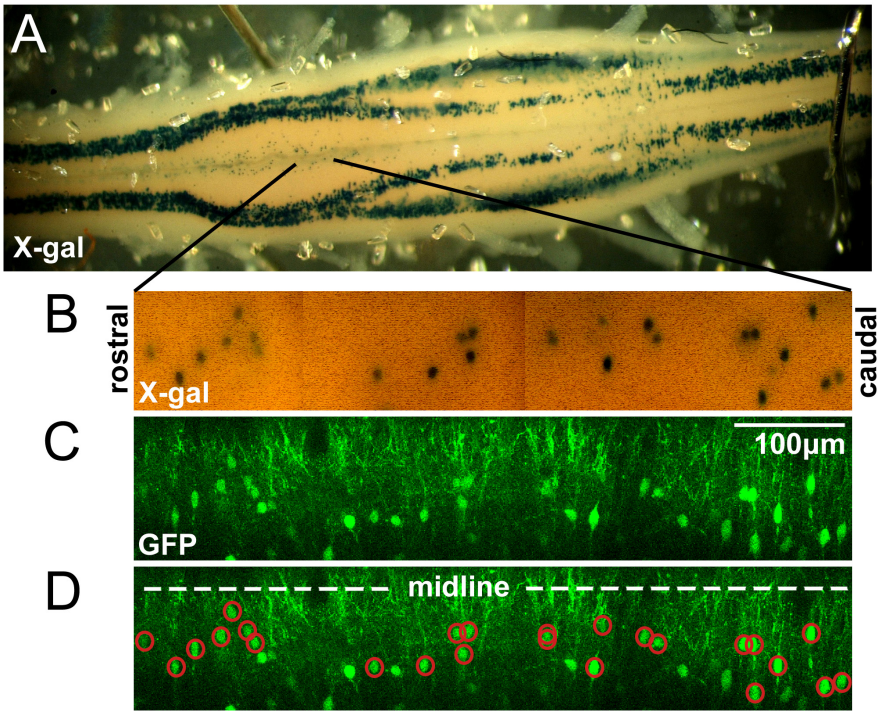

Figure 4.1: Identification of Hb9 interneurons. A, Spinal cord of an Hb9-GFP/lacZ mouse after an overnight X-gal stain. Hb9-expressing cells, including columns of motoneurons and small clusters of interneurons near the midline from T12 to L2, appeared as blue precipitates because they were LacZ+. The T13 to L2 ventromedial region had a slight orange tint due to the calcium-sensitive fluorescent dyes used for imaging experiments. B, Mosaic of projection images of the ventromedial region of a different spinal cord with X-gal-stained LacZ+ interneurons. Black lines indicate the approximate location in the spinal cord where these images were taken. C, The corresponding mosaic of projection images of GFP fluorescence taken with a two-photon microscope prior to X-gal stain. D, By comparing the spatial distribution of the X-gal and GFP fluorescence mosaics over multiple lumbar segments, we can identify post hoc GFP-labeled interneurons that were either Hb9 INs (GFP+/LacZ+, red circles) or ectopically labeled.

To verify this calcium peak-action potential correlation for spinal interneurons and also to determine the sensitivity of our microscope, we combined simultaneous whole-cell recording and calcium imaging on unidentified interneurons in the ventromedial region of the spinal cord (n=3 cells). The pipette was visualized with dextran-conjugated Cascade Blue, which also intracellularly labeled the interneuron (Fig. 4.2A). Because the calcium indicator dye washed out quickly, recordings were done within 5 minutes of break-in. In current-clamp, incremental current injection steps led to membrane potential depolarizations with increasing numbers of action potentials. Simultaneously we imaged the Fluo-3 fluorescence transients from the recorded interneuron (Fig. 4.2B). With a small amount of injected current, the interneuron depolarized but did not spike and showed no detectable fluorescence transient. With larger amounts of injected current, the interneuron fired one or more action potentials, which evoked a fluorescence peak whose amplitude correlated linearly with the number of action potentials (Fig 4.2C, linear fit R^2 = 0.79 to 0.91).

For our experiments, it was essential to determine the timing of the calcium peaks relative to the action potentials. The sampling rate of the laser scanning limits the temporal resolution at which we can measure calcium peaks. Because a barrage of action potentials during fictive locomotion can last for seconds, the fluorescence can continue to sum for many frames, and the time of the fluorescence peak may be considerably delayed relative to the start of firing. Thus, we chose to identify the frame before the fluorescence peak begins as the earliest time when a neuron could fire an action potential. As seen in Fig. 4.2D, each action potential is followed by a fluorescence peak (defined by $\Delta F/F_o > 3SD$ of F_o) in the next imaging frame. Preceding each significant fluorescence peak is a sharp rising edge whose lower point (Fig. 4.2D, red arrow) was used to estimate the earliest time when spiking activity could begin. This measured "onset of fluorescent peak" was measured for 103 current injection steps that resulted

in 1 to 7 action potentials; as expected, we found that the onset of fluorescent peak preceded the first electrophysiologically recorded action potential by 0.15±0.12 s (±SD) when imaging at 7 Hz, i.e. within one imaging frame. Together, these results demonstrate that the fluorescent peaks reflect suprathreshold activity and scale linearly with the number of action potentials. Moreover, the earliest possible time for beginning of interneuron spiking activity can be determined using the onset of rise in fluorescence with an accuracy of roughly the time to obtain one image frame (0.14 s).

We proceeded to investigate the activity of identified Hb9 INs in Hb9-GFP/lacZ mice. From the Fluo-3 AM-labeled cell population, we identified Hb9 INs by their GFP fluorescence and the subsequent X-gal stain (Fig. 4.3A, B). While imaging, fictive locomotion was elicited by one of two methods: 1) electrical stimulation of the caudal tip of the spinal cord [Gordon & Whelan, 2006, Zhong et al., 2007]; 2) chemical stimulation by bath application of 9 μM NMDA, 12 μM serotonin (5-HT), and 18 μM dopamine (DA). Both methods produced robust fictive locomotion with rhythmic ventral root bursting and left-right alternation, which was recorded using suction electrodes from upper lumbar ventral roots. Fig. 4.4C shows one representative set of calcium transients from a group of 4 GFP+ interneurons (3 of which were subsequently shown to be Hb9+, while one was Hb9-) during fictive locomotion. During fictive locomotion elicited by electrical simulation, the three Hb9 INs, but not the ectopically labeled cell, showed calcium peaks at the onset of fictive locomotion, as well as detectable peaks during later cycles of the locomotor episode. Fluorescence also slightly increases uniformly across many Fluo-3 AM-labeled cells at the beginning of electrical stimulation, with no peaks, as seen shortly after electrical stimulation in the ectopically labeled Hb9- cell 4 in Fig. 4.4C. During chemically-evoked fictive locomotion, the Hb9 INs had calcium peaks that were in phase with the ipsilateral ventral root activity, whereas the ectopically labeled cell was tonically firing. Bath application of NMDA/5-HT/DA caused a

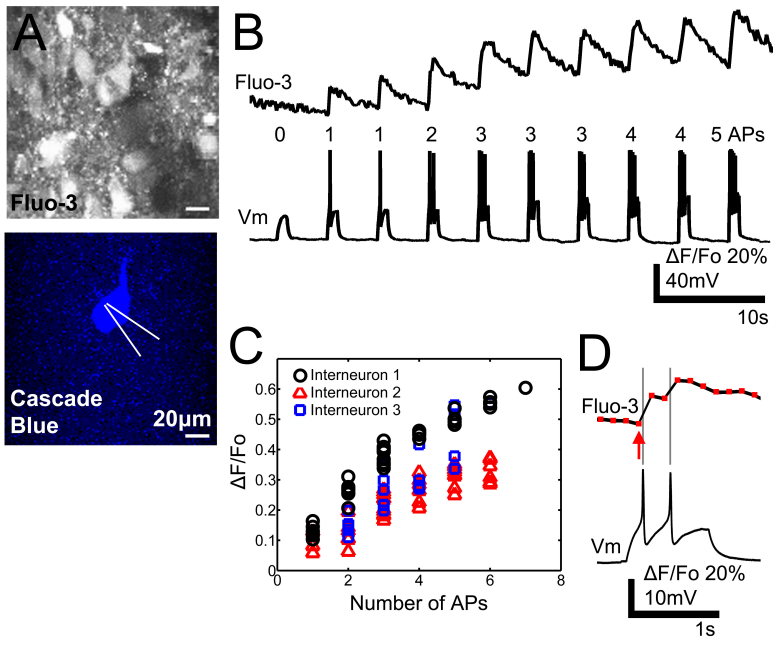

Figure 4.2: AM-ester calcium indicator dye accurately reflects the number and timing of spikes from spinal interneurons. A, Interneurons in the ventromedial region of intact neonatal mouse spinal cord were loaded with Fluo-3 AM. After hemisecting the spinal cord, whole-cell recording was made using pipette filled with dextran-conjugated Cascade Blue. B, Within 5 minutes of break-in, current injection steps elicited membrane potential depolarization and fluorescence transients. A small current step led to depolarization without action potential and no detectable fluorescence change, whereas larger steps resulted in spikes and fluorescence peaks, demonstrating that fluorescence reflects suprathreshold activity. C, The intensity of fluorescence peak scales linearly with the number of spikes evoked, although there were some variation among three interneurons from the same cord and dye preparation. D, Individual fluorescence data points (red rectangles) are shown with the corresponding electrical recording during one current step. Fluorescence transient peaks in the imaging frame following an action potential. The measured onset of fluorescence peak (red arrow) appears to occur prior to the start of the spiking activity due to our limited imaging frame rate.

19±5% increase of baseline fluorescence intensity in all Fluo-3 AM-labeled cells (n=12 cells, $p<0.01$, Student's t-test). This fluorescence increase applied to cells with or without GFP and reflected an overall increase in calcium concentration while the cord was excited by transmitters, which returned to the original baseline intensity following transmitter washout. These results demonstrated our ability to image calcium transients of multiple, identified Hb9 INs in a whole spinal cord during fictive locomotion.

Onset of Hb9 IN spiking activity occurs after the onset of ipsilateral ventral root activity at the beginning of a fictive locomotion episode. Transmitter-elicited fictive locomotion is well-characterized [Kjaerulff & Kiehn, 1996, Whelan et al., 2000] and provides a sustained period of fictive locomotion, but is not useful for studying the initial onset of a locomotor bout. In contrast, electrical stimulation of the caudal tip of the spinal cord evokes episodes of fictive locomotion, which can be repeated more than 20 times. Each episode consists of robust fictive locomotor patterns with rhythmic bursting and left-right alternation; it has a distinct initiation point, allowing us to study the events that occur at the beginning of a bout, during the transition from a resting state to fictive locomotion. To more closely investigate the possible role of Hb9 INs as the pacemaker kernel that drives the spinal locomotor circuit, we looked at the timing the initial onsets of Hb9 IN calcium peaks relative to ipsilateral ventral root activity. We found that at the start of fictive locomotor episodes elicited by electrical stimulation, onsets of Hb9 IN calcium peaks lagged behind the beginning of ipsilateral ventral root activity (Fig. 4.5A). The mean time lag for each Hb9 IN was calculated and the values for all Hb9 IN were summarized in a histogram (Fig. 4.5B). The mean lag was 1.42±0.33 s (n= 25 cells) and was significantly delayed compared to ipsilateral motor output ($p<0.001$). Some neurons failed to fire at all during the first ventral root burst (Fig. 4.5B). Of 25 neurons tested, only 3 had their average onset of calcium peak before the onset of the ipsilateral ventral root burst, and the mean onset was significantly later than the ventral

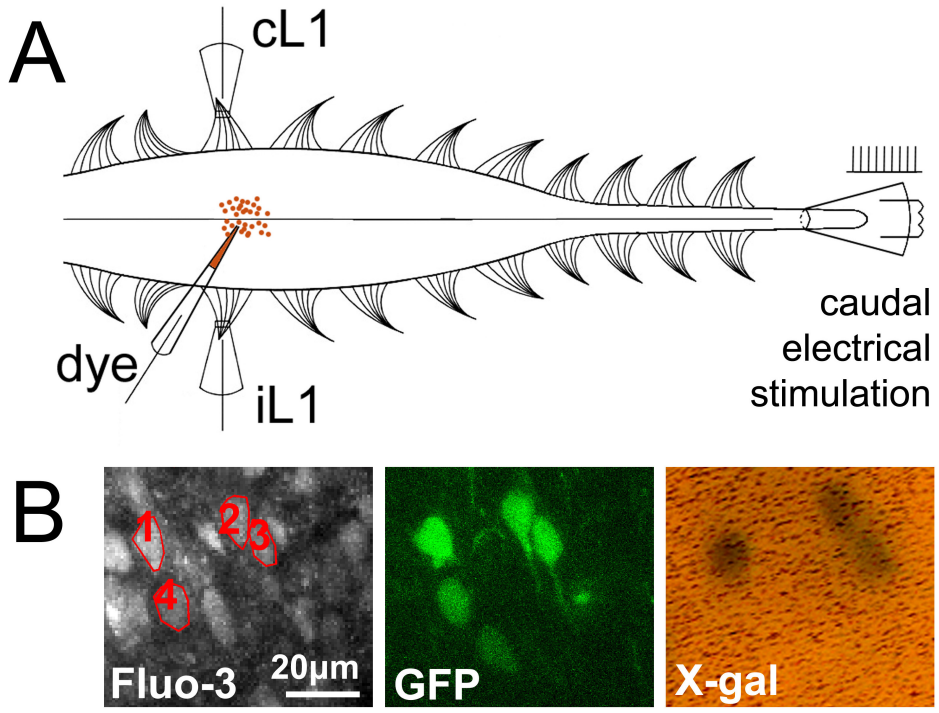

Figure 4.3: Two-photon calcium imaging of Hb9 interneurons during fictive locomotion (Part 1). A, Experimental setup. AM-ester calcium-sensitive fluorescent dyes were pressure-injected into the ventromedial region of an in vitro spinal cord from a neonatal Hb9-GFP/lacZ mouse. Suction recording electrodes were used to record extracellular electrical signals from ipsilateral and contralateral ventral roots (e.g. iL1 or iL2 and cL1 or cL2). Fictive locomotion was evoked by either bath application of NMDA, 5-HT, and DA, or electrical stimulation of the caudal tip of the cord. B, Two-photon projection images show cells near the injection sites that were indiscriminately loaded with Fluo-3 AM, and several cells that were expressing GFP. The GFP-labeled interneurons were subsequently identified to be either Hb9 INs or ectopically labeled by the post hoc X-gal stain.

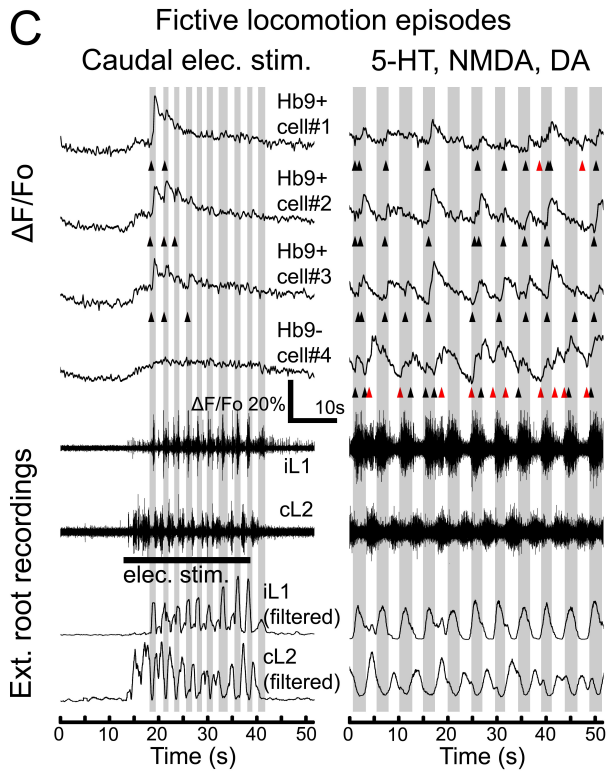

Figure 4.4: Two-photon calcium imaging of Hb9 interneurons during fictive locomotion (Part 2). C, Typical fluorescent traces show calcium transients in individual GFP-labeled interneurons during fictive locomotion. Electrical stimulation of the caudal tip of the cord elicited fictive locomotor episodes lasting ≈30 s. Extracelluar recordings of ventral roots and their corresponding low-pass filtered traces showed the signature left-right alternation of fictive locomotion. Hb9 INs, cells 1 to 3, had calcium peaks when ipsilateral ventral root is active (shaded gray) whereas the ectopically labeled cell, cell 4, was silent. Onsets of calcium peaks are indicated (triangles; black if in phase with ipsilateral root activity, red if out of phase). For the same set of cells, calcium transients were also imaged during fictive locomotion evoked by 9 mM NMDA, 12 mM 5-HT, and 18 mM DA. In chemically-induced fictive locomotion, Hb9 INs fired in phase with ipsilateral ventral root activity whereas ectopically labeled cell fired tonically in both ipsilateral and contralateral phases of fictive locomotion.

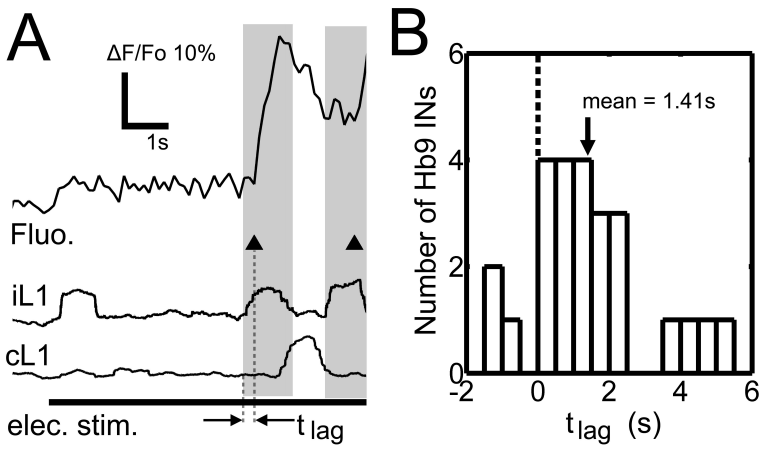

Figure 4.5: Onset of Hb9 interneuron calcium peak lags the onset of ipsilateral motor output (Part 1). A, Fluorescence trace shows the calcium transient of an Hb9 IN (GFP+/LacZ+) at the beginning of a fictive locomotor episode elicited by tonic electrical stimulation of the cauda equina. Fictive locomotion followed seconds after electrical stimulation began. Onset of calcium peak clearly lagged the beginning of ipsilateral ventral root activity. B, The lag time between onset of calcium peak and ipsilateral ventral root activity was averaged over multiple fictive locomotor episodes for each Hb9 IN. The distribution of the mean lag times are summarized in a histogram.

root burst onset ($p=6 \times 10^{-5}$, Wilcoxon signed-rank test). These data suggest that Hb9 INs are rarely active before or at the onset of ventral root activity; rather, most become active well after the onset of motoneuron bursting.

Rhythmic activity and timing of Hb9 INs during ongoing bouts of fictive locomotion. To evaluate the rhythmicity of Hb9 INs during ongoing fictive locomotion, we used circular statistics. Circular plots show the relative phase between the onset of the Hb9 IN calcium peak and the onset of ipsilateral motor output. In Fig. 4.6C, the onsets of calcium peaks for a single Hb9 IN during electrically and chemically-evoked fictive locomotion are shown. The mean phase is plotted as a vector, where the vector length

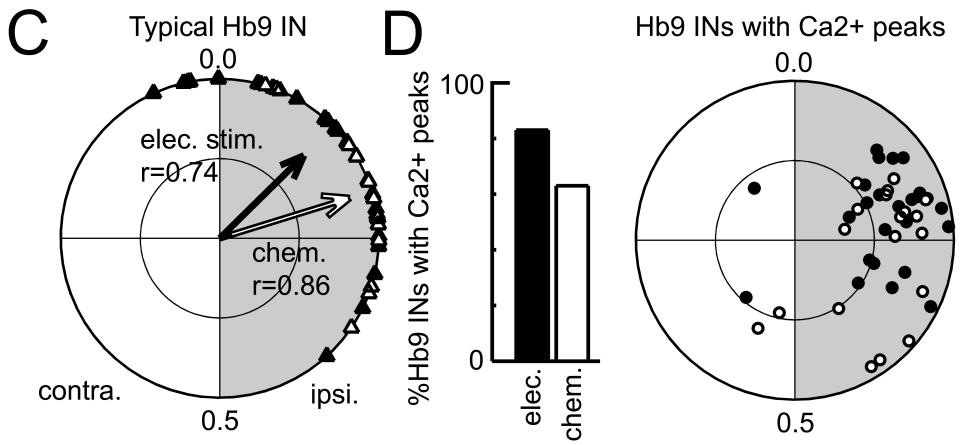

Figure 4.6: Onset of Hb9 interneuron calcium peak lags the onset of ipsilateral motor output (Part 2). C, Circular plot shows the onsets of calcium peaks (triangles; black for electrical stimulation, white for chemical) from one Hb9 IN relative to the locomotor cycle (ipsilateral half-cycle shaded gray). Most calcium peak onsets lie in the first quadrant of the circular plot, indicating that they lagged behind the beginning of ipsilateral motor output (labeled 0.0). Vector shows the mean phase and r-value, which is statistically significant and indicates that this Hb9 IN was rhythmically active. The inner circle indicates r = 0.5, the threshold for rhythmicity. D, Most of the Hb9 INs responded with at least one calcium peak during electrically and/or chemically-evoked fictive locomotion episodes. Population circular plot summarizes the phase of spiking activity from many Hb9 INs. Each dot represents the end of a mean phase vector from a single Hb9 IN, i.e. from a single-cell plot such as C (black for electrical stimulation, white for chemical).

reflects the r value, indicating the statistical significance of the rhythmicity. This neuron was significantly rhythmic during both types of stimulation with a mean onset phase in the first quadrant, 89% of the onsets of calcium peaks in the first and second quadrants of the plot, and only 11% in the fourth quadrant where they would be leading the ventral root burst. As a population, 83% (25/30) of the imaged Hb9 INs responded with multiple calcium peaks during electrically-evoked fictive locomotion episodes and 63% (19/30) during chemical stimulation. The onset phase of their activity is summarized in a population phase plot (Fig. 4.6D), where the vector of 80% of these responsive Hb9 INs lie outside the r=0.5 inner circle and thus they are rhythmically active. The mean phase of the significantly rhythmic Hb9 INs during fictive locomotion was 0.21 (r=0.58, 95% confidence intervals (CIs) of +0.03, -0.04) for electrical stimulation and 0.28 (r=0.52, 95% CIs of +0.08, -0.07) for chemical stimulation; both values are significantly later than 0, the onset of ipsilateral ventral root bursting (electrical stimulation: $p<4 \times 10^{-5}$; chemical stimulation: $p<0.01$; Wilcoxon test). The phase angles in the two conditions were not significantly different from on another ($0.1<p<0.25$, Hotelling test).

Because phase plots can be skewed by some Hb9 INs that responded with only a small number of calcium peaks, we further investigated the set of the most active Hb9 INs that responded with at least six calcium peaks over all fictive locomotor episodes during electrical (n=18) and chemical stimulations (n=15). Within this subset of cells, we found that 78% of Hb9 INs (14/18) were rhythmically active during electrical stimulation (average r=0.71) and 73% (11/15) during chemical stimulation (average r=0.66). For these rhythmic cells, the mean onset time vector was significantly greater than 0 for both electrical stimulation (0.19, CIs +0.04, -0.05, $p=6 \times 10^{-5}$, Wilcoxon test) and for chemical stimulation (0.24, CIs +0.17, -0.06, p=0.0005). All Hb9+ interneurons that were rhythmically active during chemically induced fictive locomotion were also rhythmically active during electrical stimulation, but some Hb9 INs that were rhyth-

mic during electrical stimulation were not rhythmic during chemically induced fictive locomotion. However, calcium imaging might have underestimated the number of interneurons with calcium peaks during chemical stimulation because the fluorescence changes during chemical stimulation tended to have smaller signal-to-noise ratios, possibly due to additional tonic activity in the presence of excitatory transmitters. Our data suggest that most Hb9 INs showed rhythmic and precisely timed calcium peaks during both electrically and chemically-evoked fictive locomotion, but the onsets of the calcium peak activity consistently lagged the onsets of ipsilateral ventral root.

Electrophysiological recordings confirm that Hb9 IN onset activity lags ventral root activity. Having demonstrated that the onset of Hb9 IN activity lags behind the onset of ipsilateral ventral root activity using calcium imaging, we wanted to confirm these findings using intracellular recordings, which offer much finer temporal resolution. Whole-cell recordings were made from GFP+ interneurons in the whole and hemisected spinal cords of Hb9-GFP mice. Intracellular recording of GFP+ cells in whole spinal cord is difficult because Hb9+ interneurons lie relatively deep beneath the ventral surface and are thus impossible to visualize with standard fluorescence microscopes. Our initial attempts to expose the neurons with slits in the ventral surface showed that damage to the ventral surface near the midline can very significantly reduced the likelihood of eliciting fictive locomotion via electrical stimulation of the caudal tip of the cord. We addressed this problem in two ways. First, we made intracellular recordings from superficial GFP+ cells in whole spinal cords. Fig. 4.7A shows a successful whole-cell recording of a GFP+ interneuron in the whole cord. This neuron showed subthreshold oscillations and rhythmic spiking activity during a fictive locomotor bout elicited by electrical stimulation (Fig. 4.7B) but mostly tonic activity during chemical stimulation, even when the neuron was hyperpolarized (Fig. 4.7C). A circular plot of all action potentials (Fig. 4.7D) showed that the mean firing phases for this cell were 0.32

(r=0.61) during electrical stimulation-evoked fictive locomotion. It is interesting that this cell was rhythmic during electrically-evoked but not chemically-evoked fictive locomotion. The lack of chemically evoked rhythmicity was not due to deterioration of the cell or the cord, as rhythmic bursting in response to electrical stimulation was observed before and after neurotransmitter application. We have also seen, in the imaging preparation, several cells that respond during one form of fictive locomotion but not the other. These anecdotal observations raise the intriguing possibility that depending on how it is evoked, fictive locomotion recruits different populations of interneurons for the CPG.

To record intracellularly from more neurons, we adopted the hemisected spinal cord preparation (Fig. 4.8E; [Hinckley et al., 2005]) that provided better access through the completely transected midline surface, but in which electrically-evoked fictive locomotion was not possible. Extracellular recordings of one ventral root showed slow that rhythmic bursting activity, which could be elicited by chemical stimulation. Whole-cell recordings of GFP+ interneurons revealed rhythmic spiking activity (Fig. 4.8F). Most cells were highly depolarized and fired almost continuously in the presence of NMDA/5-HT/DA, but when a holding current was applied to lower the membrane potential towards its natural level, visible bursts appeared in many of the cells, as previously reported by Hinckley and colleagues [Hinckley et al., 2005]. The circular plot of one typical GFP+ IN (Fig. 4.8G) confirmed that its rhythmic onset of spiking lagged the onset of ipsilateral ventral root activity, with a mean phase of 0.18 and a mean vector value of r=0.82. As a population, 53% of the GFP+ interneurons (9/17, Fig. 4.8H) tested were rhythmically active with $r > 0.5$. For these rhythmic GFP+ INs (average r=0.57), if all action potentials were counted, the mean phase of firing was 0.17 (95% CIs of +0.7, -0.11), Fig. 4.8I). To make a comparison with the calcium imaging experiments which measured the onset of spiking activity, we also plotted the timing of the first ac-

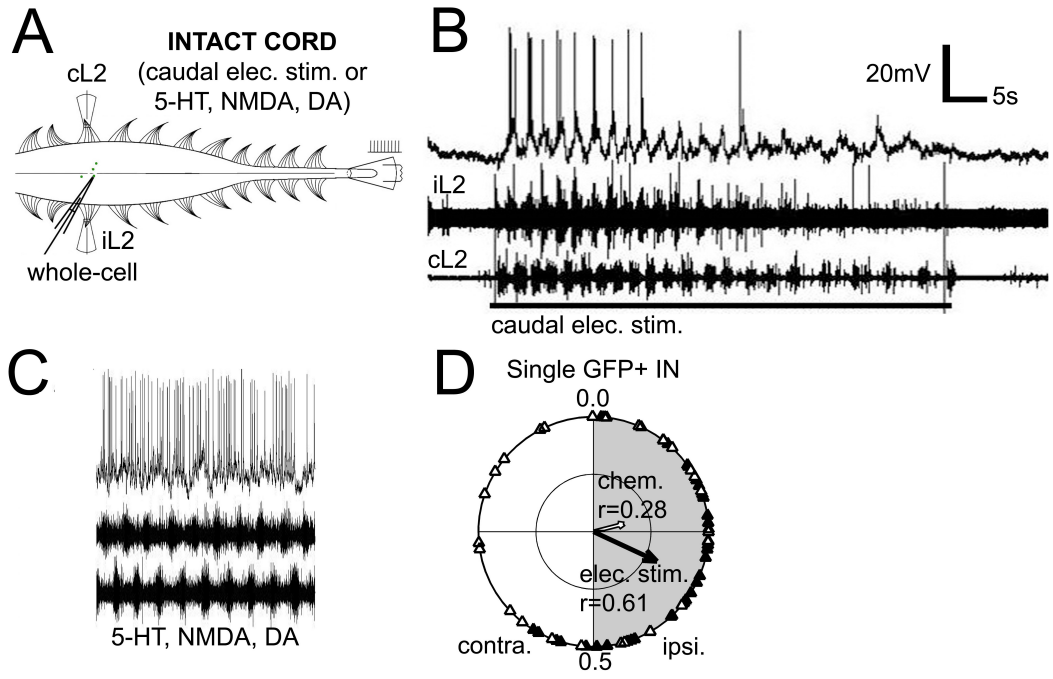

Figure 4.7: Intracellular recordings in whole and hemisected spinal cords confirm that spiking activity lags ipsilateral motor output (Part 1). A, Experimental setup for intracellular recording of GFP+ interneurons in the spinal cord of a neonatal Hb9-GFP mouse. B-C, Representative intracellular recordings from one putative Hb9 IN during fictive locomotion elicited by electrical or chemical stimulation. D, A circular plot shows that spikes from this GFP+ interneuron were mostly in-phase with the ipsilateral motor output during electrical stimulation (shaded gray, black triangles), although spikes during chemical stimulation were not rhythmic (white triangles).

tion potential per ipsilateral ventral root burst. Consistent with our imaging results, the mean phase of firing was 0.12 (r = 0.64, 95% CIs of +0.07, -0.09) and was significantly later than zero (Wilcoxon test p=0.001, Fig. 4.8J). Only one out of nine rhythmic GFP+ INs had a mean onset of spiking before the onset of the ipsilateral ventral root burst. The mean onset phases recorded either electrophysiologically (in the hemisected spinal cord; 0.12, Fig. 4.8J) or by calcium imaging (0.28, Fig. 4.6D), were not significantly

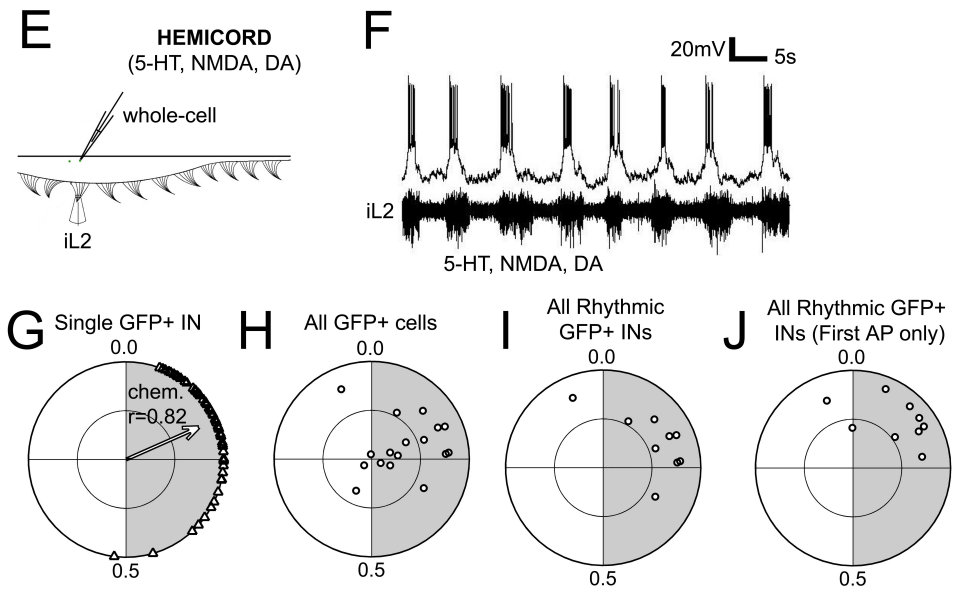

Figure 4.8: Intracellular recordings in whole and hemisected spinal cords confirm that spiking activity lags ipsilateral motor output (Part 2). E, Experimental setup for intracellular recording of GFP+ interneurons in a hemisected spinal cord of a neonatal Hb9-GFP mouse. F, Representative recording from one putative Hb9+ interneuron during chemically-evoked fictive locomotion. A bias current was applied to counteract the generally excitatory effect of the transmitters and display the bursts more clearly. G, A circular plot shows that spikes from this one GFP+ interneuron were mostly in-phase with the ipsilateral motor output during chemical stimulation (shaded gray, white triangles). H, Population circular plot of all GFP+ cells recorded show that about half of the GFP+ cells were rhythmic, i.e. outside the r = 0.5 circle. I, The rhythmic GFP+ INs have mean phases of spiking activity that lags the ipsilateral root activity. J. To compare with calcium imaging data, the population circular plot is re-graphed using only the first spike per burst (instead of all spikes). The mean phases still significantly lags the ipsilateral root activity.

different ($0.1<p<0.25$, Hotelling test) and were both were significantly later than zero. These electrophysiological data corroborate our imaging results to demonstrate that the onset of rhythmic firing by Hb9+ interneurons lags behind the onset of ipsilateral ventral root activity during fictive locomotion.

Activity patterns of Hb9+ interneurons are sparse and variable. Because there are relatively few Hb9 INs (≈100 to 500, 40 per lumbar segment near L1, Fig. 4.1), if they are to drive the rest of the CPG as the primary pacemaker neurons, they should show relatively robust and consistent levels of activity during each cycle of fictive locomotion. Electrical stimulation of the caudal spinal cord makes it possible to repeatedly induce episodes of fictive locomotion and see whether Hb9 IN activity is the same or different with each locomotor bout. During repeated episodes of fictive locomotion elicited by electrical stimulation, we imaged calcium transients of single Hb9 INs (Fig. 4.9A, B) and found each Hb9 IN's activity was variable on a cycle-by-cycle basis. In each episode, there were fewer calcium peaks than ipsilateral ventral root bursts, so the Hb9 INs did not fire during every locomotor cycle. Moreover, most calcium peaks occurred during the beginning of a fictive locomotor episode, with the probability of observing a calcium peak falling nearly to zero during a prolonged bout (Fig. 4.9C). In contrast, ventral root activity, quantified by the integrated area of each ventral root burst, remained stable and strong throughout a fictive locomotor episode (bottom trace, Fig. 4.9C). We also failed to find regular calcium peaks from a single Hb9 IN during each cycle of chemically-evoked fictive locomotion (Fig. 4.10D). As described above, most Hb9 INs showed rhythmic activity relative to the ventral root discharges, but were only active in ≈67% of the cycles. These data imply that Hb9 IN activity is not required for every ventral root burst and moreover, Hb9 IN may be more involved with the initiation than in the maintenance of an electrically-evoked fictive locomotor episode.

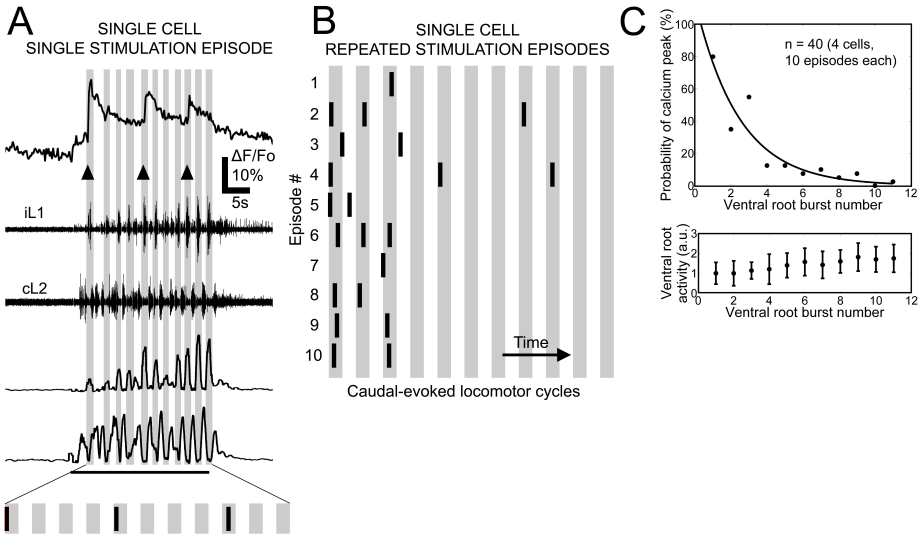

Figure 4.9: Firing patterns of Hb9 interneurons during a bout of fictive locomotion (Part 1). A, Representative fluorescence trace of calcium transient from one Hb9 IN (GFP+/LacZ+) during fictive locomotion elicited by electrical stimulation of the caudal spinal cord. Shaded area represents when ipsilateral ventral root is active and bar represents onset of calcium peak. This is shown schematically at the bottom of the trace. B, Calcium transients of one Hb9 IN during fictive locomotor episodes elicited by electrical stimulations that were repeated 10 times. Patterns of calcium peaks did not repeat and were sparse compared to the number of locomotor cycles. The Hb9 INs tended to show activity at the beginning of a fictive locomotor episode and fall off sharply with repeated bursts during a bout. These data are quantified in C, showing the probability of the neuron delivering a calcium transient for each burst in the bout (data averaged from 40 bouts). By comparison, the integrated areas of ipsilateral and contralateral ventral root activity were relatively stable throughout the bout (bottom graph in C).

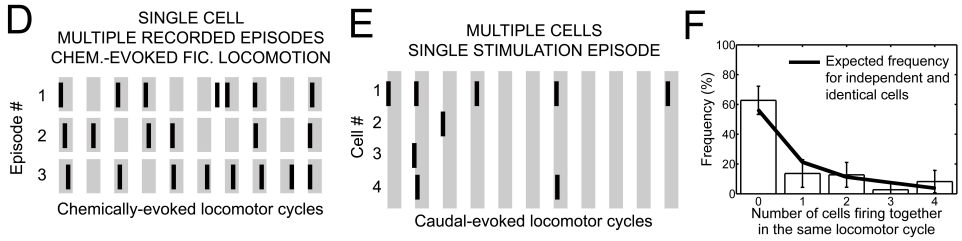

Figure 4.10: Firing patterns of Hb9 interneurons during a bout of fictive locomotion (Part 2). D, Calcium transients of a single Hb9+ interneuron during fictive locomotion elicited by bath application of 5-HT, NMDA, and DA; the three lines show consecutive records of activity during 30 locomotor cycles. Calcium peaks were observed in most but not all the locomotor cycles. E, During electrically-evoked fictive locomotion, four nearby Hb9 INs show uncoordinated calcium transients. F, The frequencies of observing the 4 cells in E firing together in the same cycle are quantified, based on 10 bouts. A trend line shows the expected frequencies for four cells if they are independent, identical, and generate calcium peaks with probability as shown in Fig. 4.9C. Similarity between the trend line and the observed frequency suggest that Hb9 INs were not strongly coupled.

Calcium imaging enabled us to record calcium transients from multiple Hb9 INs at once. When comparing as many as 5 Hb9 INs within the same field of view, we did not observe any obvious spatial organization in their activation patterns. Within a single electrically-evoked fictive locomotion episode, activity of Hb9 INs from cycle to cycle appeared uncoordinated (Fig. 4.10E). We quantified the frequencies of observing multiple Hb9 INs firing together during the same cycle (Fig. 4.10F), and compared these to the predicted frequencies assuming that each Hb9 IN was independent and showed activity according to the calcium peak probability in Fig. 4.9C. There was no significant difference between the expected frequencies and the observed frequencies, suggesting that these Hb9 INs were not strongly coupled and fired independently during fictive locomotion.

Hb9 interneurons are rhythmically active only at concentrations of NMDA, 5-HT and DA that evoke fictive locomotion. To further test if the rhythmic calcium peaks observed in Hb9 INs are related to fictive locomotion, we imaged multiple Hb9 INs while increasing the concentrations of transmitters (Fig. 4.11). In normal ringer, Hb9 INs and the ventral roots were silent. Spontaneous calcium peaks in Hb9 INs were sparse, occurring at a rate of 0.48±0.22 per minute (n=5). At our standard concentration of 9 μM NMDA, 12 μM 5-HT and 18 μM DA, fictive locomotion was elicited as demonstrated by the rhythmic, alternating bursting activity recorded in the ventral roots; rhythmic calcium transients were also observed in Hb9 INs. At higher concentrations of 5-HT, NMDA, and DA, fictive locomotion ceased but the ventral roots showed more tonic activity than the baseline, as shown by the raw and low-pass-filtered traces of ventral root recordings. As the rhythmic motor pattern ceased, rhythmic calcium transients in Hb9 INs also vanished. This result could arise from depolarization block of spike generation due to the high concentration of NMDA; however, calcium peaks could still be observed in unidentified cells and in ectopically labeled cells (Hb9-, LacZ-/GFP+, see Fig. 4.13), demonstrating that at least some cells in the cord were not in a state of depolarization block. These data showed that Hb9 INs only have rhythmic calcium transients when the transmitter concentrations are suitable for eliciting fictive locomotion. This observation support our other data showing that the rhythmic calcium accumulation of Hb9 INs is related to fictive locomotion.

Heterogeneous firing activity of ectopically labeled interneurons. So far we have focused on the genetically-defined population of Hb9 INs. Since our X-gal stain also identifies ectopically labeled (Hb9-, GFP+/LacZ-) cells, we looked at their patterns of calcium activity during fictive locomotion. Ectopically labeled cells typically showed two kinds of calcium transients (Fig. 4.12A). About half of the cells (14/27, 52%) remained silent during fictive locomotion evoked by either method (Fig. 4.12A, right).

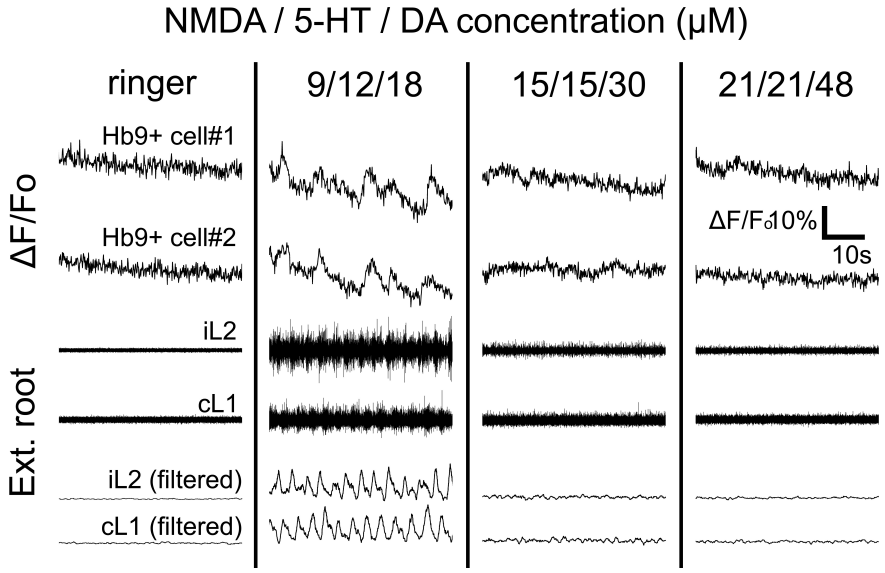

Figure 4.11: Hb9 interneurons were rhythmically active at transmitter concentrations suitable for evoking fictive locomotion. Fluorescent traces show calcium transients of two Hb9 INs (GFP+/LacZ+) during bath application of increasing concentrations of NMDA, 5-HT, and DA. In normal ringer, the Hb9 INs and ventral roots were silent. At transmitter concentrations of 9 μM / 12 μM / 18 μM, fictive locomotion was elicited as confirmed by left-right alternation of rhythmic bursts in ventral root recordings. Rhythmic calcium transients were also seen in the two Hb9 INs. At higher concentrations, fictive locomotion ceased and the ventral roots fired tonically whereas the Hb9 INs' rhythmically bursting calcium transients also disappeared. This set of data suggests that the rhythmic activity in Hb9 INs was fictive locomotion-related.

The other half of the ectopically labeled cells (13/27, 48%) had calcium transients during chemical and/or electrical stimulation. Among all the ectopically labeled cells, 30% (8/27) had calcium peaks with a distinct "sawtooth" shape including a large, sharp peak (Fig. 4.12A, left). Although the frequency of sawtooth-like calcium peaks was roughly the same as the fictive locomotion stepping cycle, the onsets of sawtooth-like calcium peaks were not significantly phase-locked relative to the ipsilateral ventral root bursts during chemically-elicited fictive locomotion (Fig. 4.13B). Moreover, the frequency of these sawtooth-like calcium peaks increased in higher transmitter concentrations at which fictive locomotion had ceased (Fig. 4.13C); note that the two ectopically labeled cells recorded simultaneously were not coordinated in their firing. As a population, few ectopically labeled cells were rhythmic during chemically stimulated (3/27) or electrically stimulated fictive locomotion (6/27, Fig. 4.13D), and the onset times of these few rhythmically active cells were typically in the first quadrant, after onset of ipsilateral ventral root activity. These results show that ectopically labeled cells (GFP+/LacZ-) have heterogeneous activity patterns; a minority are rhythmically active in phase with fictive locomotion, while the majority are silent or show rhythmic activity that is unrelated to fictive locomotion.

4.4 Discussion

Our study used two-photon calcium imaging and whole-cell recording to investigate the timing of spiking activity of Hb9 interneurons during two types of fictive locomotion in intact neonatal mouse spinal cords. Our data suggest that Hb9 interneurons are likely to be a part of the spinal locomotor CPG, but because their onset of spiking activity lags behind that of the ipsilateral ventral root activity, Hb9 interneurons are not likely to provide the major intrasegmental rhythmic drive for the motor pattern.

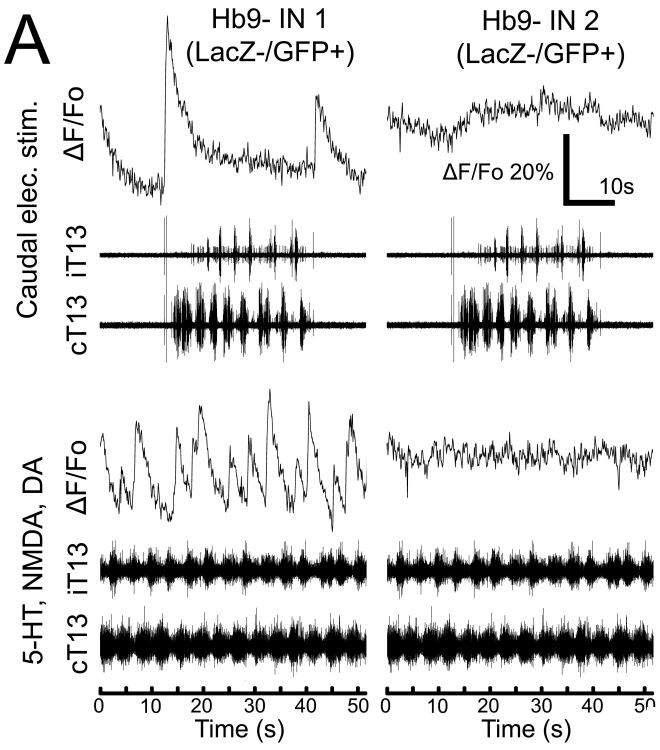

Figure 4.12: Heterogeneous types of calcium transients observed in ectopically labeled (Hb9-, GFP+/LacZ-) cells (Part 1). A, Representative fluorescence traces of calcium transients seen in two types of ectopically labeled cells. About half of the ectopically labeled cell showed large sawtooth-like calcium peaks during fictive locomotion, especially during fictive locomotion evoked by bath application of transmitters. The remaining half of the ectopically labeled cells were silent in all conditions tested.

Possible role of Hb9 INs in rhythm generation in the mouse locomotor CPG. The organization of the CPG for mammalian locomotion remains poorly understood. McCrea and colleagues [Lafreniere-Roula & McCrea, 2005, Rybak et al., 2006a, Rybak et al., 2006b, McCrea & Rybak, 2008] have used analysis of spontaneous motor deletions during locomotion to argue for a two-layer model of the CPG, wherein a kernel of neurons form the rhythm-generating network which in turn drives interneurons in a pattern-generating network to organize locomotion. The structure of such a

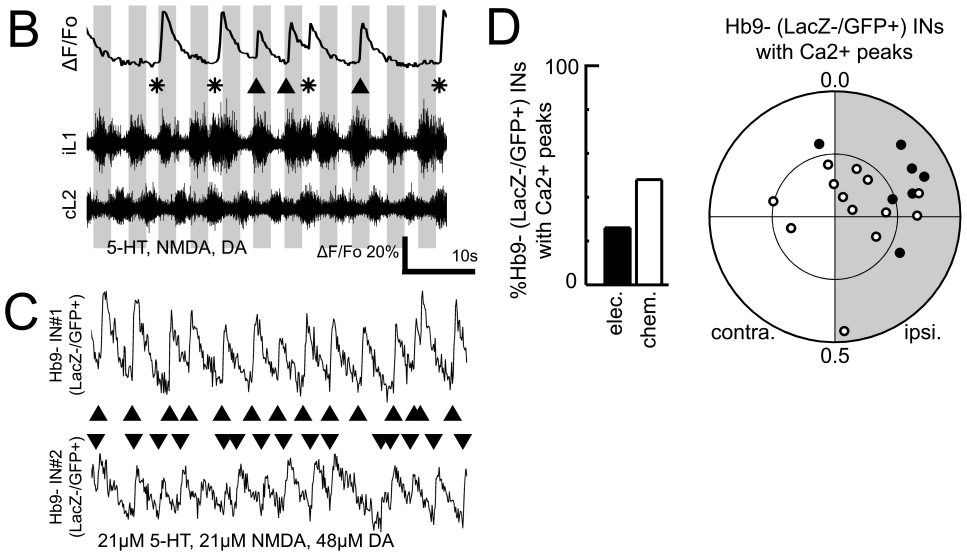

Figure 4.13: Heterogeneous types of calcium transients observed in ectopically labeled (Hb9-, GFP+/LacZ-) cells (Part 2). B, Magnified view shows that the sawtooth-like calcium peak onsets were not rhythmically coordinated to the phases of fictive locomotion (triangles if in phase with ipsilateral root activity, asterisks if out of phase). C, At higher transmitter concentrations, the frequency of occurrences of sawtooth-like calcium peak increased. Two ectopically labeled cells within the same imaging field-of-view showed calcium transients with distinctly different onset timing. D, Most ectopically labeled cells did not respond to electrical and/or chemical stimulations with calcium peaks. Population circular plot displaying only the responsive cells shows that most of them, including the ones exhibiting sawtooth-like calcium peaks, were not rhythmically active during chemical stimulation.

rhythm-generating kernel is completely unknown, but based on invertebrate networks, it could arise from a combination of network interactions and the intrinsic properties of the component neurons. These interactions could vary across a broad spectrum, from one extreme, where a set of non-oscillatory neurons generates a rhythm by mutual excitation and fatigue, to the other extreme where the neurons possess endogenous pacemaking oscillatory properties [Marder & Bucher, 2001, Feldman & Del Negro, 2006, Wilson & Brownstone, 2008]. Finding cell types in the spinal cord with properties appropriate for a role in one or the other model will provide evidence as to which model is correct.

The Hb9 INs have caused significant interest since their first electrophysiological characterizations in 2005 [Wilson et al., 2005, Hinckley et al., 2005]. These neurons are rhythmically active during transmitter-evoked fictive locomotion in the isolated hemicord [Hinckley et al., 2005], and also show TTX-resistant oscillations in the presence of the same transmitter cocktail [Wilson et al., 2005, Ziskind-Conhaim et al., 2008]. This raised the possibility that these neurons are endogenous oscillators that may play a central role in the rhythm-generating kernel of the CPG [Ziskind-Conhaim et al., 2008, Wilson & Brownstone, 2008]. More recent work has suggested that the Hb9 INs may not be intrinsically oscillatory: their TTX-resistant oscillations depend on electrical coupling, although it is not clear whether they are coupled to each other [Hinckley & Ziskind-Conhaim, 2006] or to other unidentified neurons [Wilson et al., 2007a].

In an insightful review, Brownstone and Wilson [Wilson & Brownstone, 2008] laid out a set of criteria that would define a neuron as a component of the rhythm-generating kernel of the spinal locomotor CPG. For example, they must be positioned ventromedially in the region where the CPG has been located by lesion and imaging studies;

they must receive appropriate sensory and descending synaptic inputs that can affect the rhythm; they must be excitatory and have properties (synaptic or intrinsic) that support rhythm generation. Finally, they must be rhythmically active during fictive locomotion, and future cellular knockout studies must show that they are necessary for the network to function. The Hb9 INs meet many of these predictions.

In addition, we propose three additional criteria which would characterize a class of interneurons that plays a central role in the CPG rhythm-generating kernel. First, since the rhythm-generating kernel drives the pattern-generating network and indirectly the motoneurons, members of the rhythm-generating network should start firing before the motoneurons at the onset of a bout of fictive locomotion, and their onset phase should lead that of the MNs during each burst of a locomotor bout. Second, the neurons should remain active throughout a bout of fictive locomotion, thus providing continuous drive for the rhythm. A third and weaker prediction is specific to the Hb9 INs: since there are so few of them in each spinal segment (≈ 40 per lumbar segment near L1, Fig. 4.1), each neuron should be active in every or nearly every cycle, in order to provide sufficient drive to the pattern-generating networks of the CPG.

We have tested these three criteria using calcium imaging and electrophysiological recordings. In the intact cord preparation, we can initiate repeated bouts of fictive locomotion by electrical stimulation of the caudal spinal cord, allowing us to carefully record the timing of onset of Hb9 activity relative to the ipsilateral ventral roots. We found that in the overwhelming majority of measurements, the first detectable rise of the Hb9 calcium peak lagged behind the onset of ipsilateral ventral root burst activity by an amount that could not be explained by the slow kinetics of calcium signal activation (Figs. 4.5, 4.6). Thus, initial activity in the Hb9 INs does not precede the first MN bursts, making it impossible for them to initiate MN activity. This alone does not dis-

qualify the Hb9 INs: it is possible that the unpatterned synaptic input from caudal cord stimulation excites many neurons, and the MNs simply start firing first. However, then we would expect that in subsequent cycles of the motor bout, the normal CPG network would take charge of rhythm generation, such that the Hb9 INs would begin to lead the MNs thus providing the rhythmic drive demanded of the rhythm-generating network. However, we found that this is not so. With electrically-evoked bouts of locomotor activity, the onset of Hb9 IN activity continued to lag behind the ipsilateral ventral root bursts throughout the bout. Both in the intact cord (with calcium imaging) and in the hemicord (with whole-cell recording), we found that during transmitter-evoked fictive locomotion, the Hb9 INs almost always started to fire later than the ipsilateral ventral roots. Thus, the timing of onset of Hb9 activity is not appropriate for them to provide the major intrasegmental rhythmic drive to initiate the next cycle of motoneuron activity.

The Hb9 INs also fail the second criterion, requiring continued activity during a locomotor episode. With electrically stimulated locomotor activity, we found that the Hb9 INs were most active during the first few cycles, but rapidly reduced their activity or fell silent, so that virtually none of them were active in the final cycles of the bout (Figs. 4.9, 4.10). Despite this, the strength and rhythmicity of the motoneuron bursts was not significantly decreased in the later cycles of a bout. It is hard to imagine a crucial component of the rhythm-generating kernel of the CPG acting in this way.

The third criterion is a weaker one; based on the relative paucity of Hb9 INs in the spinal cord, it seems reasonable that they should be active on each or nearly each cycle of the locomotor rhythm, to provide sufficient drive to the pattern-forming network. Again, this is not seen, either during electrically-evoked fictive locomotion, where the Hb9 INs rapidly decrease their activity, or during transmitter-evoked fictive locomotion, where an Hb9 IN on average only fires a calcium peak on $\approx$67% of the cycles. It is possible

that only a small minority of Hb9 INs need be active at any time, but if so, they would have to evoke very strong synaptic drive to their follower cells.

While these new criteria appear to rule out a role for the Hb9 INs as the major intrasegmental pacemaking neurons in the rhythm-generating kernel of the CPG, they might still contribute to the rhythm-generating component of the CPG. For example, the Hb9 INs might not be providing drive to the pattern-forming networks within the same segment, but instead, they may drive networks in a more caudal segment whose motoneurons would be active with some phase delay [Bonnot et al., 2002], such that the Hb9 INs could indeed lead the follower neurons. Second, the Hb9 INs might still participate in rhythm generation as part of a distributed network of mutually exciting interneurons. After another phase-leading interneuron initiated the next motor burst, the Hb9 INs could be "holding" timing information before handing the excitation off to another class of cells, before the excitation finally returns to the phase-leading cells.

Even if they are not part of the rhythm-generating network, their significantly rhythmic activity with a highly uniform phase during fictive locomotion suggests that the Hb9 INs are active components of the locomotor CPG. They may act as amplifiers: once the MNs begin a burst, Hb9 cells active in the first half of the burst could further excite the MNs and help push the burst to its peak intensity. Alternatively, the observation that Hb9 INs are more likely to be active early than late in a bout of electrically-evoked locomotion suggests they may have some function in establishing a bout of locomotion rather than sustaining it. Of course, their uniform phase may reflect Hb9 INs being electrically coupled to, or receiving simultaneous inputs from, a group of presynaptic partners involved in locomotion, without Hb9 INs being required for locomotion at all. The field eagerly awaits a method of silencing Hb9 IN activity without affecting MN activity, so the necessity of Hb9 INs for fictive locomotion can be directly tested.

CHAPTER 5

WHAT CAN POPULATION CALCIUM IMAGING TELL US ABOUT NEURAL CIRCUITS?*

Calcium imaging of bulk-loaded fluorescent indicators can be used to record the spiking activity of hundreds of neurons. Recent advances promise imaging technologies that are faster, more efficient, and applicable to awake animals, thereby moving imaging capabilities closer to the traditional strengths of multi-electrode arrays. This article reviews these technical achievements and discusses how they can help us achieve the goal of understanding neural circuits.

5.1 Introduction

Activity in a single neuron results from the flow of charged ions and is inherently electrical by nature. Electrophysiology, the measurement of these electrical currents, provides great insights to neural systems. In simpler neural circuits such as the stomatogastric ganglion in crustaceans, multiple intracellular electrodes can be used to record membrane potentials from all of the identified component cells in the network. From these recordings, knowledge of the various synaptic connections, ionic currents, and activity patterns can then be combined to generate a basic understanding of the circuit operating principles. However, scaling this approach to more complex neural systems is limited by the number of recordings possible, as constrained by the patience of the experimenter and the available table space for micromanipulators.

One method to circumvent this limitation is multi-electrode arrays [Buzsáki, 2004], which use an array of closely spaced electrodes to record spiking activity from many

*Originally published as: Kwan, A.C. (2008) "What can population calcium imaging tell us about neural circuits?", J. Neurophysiol., 100, 2977-2980

neurons at once. When applied to animal models, multi-electrode arrays have been useful in obtaining insights about the firing patterns of neural circuits that underlie different types of behaviors. Recently, another technique, calcium imaging of tissues bulk-loaded with membrane-permeable fluorescent indicators [Stosiek et al., 2003], has emerged which also enables spiking activity to be recorded from multiple neurons. This technique was received with much excitement because imaging is compatible with other optical methods and can be used on transgenic animal models that express fluorescent markers. In the last year, significant progress [Dombeck et al., 2008, Duemani Reddy et al., 2008, Holekamp et al., 2008] has been made in improving the optical and experimental setup (Fig. 5.1), such that the capability of population calcium imaging is approaching some of the traditional strengths of multi-electrode arrays. Here, I will discuss these technical advances in the context of using population calcium imaging as a tool to understand neural circuits.

5.2 Discussion

Calcium imaging of neuronal populations. Currently, the most widely used method for population calcium imaging was introduced by Arthur Konnerth's laboratory [Stosiek et al., 2003]. In their approach, acetoxymethyl (AM)-ester calcium indicator dyes (popular choices are calcium green-1 AM and Oregon green 488-1 AM) are ejected into the tissue sample when an outward pressure is applied. The AM-ester dyes are membrane-permeable; they enter the cells and remain inside the cell after an intracellular esterase cleaves the ester. Using this bulk-labeling method, Stosiek et al. were able to stably label hundreds of cortical cells within a $\approx$400-μm-diameter region for many hours. Kerr et al. [Kerr et al., 2005] subsequently showed that fluorescence changes recorded from bulk-labeled neurons are direct results of calcium influx from action po-

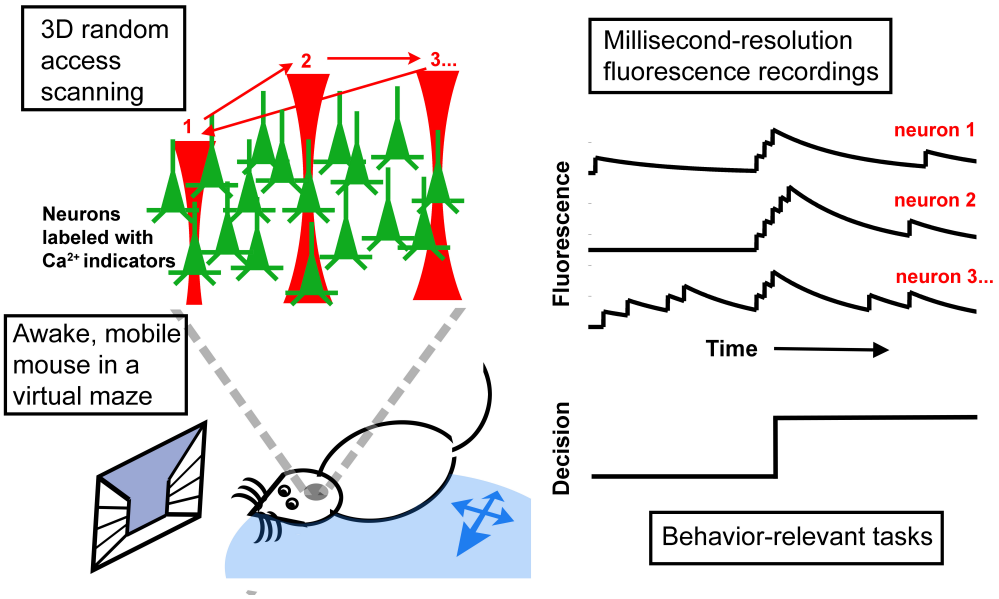

Figure 5.1: An ideal population calcium imaging experiment for studying neural circuits. This diagram illustrates a calcium imaging experiment made possible by recent advances: recording spiking activity from neuronal networks in an awake mouse with single-cell spatial and millisecond temporal resolutions. Left: two enabling technical advances. First, a 3-dimensional (3-D) random access method is used to steer the laser beam efficiently to points of interests. By eliminating the slow mechanical scanning mirrors, calcium imaging can now be done at selected locations with millisecond resolution. Second, a head-fixed, trained mouse is comfortable while its feet are grounded on a free-floating ball. When incorporated into a microscope, the "mouse-on-a-ball" setup permits imaging in awake, mobile mice with minimal movement artifacts. Data from such experiments (right) will provide insights for understanding neural circuits including ones that underlie decision-making tasks.

tentials. To demonstrate this tight relationship, they patched bulk-labeled pyramidal neurons in a cell-attached configuration and were able to show that 97% of single action potentials can be reliably detected by using fluorescence. With past studies in which calcium indicators have been introduced by other methods (e.g. whole-cell patching, bath incubation, etc.), this result confirms that fluorescence reports suprathreshold neuronal activity. Thus, with many labeled cells, stable fluorescence, and direct correlation with action potentials, population calcium imaging fulfills the basic requirements to be a useful technique for monitoring the spiking activity of neuronal populations.

Imaging of the bulk-labeled tissue is usually done with two-photon microscopy [Denk et al., 1990, Zipfel et al., 2003b]. Here, a femtosecond pulsed laser provides infrared photons which are focused onto the fluorescent sample. When two infrared photons are absorbed nearly simultaneously, their combined energy is enough to excite a fluorophore and produce a fluorescence photon. The uncertainty principle tells us that "nearly simultaneous" is <1 femtosecond, so two-photon absorption is a rare event except at the focus of the objective lens, where there are the most number of infrared photons. Knowing that the fluorescence must come from the focal volume is important, because then all detected fluorescence photons, scattered or not, can contribute to a useful signal. This is the key reason why in scattering tissues such as the brain, two-photon microscopy has been the de facto instrument of choice.

However, despite its unique capability for deep-tissue imaging, most two-photon microscopes are relatively slow and bulky. Attempts to create miniature two-photon microscopes have compromised on spatial resolution or field of view, which limits their practical utility for small animal studies. Furthermore, to generate an image, the laser beam is raster-scanned by a pair of mechanical galvanometers that typically oscillate at <2 kHz. Scanning in the z-direction is usually done by moving the microscope objective,

which is even slower. Imaging at this speed will miss the millisecond-scale events in the brain, for example the rising and falling of single action potentials.

Imaging from a new perspective. How can we scan faster while maintaining the deep-tissue advantage of two-photon microscopy? Duemani Reddy et al. [Duemani Reddy et al., 2008] offer an efficient solution for scanning a 3-D volume: send the laser beam only to the interesting regions, such as the soma or the dendrites, and waste no time on other regions. To implement this idea, they chose not to rely on mechanical galvanometers and motorized microscope objectives, which are slow because mirrors and objective lenses are relatively heavy. Instead, the laser beam is steered using acoustic-optical deflectors (AODs). Re-positioning can be fast ($\approx$10 μs, depending on size of AOD), allowing the beam to be moved to multiple spots quickly, and not necessarily in sequential order. An exciting development in this work is that by steering with a series of 4 AODs driven by custom waveforms, Duemani Reddy et al. are now able to randomly access spots in a 3-D volume, whereas previous implementations were limited to two dimensions.

The AOD method is tantalizing because although it may not be faster than galvanometers, it is more efficient. Scanning only the points of interest allows more pixel dwell time to collect fluorescence and improve signal-to-noise. To test their system, Duemani Reddy et al. imaged sub-micron fluorescent beads to measure the point spread function, a key parameter of spatial resolution for a microscope. While the resolution was not flattering ($\approx$0.5 $\times$ 2.3 μm at focus, which is $\approx$3 times the expected size in an optimal two-photon microscope, see [Zipfel et al., 2003b]), they found only slightly worse resolution when scanning the z-axis with AODs and were able to resolve dendritic spines. Fast functional imaging was demonstrated in acute brain slices. On a single calcium indicator-filled CA1 pyramidal neuron, they initially determined several dendritic

locations from an image stack of the neuron, then return to those points of interest to measure calcium transients. The current implementation has some remaining technical problems. For example, the z-range is only 50 μm and the pulse tends to broaden to picosecond duration. Both of these shortcomings can be improved with better or additional optical elements. The real question is whether the added optical complexity can be justified by the new capability; I believe the answer is a resounding yes, especially for certain applications such as uncaging or imaging membrane potentials.

To tackle the same problem on imaging speed, Holekamp et al. came up with a different solution [Holekamp et al., 2008]. They knew that wide-field illumination can excite dyes across the entire field of view, and fluorescence can be collected with a fast CCD detector. This is the most basic form of microscopy, but it is not suited to tissue imaging because it does not provide optical sections, so cells at different axial locations will overlap. To overcome this problem, Holekamp et al. separated the excitation and detection paths. For excitation, instead of a microscope objective, they used illumination optics that include a cylindrical lens to generate a light sheet that excites only a thin layer of cells. Fluorescence is then collected by an orthogonally placed CCD detector that is coupled in movement with the illumination optics. Finally, the microscope was set up at a 45° angle such that both excitation and detection paths enter from the same surface, enabling the system to be used for preparations such as cranial windows.

This method, termed objective-coupled planar illumination microscopy, provides optical sections with a specific thickness contingent on the light sheet, which is $\approx$5 μm thick. For population calcium imaging, this thickness matches with the typical size of a neuronal cell body, so one section would contain no more than a monolayer of cells. The CCD detector captures images at hundreds of frames per second, so when the technique was demonstrated in the mouse accessory olfactory system, population calcium

transients were clean and distinct. One concern for this technique is that in scattering tissues, the light sheet illumination may not be uniform. In fact, Holekamp et al. pointed out the consequences of this non-uniformity: imaging depth is limited to ≈150 μm and deep-lying cells tend to be imaged at reduced spatial resolution. For neural systems with certain geometries, such as the epithelium-like cell layer demonstrated here, this approach improves imaging speed 100-fold without losing the sectioning capability to observe single cells.

Bridging the gap with behavioral studies. A significant improvement in *in vivo* experimental preparation was presented in a convincing paper by Dombeck et al. [Dombeck et al., 2008]. Many *in vivo* two-photon microscopy studies have been performed on anesthetized animals, because microscopes are not portable and miniaturization compromises the spatial resolution or field of view. To extend imaging to awake animals, Dombeck et al. took inspiration from insect experiments where one part of the body is fixed, for example by a tiny glob of glue, but the rest of the insect is unrestrained. In their scheme, a mouse is head-fixed to the microscope but its feet are grounded on an air-supported floating Styrofoam ball. The ball acts as a spherical treadmill where the mouse can rest or run. Most importantly, awake mice seem at ease in this head-fixed, ball-supporting setup after only a short adaptation session.

Using this "mouse-on-a-ball" setup, Dombeck et al. were able to monitor the movement of the mouse while doing population calcium imaging through a cranial window. The system was remarkably stable such that they observed lateral displacements of <5 μm and minimal axial displacement. Moreover, spatial resolution was higher than miniature two-photon microscopes because tabletop optics were used. As a result, this work opens up exciting, new lines of experiments where behavior of awake, mobile mice can be studied in conjunction with population calcium imaging of neural circuits. For

instance, one could imagine a virtual reality display set up around the mouse to simulate a maze to evoke neuronal activity responsible for decision-making and spatial learning.

A comparison with multi-electrode arrays. The combination of these technical advances is bringing population calcium imaging to almost the same level as the traditional strengths of multi-electrode arrays [Buzsáki, 2004]. The temporal resolution of imaging, demonstrated by using AODs on selected areas or by using objective-coupled planar illumination, is in the millisecond time scale. Behavior studies, which have been the forte of multi-electrode array experiments, can now be simulated by a virtual reality, mobile mouse setup. In addition, a distinct advantage of optical imaging is its compatibility with transgenic models that express fluorescent markers for genetically identifying cells. However, repeated population calcium imaging sessions, the equivalent to chronic electrode recordings, has not yet been demonstrated. Moreover, AM-ester calcium indicator dyes label predominantly the cell bodies, so measured fluorescence changes reflect calcium influx in the soma, but not in the neurites.

An interesting comparison can be made between population calcium imaging and two-dimensional planar electrode arrays [Hutzler et al., 2006]. In planar arrays, neuronal cultures or organotypic slices are grown on a grid of microfabricated transistors, which permits recording from multiple cells. The spatial resolution, defined by the number of elements in the array, can be reduced to single-cell sizes for a millimeter-wide field. Also possible (but not demonstrated by [Hutzler et al., 2006]) is the ability to use the same recording transistors for stimulation, allowing exquisite control at single-cell level. This dual ability to stimulate and record can be a powerful tool for dissecting neural circuits by enabling perturbation of one element at a time. Single-cell stimulation is not yet possible in population calcium imaging, although there is hope with the rapid progress of light-gated ion channels.

Lost in the translation: going from electrons to calcium. With these new imaging tools, are we any closer to understanding neural circuits? Missing in many imaging-only experiments is complementary knowledge of the circuit, including the intrinsic properties of each neuron type and the synaptic connections between them. By going from recording membrane potential to imaging calcium, only the suprathreshold activities are measured. With additional analysis, it is possible to recover characteristics such as the firing rate from fluorescence traces with a very good signal-to-noise ratio [Yaksi & Friedrich, 2006]. Nonetheless, it is not yet possible to use fluorescence to distinguish between such neuronal firing mechanisms as plateau potentials and post-inhibitory rebound, which have been shown to be essential for understanding simpler, invertebrate neural circuits.

Part of the difficulty in going from firing patterns to circuit operation is also the lack of connectivity information. One can imagine the possibility of partially recovering some information on neuronal firing mechanisms from fluorescence data if we know how each neuron is connected to another. Detailed connectivity information includes synapse locations and dendritic branching patterns, which can currently be obtained from several neurons by 3-D neuron tracing or from fixed tissues by electron microscopy. But if the detailed connectivity is unknown, as is the case for neural circuits with more than tens of cells in live tissues, then it is an intractable problem to figure out how the neural circuit computes to generate the changing firing patterns that we observe.

New optical tools come to the rescue. Major technical advances have made population calcium imaging an excellent tool for looking at a neural circuit's firing pattern, which is likely to be computationally relevant. This type of imaging is also one of the very few ways to observe a circuit and all of its components in action at single-cell resolution. On

the other hand, to truly understand neural circuits, more information about subthreshold activity and connectivity is needed. This challenge highlights, again, one key advantage of population calcium imaging, which is its compatibility with other optical techniques. Emerging methods, such as two-photon uncaging for mapping functional connectivity [Matsuzaki et al., 2008] or development of better voltage-sensitive fluorescent dyes [Kuhn et al., 2008], are promising a future where we can measure multiple aspects of a neural circuit at the same time.

CHAPTER 6

CONCLUSION AND FUTURE RESEARCH

In the preceding Chapters, I have described how TPF and SHG microscopy can be used to probe the structure and function of neural circuits with specific examples. In Chapter 2, SHG microscopy reveals an age-dependent, neurite-specific organization of polarized microtubule arrays in the mouse hippocampus and neocortex. In Chapter 3, intrinsic TPF and SHG were observed at senile plaques of brain slices from AD mouse models and their emission spectra were characterized. In Chapter 4, two-photon calcium imaging was applied to find the timing and pattern of spiking activity of one genetically-defined set of excitatory interneurons in the mouse spinal cord. In Chapter 5, several technical improvements to two-photon calcium imaging were highlighted in relation to the study of neural circuits.

Recent molecular advances may provide a sensitive tool for determining microtubule polarity within fine neuronal processes. One protein family, EB1, preferentially binds to the plus-ends of polymerizing microtubules [Akhmanova & Hoogenraad, 2005]. By fluorescently labeling these proteins and then tracking their trajectories, it is possible to estimate the orientations of plus-end-distal microtubule arrays in a neurite. This approach has been used to estimate microtubule polarity in various neurons in the fruit flies [Stone et al., 2008]. Surprisingly, Stone et al. found that in fruit flies, dendrites have polarized microtubules that are minus-end distal, opposite to what was expected in mammalian neurons (see Chapter 2). Similar approach should be possible in mice such that the sign of the polarity of dendritic microtubule arrays observed in Chapter 2 can be resolved. Transfection of EB1-GFP has been demonstrated in dendrites of dissociated neuronal cultures [Jaworski et al., 2009] and may be possibly extended to native brain tissues via *in vivo* two-photon-guided transfection [Kitamura et al., 2008].

The original motivation for the research in Chapter 3 was to investigate the interaction between neuronal microtubule arrays and NFTs. Autofluorescence from NFT was initially observed in unfixed human post-mortem tissues [Zipfel et al., 2003a]. Unfortunately NFTs were not found in the AD mouse models studied, so future research can focus on measuring intrinsic emissions in NFT-bearing mouse models, for example rTg4510 mice [Spires-Jones et al., 2008]. The source of autofluorescence observed in senile plaques may be better understood if the intrinsic optical emissions can be correlated with conformational states of aggregation, some of which can be classified based on immunohistochemistry [Lee et al., 2006, Oddo et al., 2006]. Another fruitful avenue will be to use two-photon calcium imaging, as described in Chapter 4, to investigate calcium unbalance related to neurodegenerative diseases. Recent experiments [Kuchibhotla et al., 2005, Busche et al., 2008] showed that brain calcium regulation may be very different between AD and wild type mice.

The experiments in Chapter 4 attempted to link the neuronal activity to the motor output during fictive locomotion. Correlating with behavior is necessary for understanding neural circuits, which are nonlinear and dynamical [Buzsáki, 2006], making any investigation irrelevant if not linked to a biological framework. This type of behavioral imaging studies may finally be possible now due to progress in head-restrained, awake mouse studies [Kleinfeld & Griesbeck, 2005, Dombeck et al., 2008, Poulet & Petersen, 2008]. Moreover, the development of better genetically-encoded calcium indicators [Heim et al., 2007, Wallace et al., 2008] can also streamline experiments and permit time-lapse investigations that are not possible with current dye-loading technologies.

APPENDIX A

PROTOCOL FOR LABELING NEURONAL POPULATIONS WITH AM-ESTER FLUORESCENT DYES

This protocol is modified from the procedures described in [Stosiek et al., 2003, Garaschuk et al., 2006]. These steps have been used to label neuronal populations with AM-ester fluorescent dyes in hippocampal slices and in neonatal spinal cords, e.g. in Chapter 4. Successful dye loading will result in a uniformly-labeled area, ≈400 μm in diameter [Stosiek et al., 2003], that contains many cells and few bright specks (Fig. A.1).

1. Pull patch pipettes (outer diameter 1.5 mm, borosilicate glass, filament, 1-4 MΩ).
2. From 5 mL sealed glass vials of DMSO (e.g. from Sigma), aliquot into 0.5 mL tubes and store in desiccator. Fresh DMSO, at most week-old, is essential.
3. Put 50 mg pluronic F-127 into 0.25 mL DMSO to make 20% solution, stir until dissolved on hot plate (about 10 min).
4. Add the pluronic/DMSO solution (≈ 4.0 μL, depending on molecular weight of the dye) to 5 mg AM-ester fluorescent dyes (e.g. "Special-packaged" Oregon Green BAPTA-1 AM or Fluo-3 AM from Invitrogen) to make 10 mM.
5. Vortex for 15 s so the pluronic/DMSO solution would catch all the dyes that were stuck to the sides of the vial.
6. Centrifuge for several seconds so the dye solution sits at bottom of the vial.
7. Fill sonicator with room temperature water.
8. Sonicate for 5 min.
9. Add the pipette solution, consisting of 150 mM NaCl, 2.5 mM KCl, 10 mM HEPES, to dilute the dye solution 1:10 (≈ 36 μL).

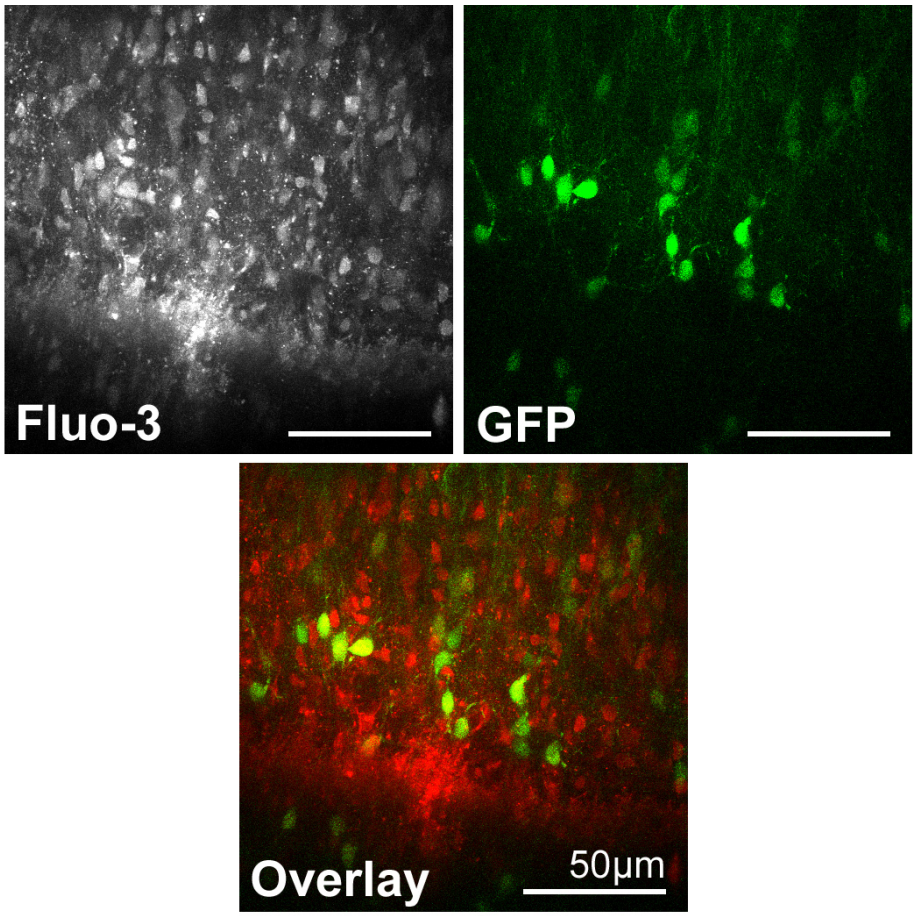

Figure A.1: Ventral spinal cord labeled by bolus injection of AM-ester fluorescent calcium indicator dyes. In this transgenic Hb9-GFP mouse line, a set of excitatory interneurons is expressing GFP, which can be spectrally separated from the injected Fluo-3-AM.

10. Vortex for 15 s and looking for a clear, well-mixed dye solution.

11. Sonicate for 20 min.

12. Pipette dye solution onto a 0.22 μm microcentrifuge filter. The solution should have no floating particulates. Spin for 10 s at high speed such that solution filters through the membrane.

13. Use slendar, plastic tips (e.g. μLoader, Eppendorf) to fill pipette.

14. Insert pipette into tissue with a holding pressure of 4 psi and eject dye for 1-10 min at 10 psi.
15. Incubate the tissue and wait for the dye to be either internalized or washed away. For neonatal mouse spinal cords at room temperature, optimal loading is usually seen in 1 hr.

APPENDIX B

PROTOCOL FOR IMMUNOHISTOCHEMISTRY OF DISSOCIATED HIPPOCAMPAL CULTURES

This protocol is modified from the procedures described in [Dombeck et al., 2003, Schwamborn et al., 2006]. These steps have been used to stain dissociated hippocampal cultures for Tau-1 and MAP-2 (Figs. 2.6 and B.1).

Supplies:

- Formaldehyde (high quality, e.g. Polysciences Inc. 18814)
- Triton-X 100
- Phosphate buffer solution (PBS)
- Goat serum
- Primary antibody 1 (e.g. Mouse, Tau-1, Chemicon MAB3420)
- Primary antibody 2 (e.g. Rabbit, MAP-2, Chemicon AB5622)
- Secondary antibody 1, Alexa 488 goat anti-mouse IgG highly cross-absorbed (e.g. Invitrogen A-11029, 2 mg/mL, 0.5 mL)
- Secondary antibody 2, Alexa 568 goat anti-rabbit IgG highly cross-absorbed (e.g. Invitrogen A-11036, 2 mg/mL, 0.5 mL)
- Antifade (Vectashield)

All at room temperature unless otherwise specified:

Fix in paraformaldehyde:

1. Add 2 mL 3.7% fresh paraformaldehyde to PBS containing 15% sucrose (1.5 g sucrose in 10 mL PBS) at 4 °C to the culture dish.

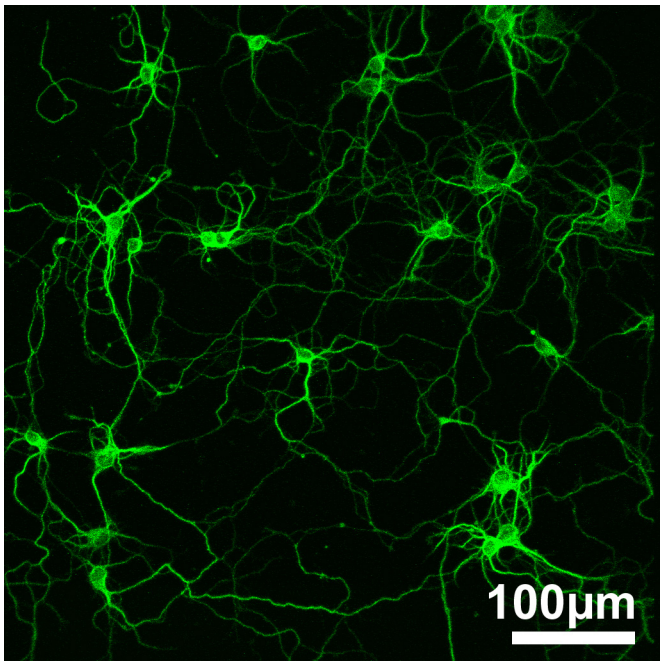

Figure B.1: Dissociated hippocampal culture stained for MAP-2. Image taken with a Bio-Rad MRC1024 confocal microscope with 568 nm excitation. Successful application of this protocol results in uniform staining in the cell bodies and fine neurites.

2. Let sit for 20 min in refrigerator at 4 °C.

3. Aspirate off the paraformaldehyde solution and wash with PBS (3 x 5 min).

Permeate the cells:

1. Add 2 mL PBS containing 0.1% Triton X-100 and 0.1% sodium citrate for 3 min at 4 °C.

2. Wash with PBS (3 x 5 min).

3. Add 2 mL PBS containing 10% horse serum for and let sit for 1 hr.

Primary antibody application:

1. Aspirate off PBS.
2. Add 1 mL PBS containing 10% goat serum.
3. Add 2.5 μL of Tau-1 primary antibody for a dilution of 1:400.
4. Add 2 μL of MAP-2 primary antibody for a dilution of 1:500.
5. Let sit overnight.

Wash primary antibody out:

1. Wash with PBS (3 x 5 min).
2. Return to 1 mL PBS containing 10% goat serum.

Secondary antibody application

1. Add anti-rabbit secondary (add 25 μL aliquot to 1 mL PBS) for a dilution of 40:1.
2. Add anti-mouse secondary (add 25 μL aliquot to 1 mL PBS) for a dilution of 40:1.
3. Let sit for 90 min.

Add Anitfade:

1. Wash with PBS (3 x 5 min).
2. Aspirate off PBS so cells just moist.
3. Add Antifade to fill the center well of the cultured dish ($\approx$6 drops).
4. Cover with coverslip without inducing air bubbles.
5. Store and image in this form within several days.

APPENDIX C

PROTOCOL FOR PREPARING CRANIAL WINDOWS FOR *IN VIVO* RODENT IMAGING

This protocol is based on the procedures described in [Christie et al., 2002] with additional details learned from the lab of Dr. Maiken Nedergaard at the University of Rochester Medical Center. These steps have been uesd to image the olfactory bulb (Fig. 1.4) and neocortex (Figs. 1.2 and 1.5).

1. Restrain the mouse by gently gripping the neck area. For a 25-30 g mouse, anesthetize with intraperitoneal injection of 60 mg/kg ketamine and 10 mg/kg xylazine. Wait 5 min for the anesthetics to kick in. Subsequently, every 30-45 min, apply half the dosage to maintain anesthesia. (Alternatively, application of continuous isoflurane via tracheal artificial ventilation would be better for maintaining rodent health)
2. Put the mouse in a stereotaxic frame and stabilize the head with ear bars. A heating pad should be used to keep the mouse warm.
3. Shave the hair above the surgical area to avoid obstruction during surgery.
4. Use a scribe or a pair of scissors to make an incision above the location of the cranial window. Spread the skin apart. If all connective tissues are cut, the skin will not flex back into the exposed area.
5. Fill the exposed area with a few drops of 10% ferric chloride. This step dries the surgical area and prepares for a clean surface to drill on. Wipe, in one direction, with absorbent paper.
6. Mix the dental acrylic cement. Diluting the two-part mixture allows more fiddle time during gluing but lengthens the set time. The strength of the cement does not seem to depend on the dilution. Fill the exposed area with dental cement.

7. Press a custom steel plate onto head. Steel plates can be made from thin stainless steel sheets with one large punched hole (for cranial window) between two smaller holes (for bolting onto fixture). Scoop away extra cement from the large hole. Depending on dilution, wait 10 min for cement to set.

8. Secure the mouse by bolting down the two small holes onto a fixture. Perfuse artificial cerebrospinal fluid (ACSF), kept cold in an iced bucket, onto the steel plate so it flows through the drilling area and is collected by a plastic dish. Cold ACSF reduces heating during drilling.

9. Begin drilling with a foot pedal-operated drill equipped with a small-diameter burr. Side illuminated light accentuates features. Initially drill away extra cement on the steel plate to prepare a flat surface for coverslip. Then drill the extra cement on top of skull.

10. Once the cement is gone, drill the skull above the cortex to be exposed. Move the burr in circular path corresponding to the size of cranial window. Do not press drill into the cortex. Do not drill through completely. For thinned skull experiment, stop when the skull becomes almost translucent (Fig. C.1). For cranial windows, when the skull is thinned enough, use one tip of foreceps to gently flip skull open.

11. Use sharp foreceps to remove the dura, which for most parts is mostly translucent but for some area is slightly red. Grip the dura near the edge of the exposed cortex. Pull and rip the dura in one direction, remembering that the dura consists of fibers oriented parallel to midline.

12. Stop the ACSF perfusion. To label topically, apply drops of dye (e.g. Sulforhodamine 101) onto the exposed cortex and cover with parafilm to avoid evaporation. Cover the animal with aluminum foil. Wait for the dye to penetrate and then perfuse with ACSF again to wash away the excess dye.

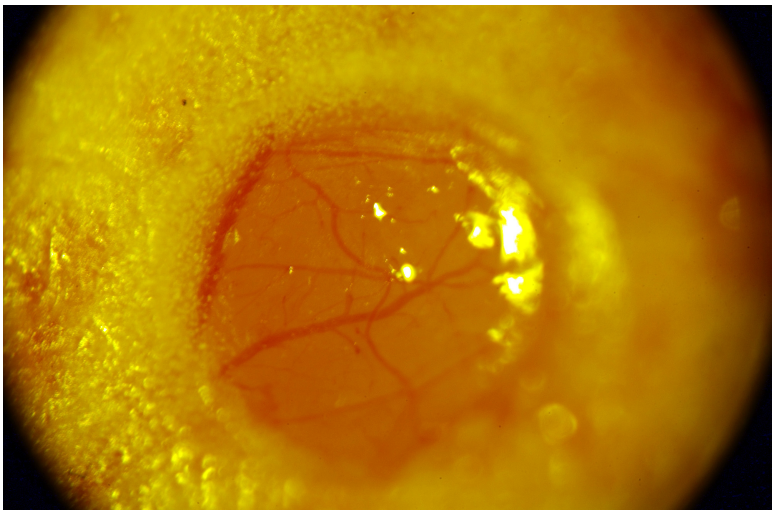

Figure C.1: Thinned skull for *in vivo* rodent imaging of the neocortex. Ideally the skull should be thinned until the vasculatures are clearly visible.

13. Prepare 0.75% agar (e.g. Sigma Type III-A) by heating and then maintain at about 40°C.

14. Apply the agar to the exposed cortex. Overfill a little. Place a micro-coverslip on top of the agar. Scribe away the extra agar around the coverslip.

15. Apply more dental acrylic cement around the coverslip. Make a small well to keep in the solution for immersion dipping optics.

APPENDIX D

PROTOCOL FOR PREPARING HIPPOCAMPAL BRAIN SLICES

This protocol is used to prepare brain slices used for Chapter 2 and 3.

Supplies:

- Vibratome (e.g. Campden Instruments Integraslice 7550 PSDS), including a 765 Peltier cooling unit, a SMZ-140 stereo zoom eyepiece, an U-shaped rack with black rubber pedestal, and a NESLab RTE-101 water chiller
- Disposable razor blades (e.g. Campden Instruments PN#752/1/SS stainless steel or PN#7550/1/C ceramic blades)
- Dish of agar (2% by weight), stored in refrigerator with wet towel on top to prevent drying up
- Surgical tools (e.g. ToughCut Mayo with 17 cm curved blade, ToughCut iris scissors with 11.5 cm straight sharp-sharp blade, hippocampal dissecting tool, standard scalpel 12 cm #3 solid handle plus blade, Foreceps with 11 cm standard tip, all from Fine Science Tools)
- Paint brush (e.g. Princeton Art and Brush Co. 4000R, size 2/0, round)
- Super glue (e.g. Loctite 495 instant adhesive)
- Slice chamber (Nylon mesh-bottomed cubes, see [Sakmann & Stuart, 1983])
- Transfer pipettes, cut tip to make a large opening for sucking up brain slices
- Plastic bags for disposing bodies
- Absorbent mat
- Thick glass petri-dish with Sylgard-gel bottom, sits on ice pack
- Ice bucket with crushed ice

- Water bath (e.g. Precision, stainless steel water bath model 182)

1. Prepare 2 L of fresh artificial cerebrospinal fluid (ACSF, e.g. according to recipes suggested in [Kirov et al., 2003] for mouse).
2. Set 500 mL of ACSF in a bucket of crushed ice and bubbled with 95% O_2 and 5% CO_2.
3. Insert a new razor blade into the vibratome. Make sure the blade edge is level.
4. Fill the vibratome rack and dissection petri-dish with ice-cold, bubbled ACSF.
5. Fill the slice chamber beaker with bubbled ACSF and set in the water bath set at 37 °C.
6. Cut a small $\approx$1 cm^3 cube of agar.
7. Set the vibratome to Freq = 95 Hz, Ampl. = 1.0 mm, Advance 0.15 mm/s.
8. For mice younger than postnatal day 10, euthanize by cervical dislocation, otherwise if mice are older, euthanize by CO_2 inhalation (check with current animal care IACUC guidelines). Decapitate with the large Mayo scissors.
9. Cut the skin down the midline of the head with the small scissors and pull back scalp.
10. Make a straight cut along the midline of the skull. Use foreceps to peel back the skull cap halves to expose the forebrain. Alternatively, cut along the left and right of the skull cap and then lift the entire cap towards the nose.
11. Scoop out the forebrain with the hippocampal dissection tool and immerse it in the bubbling, iced ACSF-filled dissection dish.
12. Use a razor blade to cut the forebrain. To make hippocampal slices, the line of cut is between two points: the anterior midline and the posterior lateral, or $\approx 30^\circ$ away from the midline considering the anterior midline point as the hinge.

13. Spread a thin layer of super glue onto the dried surface of the rubber pedestal of the U-shaped rack.

14. Use the hippocampal dissection tool to place the forebrain onto the absorbent mat to dry and then onto the pedestal, with the recently cut and exposed surface facing down.

15. Place the agar cube behind the forebrain and nudge so the agar will be the resisting force towards the vibratome.

16. Insert the U-shaped rack into the vibratome.

17. Use the vibratome to make ≈250 to 400 μm-thick slices. Carefully use the paint brush to detach slices from the forebrain and then pick up using the wide-mouth transfer pipette. Depending on the age and the desired slice thickness, one brain can yield ≈5 useful hippocampal slices.

18. Transfer slices to the slice chamber in the heated water bath and incubate for 1 hr at 37 ° before imaging.

APPENDIX E

A BRIEF SURVEY OF INSTRUMENTATION ADVANCES IN NONLINEAR MICROSCOPY

A basic TPF and SHG microscope can have a simple anatomy (Fig. 1.2), which has led to several do-it-yourself guides [Majewska et al., 2000, Tsai et al., 2002, Mertz, 2005, Vucinic & Sejnowski, 2007] and commercial instruments. However, despite the availability of commercial off-the-shelf microscopes, many laboratories continue to modify instruments to suit their research needs. I will survey the core components of a multiphoton microscope and discuss the merits of home-brew modifications.

Laser sources and delivery. Currently, the popular choice for excitation source is the mode-locked titanium-sapphire laser. This laser is capable of generating ultrashort pulses with ≈100 fs duration and high peak intensity, both critical requirements for obtaining a detectable amount of TPF and SHG in biological specimens. Furthermore, wavelength is tunable from ≈ 700-1000 nm, a range that is useful for exciting many inorganic dyes and fluorescent proteins. Other lasers have also been used for multiphoton microscopy. Single-wavelength pulsed sources such as a 1064 nm fiber laser [Dombeck et al., 2005] and a 1033 nm Yb:KYW laser [Vucinic & Sejnowski, 2007] have been used in experiments that demanded higher wavelengths. Continuous-wave [Hell et al., 1998] and picosecond-duration pulsed lasers can also be used to image exceptionally bright samples. There is a review for the various laser sources used for multiphoton microscopy [Wise, 2005].

More fluorescence can be obtained by using an excitation source with reduced pulse duration or higher peak intensity. Pulse duration can be reduced using a variety of techniques, although practically, compensation for dispersion within the specimen is not trivial and would vary from sample to sample. To increase peak power, regenerative

amplifiers have been used [Theer et al., 2003] to extend the imaging depth to ≈1 mm within scattering brain tissues. However, the improvement comes at the expense of reduced laser repetitive rate, which limits the microscope's scanning speed. There is also evidence that reduced repetition rate [Donnert et al., 2007] or low peak power with increased repetition rate [Ji et al., 2008] can reduce photobleaching .

Laser intensity can be controlled by employing an electro-optical modulator, i.e. a Pockels cell, which can have transmittance up to ≈95% and a rejection ratio of ≈1:500. A Pockels cell is generally preferred over the more dispersive acoustic-optical tunable filters that are commonly used in confocal microscopy. Depending on the electronics, a Pockels cell can be driven to switch from off-to-on in <0.1 μs, which is useful for time-dependent applications such as fluorescence recovery after photobleaching [Brown et al., 1999] and fluorescence lifetime measurements [Heikal et al., 2001]. Recent studies have also tried to modify and engineering the spectral content of the laser pulses. By using a diffraction grating to spatially separate the frequency components and then a spatial light modulator to change their relative phase, it has been demonstrated that coherent control can be applied to multiphoton microscopy for selective excitation of a subset of fluorophores [Dela Cruz et al., 2004].

Much effort has been devoted to optical fiber delivery so the microscope can be separated from the laser and be more compact for such applications as endoscopy and imaging moving rodents. The main challenge of delivering ultrafast pulses with optical fibers had been unwanted nonlinear interactions such as group velocity dispersion and self-phase modulation. In early versions of fiber-based microscope [Helmchen et al., 2001], pulses delivered by a single-mode fiber were dispersion compensated, but self-phase modulation would broaden the pulse to ≈1 ps. Recently, several research groups have switched to photonic bandgap fibers, which can deliver pulses with less distortion

[Ouzounov et al., 2002]. The use of fiber delivery and other miniaturization efforts have led to microscope designs that weigh only 0.6 g [Engelbrecht et al., 2008].

Beam scanning. Many commercial microscopes scan the laser beam in *x*-*y* directions using a pair of mirrors driven by mechanical galvanometers. Galvanometers can scan at ≈2 kHz within its angular range, which translates to ≈0.5 ms per line, or ≈4 frames per second for a 512 × 512 image. Small mirrors with ≈5 mm-diameter apertures are typically used to reduce the mechanical load on galvanometers, so the beam must be expanded after the scanner to fill the back aperture of the objective.

Because many biological processes occur in the milliseconds time scale, there is significant incentive to increase the scanning speed. One method of rapid scanning is to split the beam into "beamlets" so many foci can be scanned concurrently. Beam splitting can be done by a microlens array on a Nipkow-style spinning disk [Bewersdorf et al., 1998] or by an etalon of cascaded beamsplitters [Fittinghoff et al., 2000]. Point spread function overlap between the foci, which can reduce the axial resolution (but see [Andresen et al., 2001]). Using this multi-foci approach, scanning speed, constrained by a practical limit on producing many beamlets of uniform intensity, can be >25 Hz for a full frame image. However, scattered photons can be assigned to the wrong beamlet, which renders this method unsuitable for deep-tissue imaging.

Scanning speed is also constrained by signal-to-noise at each pixel due to finite fluorescence photon flux, so a promising approach for rapid scanning is to steer the beam with acoustic-optical deflectors (AOD) [Iyer et al., 2003]. This method enables random-access scanning, where the beam can be repeatedly steered to and dwelled at several *x*-*y* positions, unlike galvanometers where the scanning is sequential. Access time can be as fast as ≈5-15 μs, where smaller AODs tend to decrease access time but are more

prone to beam walk-off. Low noise of the AOD leads to high positional accuracy. The main disadvantage is optical complexity because the severe dispersion from AODs must be compensated. In particular, diffraction of the polychromatic pulse leads to angular spread, which can significantly reduce spatial resolution. This problem can be remedied by using prisms [Roorda et al., 2004] or diffraction grating [Iyer et al., 2003], although perfect compensation is difficult to achieve because of the wavelength dependence.

Adding the *z*-axis to *x*-*y* scanning allows for more rapid imaging of a three-dimensional volume. Piezoelectric elements have been used to drive the relatively heavy objective lens, which can oscillate at ≈10 Hz with a range of ≈250 μm [Gobel et al., 2007]. An interesting development is to use group velocity dispersion as a focusing mechanism [Durst et al., 2006, Oron et al., 2005]. In this approach, a grating is used to spatially separate spectral components of a pulse, which then are recombined after the objective lens so the pulse duration is shortest at the spatial focus hence maximizing multiphoton excitation. It may be possible to reject out-of-background fluorescence by this method, although this has yet to be demonstrated.

There are designs for compact scanners that work with fiber-based microscopes. One scanning mechanism oscillates the tip of the beam-delivering fiber using a piezoelectric actuator in a repeating pattern that would cover the field of view [Helmchen et al., 2001]. Another method uses microfabricated mirrors, which can scan at speeds comparable to conventional galvanometers [Piyawattanametha et al., 2006].

Microscope objectives. Microscope objectives are generally designed to minimize spherical and chromatic aberrations, but multiphoton microscopy demands several additional features. First, the objective should have high transmission at infrared wavelengths. Second, it is advantageous to expand the laser beam to overfill the back aperture and use an objective with high numerical aperture to obtain the best spatial resolution.

Third, low magnification and a large exit pupil are important for maximizing the collection of scattered photons when imaging deep within tissues [Oheim et al., 2001].

To image structures deep within tissues, gradient index (GRIN) lenses have been used as a rigid stick objective that can be inserted into the tissue [Levene et al., 2004, Jung & Schnitzer, 2003]. The lens is a compact glass rod ≈350 μm in diameter and can be readily integrated into designs for fiber-based microscopes [Flusberg et al., 2005]. Aberrations lead to lower spatial resolution (≈1 μm lateral, ≈15 μm axial), but the bigger concern is the mechanical damage of tissues near the lens because working distance tends to be small (≈150 μm) and the imaged area may be compressed. Other techniques, such as adaptive optics [Rueckel et al., 2006] and clever subtraction of background fluorescence [Leray et al., 2007], may also be useful for extending imaging depth.

Detectors. Bi-alkali photomultiplier tubes (PMTs) have been the workhorse in multiphoton microscopes for many years. These detectors provide reasonable quantum efficiency, ≈25% at visible wavelengths, and yet are relatively blind to the laser wavelengths. Suitable for non-descanned detection, these detectors can have a large active area. More importantly, PMTs in general have linear gain over a large dynamic range such that the current output is proportional to the photon number, which simplifies the electronics and image analysis. In some cases, multi-alkali PMTs are used instead for their higher quantum efficiency at wavelengths >525 nm.

In the last few years, several new types of photomultiplier tubes have been introduced. Gallium arsenide phosphate (GaAsP) PMTs have higher quantum efficiency at ≈40% and are well-suited for imaging green fluorescent proteins and many of its redshifted variants. Recently, new models of bi-alkali PMTs, called "super bi-alkali" and "ultra bi-alkali," have also been introduced and promise even higher quantum efficiencies.

Other than PMTs, CCD cameras and avalanche diodes can also detect fluorescence. So far, CCD cameras have been used in microscopes when spatial information is needed, for example in multi-focal scanning. Avalanche diodes boast superior quantum efficiencies but have relatively long dead time between counted photons, so the signal and photon count may not be linear even with modest amount of fluorescence.

Commercial instruments. The technology of multiphoton microscopy has been patented and licensed for producing commercial instruments. In 1996, Bio-Rad Laboratories introduced MRC-1024, the first laser-scanning microscope with multiphoton capability. This microscope has several unique features including the ability to do photon counting in each detector. This system was followed by the Radiance 2000 and 2100 systems, which were released in 1999 and contain a Rainbow attachment for spectral imaging. At about the same time, Carl Zeiss Inc. released the LSM 510 NLO. This system led to a patent infringement case, which culminated in the acquisition of Bio-Rad's Cell Science Division by Carl Zeiss Inc. in 2004. As of 2008, the LSM 510 is the licensed commercial multiphoton microscope. Sub-licenses have also been granted to companies that build multiphoton microscopes with special capabilities, such as to Prairie Technologies for adding another laser for two-photon uncaging and to LaVision BioTec for building a multi-focal scanner.

REFERENCES

[Akhmanova & Hoogenraad, 2005] Akhmanova, A. & Hoogenraad, C. C. (2005). Microtubule plus-end-tracking proteins: mechanisms and functions. Curr Opin Cell Biol 17, 47–54.

[Alpár et al., 2006] Alpár, A., Ueberham, U., Bruckner, M. K., Seeger, G., Arendt, T. & Gartner, U. (2006). Different dendrite and dendritic spine alterations in basal and apical arbors in mutant human amyloid precursor protein transgenic mice. Brain Res 1099, 189–198.

[Andresen et al., 2001] Andresen, V., Egner, A. & Hell, S. W. (2001). Time-multiplexed multifocal multiphoton microscope. Opt Lett 26, 75–77.

[Arber et al., 1999] Arber, S., Han, B., Mendelsohn, M., Smith, M., Jessell, T. M. & Sockanathan, S. (1999). Requirement for the homeobox gene hb9 in the consolidation of motor neuron identity. Neuron 23, 659–674.

[Atwood et al., 2002] Atwood, C. S., Martins, R. N., Smith, M. A. & Perry, G. (2002). Senile plaque composition and posttranslational modification of amyloid-beta peptide and associated proteins. Peptides 23, 1343–1350.

[Baas, 1999] Baas, P. W. (1999). Microtubules and neuronal polarity: Lessons from mitosis. Neuron 22, 23–31.

[Baas et al., 1993] Baas, P. W., Ahmad, F. J., Pienkowski, T. P., Brown, A. & Black, M. M. (1993). Sites of microtubule stabilization for the axon. J Neurosci 13, 2177–2185.

[Baas et al., 1989] Baas, P. W., Black, M. M. & Banker, G. A. (1989). Changes in microtubule polarity orientation during the development of hippocampal neurons in culture. J Cell Biol 109, 3085–3094.

[Baas et al., 1988] Baas, P. W., Deitch, J. S., Black, M. M. & Banker, G. A. (1988). Polarity orientation of microtubules in hippocampal neurons: Uniformity in the axon and nonuniformity in the dendrite. Proc Natl Acad Sci USA 85, 8335–8339.

[Bacskai et al., 2001] Bacskai, B. J., Kajdasz, S. T., Christie, R. H., Carter, C., Games, D., Seubert, P., Schenk, D. & Hyman, B. T. (2001). Imaging of amyloid-beta deposits in brains of living mice permits direct observation of clearance of plaques with immunotherapy. Nat Med 7, 369–372.

[Ballatore et al., 2007] Ballatore, C., Lee, V. M. & Trojanowski, J. Q. (2007). Tau-mediated neurodegeneration in Alzheimer's disease and related disorders. Nat Rev Neurosci 8, 663–672.

[Bates et al., 2007] Bates, M., Huang, B., Dempsey, G. T. & Zhuang, X. (2007). Multicolor superresolution imaging with photo-switchable fluorescent probes. Science 317, 1749–1753.

[Berkowitz & Stein, 1994] Berkowitz, A. & Stein, P. S. G. (1994). Activity of descending propriospinal axons in the turtle hindlimb enlargement during two forms of fictive scratching: phase analyses. J Neurosci 14, 5105–5119.

[Bewersdorf et al., 1998] Bewersdorf, J., Pick, R. & Hell, S. W. (1998). Multifocal multiphoton microscopy. Opt Lett 23, 655–657.

[Bonnot et al., 2005] Bonnot, A., Mentis, G. Z., Skoch, J. & O'Donovan, M. J. (2005). Electroporation loading of calcium-sensitive dyes into the cns. J Neurophysiol 93, 1793–1808.

[Bonnot et al., 2002] Bonnot, A., Whelan, P. J., Mentis, G. Z. & O'Donovan, M. J. (2002). Spatiotemporal pattern of motoneuron activation in the rostral lumbar and the sacral segments during locomotor-like activity in the neonatal mouse spinal cord. J Neurosci 22, RC203:1–6.

[Borchelt et al., 1997] Borchelt, D. R., Ratovitski, T., van Lare, J., Lee, M. K., Gonzales, V., Jenkins, N. A., Copeland, N. G., Price, D. L. & Sisodia, S. S. (1997). Accelerated amyloid deposition in the brains of transgenic mice coexpressing mutant presenilin 1 and amyloid precursor proteins. Neuron 19, 939–945.

[Boyd, 2002] Boyd, R. W. (2002). Nonlinear Optics, 2nd Ed. Academic Press, New York, NY.

[Brown et al., 2003] Brown, E., McKee, T., diTomaso, E., Pluen, A., Seed, B., Boucher, Y. & Jain, R. K. (2003). Dynamic imaging of collagen and its modulation in tumors in vivo using second-harmonic generation. Nat Med 9, 796–800.

[Brown et al., 1999] Brown, E. B., Wu, E. S., Zipfel, W. R. & Webb, W. W. (1999). Measurement of molecular diffusion in solution by multiphoton fluorescence photobleaching recovery. Biophys J 77, 2837–2849.

[Brownstone & Wilson, 2008] Brownstone, R. M. & Wilson, J. M. (2008). Strategies

for delineating spinal locomotor rhythm-generating networks and the possible role of Hb9 interneurons in rhythmogenesis. Brain Res Rev 57, 64–76.

[Burton, 1988] Burton, P. R. (1988). Dendrites of mitral cell neurons contain microtubules of opposite polarity. Brain Res 473, 107–115.

[Busche et al., 2008] Busche, M. A., Eichhoff, G., Adelsberger, H., Abramowski, D., Wiederhold, K. H., Haass, C., Staufenbiel, M., Konnerth, A. & Garaschuk, O. (2008). Clusters of hyperactive neurons near amyloid plaques in mouse model of Alzheimer's disease. Science 321, 1686–1689.

[Buzsáki, 2004] Buzsáki, G. (2004). Large-scale recording of neuronal ensembles. Nat Neurosci 7, 446–451.

[Buzsáki, 2006] Buzsáki, G. (2006). Rhythms of the Brain. Oxford University Press, Oxford.

[Calhoun et al., 1998] Calhoun, M. E., Kurth, D., Phinney, A. L., Long, J. M., Hengemihle, J., Mouton, P. R., Ingram, D. K. & Jucker, M. (1998). Hippocampal neuron and synaptophysin-positive bouton number in aging C57BL/6 mice. Neurobiol Aging 19, 599–606.

[Campagnola & Loew, 2003] Campagnola, P. J. & Loew, L. M. (2003). Second-harmonic imaging microscopy for visualizing biomolecular arrays in cells, tissues and organisms. Nat Biotechnol 21, 1356–1360.

[Campagnola et al., 2002] Campagnola, P. J., Millard, A. C., Terasaki, M., Hoppe, P. E., Malone, C. J. & Mohler, W. A. (2002). Three-dimensional high-resolution second-harmonic generation imaging of endogenous structural proteins in biological tissues. Biophys J 82, 493–508.

[Chen et al., 1992] Chen, J., Kanai, Y., Cowan, N. J. & Hirokawa, N. (1992). Projection domains of MAP-2 and tau determine spacings between microtubules in dendrites and axons. Nature 360, 674–677.

[Christie et al., 2002] Christie, R. H., Bacskai, B. J., Zipfel, W. R., Williams, R. M., Kajdasz, S. T., Webb, W. W. & Hyman, B. T. (2002). Growth arrest of individual senile plaques in a model of Alzheimer's disease observed by in vivo multiphoton microscopy. Nature 420, 788–794.

[Davis et al., 1990] Davis, L., Burger, B., Banker, G. A. & Steward, O. (1990). Den-

dritic transport: quantitative analysis of the time course of somatodendritic transport of recently synthesized RNA. J Neurosci 10, 3056–3068.

[Débarre et al., 2006] Débarre, D., Supatto, W., Pena, A. M., Fabre, A., Tordjmann, T., Combettes, L., Schanne-Klein, M. C. & Beaurepaire, E. (2006). Imaging lipid bodies in cells and tissues using third-harmonic generation microscopy. Nat Methods 3, 47–53.

[Dela Cruz et al., 2004] Dela Cruz, J. M., Pastirk, I., Comstock, M., Lozovoy, V. V. & Dantus, M. (2004). Use of coherent control methods through scattering biological tissue to achieve functional imaging. Proc Natl Acad Sci USA 101, 16996–17001.

[Denk et al., 1990] Denk, W., Strickler, J. H. & Webb, W. W. (1990). Two-photon laser scanning fluorescence. Science 248, 73–76.

[Denk & Svoboda, 1997] Denk, W. & Svoboda, K. (1997). Photon upmanship: why multiphoton imaging is more than a gimmick. Neuron 18, 351–357.

[Diez et al., 2003] Diez, M., Koistinaho, J., Kahn, K., Games, D. & Hokfelt, T. (2003). Neuropeptides in hippocampus and cortex in transgenic mice overexpressing V717F beta-amyloid precursor protein initial observations. Neuroscience 100, 259–286.

[Dombeck et al., 2004] Dombeck, D. A., Blanchard-Desce, M. & Webb, W. W. (2004). Optical recording of action potentials with second-harmonic generation microscopy. J Neurosci 24, 999–1003.

[Dombeck et al., 2003] Dombeck, D. A., Kasischke, K. A., Vishwasrao, H. D., Ingelsson, M., Hyman, B. T. & Webb, W. W. (2003). Uniform polarity microtubule assemblies imaged in native brain tissue by second-harmonic generation microscopy. Proc Natl Acad Sci USA 100, 7081–7086.

[Dombeck et al., 2008] Dombeck, D. A., Khabbaz, A. N., Collman, F., Adelman, T. L. & Tank, D. W. (2008). Imaging large-scale neural activity with cellular resolution in awake mobile mice. Neuron 56, 43–57.

[Dombeck et al., 2005] Dombeck, D. A., Sacconi, L., Blanchard-Desce, M. & Webb, W. W. (2005). Optical recording of fast neuronal membrane potential transients in acute mammalian brain slices by second-harmonic generation microscopy. J Neurophysiol 94, 3628–3636.

[Donnert et al., 2007] Donnert, G., Eggeling, C. & Hell, S. W. (2007). Major signal

increase in fluorescence microscopy through dark-state relaxation. Nat Methods 4, 81–86.

[Dowson, 1981] Dowson, J. H. (1981). A sensitive method for demonstration of senile plaques in the dementing brain. Histopathology 5, 305–310.

[Drach et al., 1994] Drach, L. M., Bohl, J. & Goebel, H. H. (1994). The lipofuscin content of nerve cells of the inferior olivary nucleus in Alzheimer's disease. Dementia 5, 234–239.

[Duemani Reddy et al., 2008] Duemani Reddy, G., Kelleher, K., Fink, R. & Saggau, P. (2008). Three-dimensional random access multiphoton microscopy for functional imaging of neuronal activity. Nat Neurosci 11, 713–720.

[Durst et al., 2006] Durst, M. E., Zhu, G. & Xu, C. (2006). Simultaneous spatial and temporal focusing for axial scanning. Opt Express 14, 12243–12254.

[Eichhoff et al., 2008] Eichhoff, G., Busche, M. A. & Garaschuk, O. (2008). In vivo calcium imaging of the aging and diseased brain. Eur J Nucl Med Mol Imaging 35, S99–S106.

[Engelbrecht et al., 2008] Engelbrecht, C., Johnston, R., Seibel, E. & Helmchen, F. (2008). Ultra-compact fiber-optic two-photon microscope for functional fluorescence imaging in vivo. Opt Express 16, 5556–5564.

[Feldman & Del Negro, 2006] Feldman, J. L. & Del Negro, C. A. (2006). Looking for inspiration: new perspective on respiratory rhythm. Nat Rev Neurosci 7, 232–242.

[Feng et al., 2000] Feng, G., Mellor, R. H., Bernstein, M., Keller-Peck, C., Nguyen, Q. T., Wallace, M., Nerbonne, J. M., Lichtman, J. W. & Sanes, J. R. (2000). Imaging neuronal subsets in transgenic mice expressing multiple spectral variants of GFP. Neuron 28, 41–51.

[Ferreira et al., 1987] Ferreira, A., Busciglio, J. & Cáceres, A. (1987). An immunocytochemical analysis of the ontogeny of the microtubule-associated proteins MAP-2 and Tau in the nervous system of the rat. Brain Res 431, 9–31.

[Fetcho et al., 2008] Fetcho, J. R., Higashijima, S. & McLean, D. L. (2008). Zebrafish and motor control over the last decade. Brain Res Rev 57, 86–93.

[Fiala & Harris, 1999] Fiala, J. C. & Harris, K. M. (1999). Dendrite structure. In Dendrites, (G. Stuart, N. S. & Hausser, M., eds), pp. 1–34. Oxford Univ Press New York.

[Fittinghoff et al., 2000] Fittinghoff, D. N., Wiseman, P. W. & Squier, J. A. (2000). Widefield multiphoton and temporally decorrelated multifocal multiphoton microscopy. Opt Express 7, 273–279.

[Flusberg et al., 2005] Flusberg, B. A., Jung, J. C., Cocker, E. D., Anderson, E. P. & Schnitzer, M. J. (2005). In vivo brain imaging using a portable 3.9 gram two-photon fluorescence microendoscope. Opt Lett 30, 2272–2274.

[Garaschuk et al., 2006] Garaschuk, O., Milos, R.-I. & Konnerth, A. (2006). Targeted bulk-loading of fluorescent indicators for two-photon brain imaging in vivo. Nat Protocol 1, 380–386.

[Gobel et al., 2007] Gobel, W., Kampa, B. & Helmchen, F. (2007). Imaging cellular network dynamics in three dimensions using fast 3D laser scanning. Nat Methods 4, 73–79.

[Gobel et al., 2004] Gobel, W., Kerr, J. N., Nimmerjahn, A. & Helmchen, F. (2004). Miniaturized two-photon microscope based on a flexible coherent fiber and a gradient-index lens objective. Opt Lett 29, 2521–2523.

[Gordon & Whelan, 2006] Gordon, I. T. & Whelan, P. J. (2006). Monoaminergic control of cauda-equina-evoked locomotion in the neonatal mouse spinal cord. J Neurophysiol 96, 3122–3129.

[Grillner, 2003] Grillner, S. (2003). The motor infrastructure: from ion channels to neuronal networks. Nat Rev Neurosci 4, 573–586.

[Grooms et al., 2006] Grooms, S. Y., Noh, K.-M., Regis, R., Bassell, G. J., Bryan, M. K., Carroll, R. C. & Zukin, R. S. (2006). Activity bidirectionally regulates AMPA receptor mRNA abundance in dendrites of hippocampal neurons. J Neurosci 26, 8339–8351.

[Grutzendler et al., 2007] Grutzendler, J., Helmin, K., Tsai, J. & Gan, W. B. (2007). Various dendritic abnormalities are associated with fibrillar amyloid deposits in Alzheimer's disease. Ann NY Acad Sci 1097, 30–39.

[Grutzendler et al., 2002] Grutzendler, J., Kasthuri, N. & Gan, W. B. (2002). Long-term dendritic spine stability in the adult cortex. Nature 420, 812–816.

[Guillaud et al., 2003] Guillaud, L., Setou, M. & Hirokawa, N. (2003). KIF17 dynamics and regulation of NR2B trafficking in hippocampal neurons. J Neurosci 23, 131–140.

[Han et al., 2007] Han, P., Nakanishi, S. T., Tran, M. A. & Whelan, P. J. (2007). Dopaminergic modulation of spinal neuronal excitability. J Neurosci 27, 13192–13204.

[Hanlon et al., 2008] Hanlon, E. B., Perelman, L. T., Vitkin, E. I., Greco, F. A., McKee, A. C. & Kowall, N. W. (2008). Scattering differentiates Alzheimer disease in vitro. Opt Lett 33, 624–626.

[Harvey et al., 2008] Harvey, C. D., Yasuda, R., Zhong, H. & Svoboda, K. (2008). The spread of Ras activity triggered by activation of a single dendritic spine. Science 321, 136–140.

[Heidemann & McIntosh, 1980] Heidemann, S. R. & McIntosh, J. R. (1980). Visualization of the structural polarity of microtubules. Nature 286, 517–519.

[Heikal et al., 2001] Heikal, A. A., Hess, S. T. & Webb, W. W. (2001). Multiphoton molecular spectroscopy and excited state dynamics of enhanced green fluorescent protein (EGFP): acid-base specificity. Chem Phys 274, 37–55.

[Heim et al., 2007] Heim, N., Garaschuk, O., Friedrich, M. W., Mank, M., Milos, R. I., Kovalchuk, Y., Konnerth, A. & Griesbeck, O. (2007). Improved calcium imaging in transgenic mice expressing a troponin C-based biosensor. Nat Methods 4, 127–129.

[Hell et al., 1998] Hell, S. W., Booth, M., Wilms, S., Schnetter, C. M., Kirsch, A. K., Arndt-Jovin, D. J. & Jovin, T. M. (1998). Two-photon near- and far-field fluorescence microscopy with continuous-wave excitation. Opt Lett 23, 1238–1240.

[Helmchen et al., 2001] Helmchen, F., Fee, M., Tank, D. & Denk, W. (2001). A miniature head-mounted two-photon microscope: High-resolution brain imaging in freely moving animals. Neuron 31, 903–912.

[Hinckley et al., 2005] Hinckley, C. A., Hartley, R., Wu, L., Todd, A. & Ziskind-Conhaim, L. (2005). Locomotor-like rhythms in a genetically distinct cluster of interneurons in the mammalian spinal cord. J Neurophysiol 26, 8477–8483.

[Hinckley & Ziskind-Conhaim, 2006] Hinckley, C. A. & Ziskind-Conhaim, L. (2006). Electrical coupling between locomotor-related excitatory interneurons in the mammalian spinal cord. J Neurosci 26, 8477–8483.

[Hintersteiner et al., 2005] Hintersteiner, M., Enz, A., Frey, P., Jaton, A. L., Kinzy, W., Kneuer, R., Neumann, U., Rudin, M., Staufenbiel, M., Stoeckli, M., Wiederhold,

K. H. & Gremlich, H. U. (2005). Post-mortem correlates of in vivo PiB-PET amyloid imaging in a typical case of Alzheimer's disease. Nat Biotechnol 23, 577–583.

[Hirokawa, 1998] Hirokawa, N. (1998). Kinesin and dynein superfamily proteins and the mechanism of organelle transport. Science 279, 518–526.

[Hirokawa & Takemura, 2005] Hirokawa, N. & Takemura, R. (2005). Molecular motors and mechanisms of directional transport in neurons. Nat Rev Neurosci 6, 201–214.

[Holekamp et al., 2008] Holekamp, T. F., Turaga, D. & Holy, T. E. (2008). Fast three-dimensional fluorescence imaging of activity in neural populations by objective-coupled planar illumination microscopy. Neuron 57, 661–672.

[Hsiao et al., 1996] Hsiao, K., Chapman, P., Nilsen, S., Eckman, C., Harigaya, Y., Younkin, S., Yang, F. & Cole, G. (1996). Correlative memory deficits, abeta elevation, and amyloid plaques in transgenic mice. Science 274, 99–102.

[Hutzler et al., 2006] Hutzler, M., Lambacher, A., Eversmann, B., Jenkner, M., Thewes, R. & Fromherz, P. (2006). High-resolution multitransistor array recording of electrical field potentials in cultured brain slices. J Neurophysiol 96, 1637–1645.

[Ikonomovic et al., 2008] Ikonomovic, M. D., Klunk, W. E., Abrahamson, E. E., Mathis, C. A., Price, J. C., Tsopelas, N. D., Lopresti, B. J., Ziolko, S., Bi, W., Paljug, W. R., Debnath, M. L., Hope, C. E., Isanski, B. A., Hamilton, R. L. & DeKosky, S. T. (2008). Post-mortem correlates of in vivo PiB-PET amyloid imaging in a typical case of Alzheimer's disease. Brain 131, 1630–1645.

[Iyer et al., 2003] Iyer, V., Losavio, B. & Saggau, P. (2003). Compensation of spatial and temporal dispersion for acousto-optic multiphoton laser-scanning microscopy. J Biomed Opt 8, 460–471.

[Jaworski et al., 2009] Jaworski, J., Kapitein, L. C., Gouveia, S. M., Dortland, B. R., Wulf, P. S., Grigoriev, I., Camera, P., Spangler, S. A., Di Stefano, P., Demmers, J., Krugers, H., Defilippi, P., Akhmanova, A. & Hoogenraad, C. C. (2009). Dynamic microtubules regulate dendritic spine morphology and synaptic plasticity. Neuron 61, 85–100.

[Ji et al., 2008] Ji, N., Magee, J. C. & Betzig, E. (2008). High-speed, low-photodamage nonlinear imaging using passive pulse splitters. Nat Methods 5, 197–202.

[Jiang et al., 1999] Jiang, Z., Rempel, J., Li, J., Sawchuk, M. A., Carlin, K. P. & Brown-

stone, R. M. (1999). Development of L-type calcium channels and a nifedipine-sensitive motor activity in the postnatal mouse spinal cord. Eur J Neurosci 11, 3481–3487.

[Johnston & Amaral, 2004] Johnston, D. & Amaral, D. G. (2004). Hippocampus. In The Synaptic Organization of the Brain, (Shepherd, G. M., ed.), pp. 455–498. Oxford Univ Press New York.

[Jung & Schnitzer, 2003] Jung, J. C. & Schnitzer, M. J. (2003). Multiphoton endoscopy. Opt Lett 28, 902–904.

[Kanai et al., 2004] Kanai, Y., Dohmae, N. & Hirokawa, N. (2004). Kinesin transports RNA: isolation and characterization of an RNA-transporting granule. Neuron 43, 513–525.

[Kasischke et al., 2004] Kasischke, K. A., Vishwasrao, H. D., Fisher, P. J., Zipfel, W. R. & Webb, W. W. (2004). Neural activity triggers neuronal oxidative metabolism followed by astrocytic glycolysis. Science 305, 99–103.

[Kerr et al., 2005] Kerr, J. N., Greenberg, D. & Helmchen, F. (2005). Imaging input and output of neocortical networks in vivo. Proc Natl Acad Sci USA 102, 14063–14068.

[Kiehn, 2006] Kiehn, O. (2006). Locomotor circuits in the mammalian spinal cord. Annu Rev Neurosci 29, 279–306.

[Kirov et al., 2003] Kirov, S. A., Petrak, L. J., Fiala, J. C. & Harris, K. M. (2003). Dendritic spines disappear with chilling but proliferate excessively upon rewarming of mature hippocampus. Neuroscience 127, 69–80.

[Kitamura et al., 2008] Kitamura, K., Judkewitz, B., Kano, M., Denk, W. & Hausser, M. (2008). Targeted patch-clamp recordings and single-cell electroporation of unlabeled neurons in vivo. Nat Methods 5, 61–67.

[Kjaerulff & Kiehn, 1996] Kjaerulff, O. & Kiehn, O. (1996). Distribution of networks generating and coordinating locomotor activity in the neonatal rat spinal cord in vitro: a lesion study. J Neurosci 16, 5777–5794.

[Kleinfeld & Griesbeck, 2005] Kleinfeld, D. & Griesbeck, O. (2005). From art to engineering? The rise of in vivo mammalian electrophysiology through genetically targeted labeling and nonlinear imaging. PLoS Biol 3, 1685–1689.

[Kleinfeld et al., 1998] Kleinfeld, D., Mitra, P. P., Helmchen, F. & Denk, W. (1998).

Fluctuations and stimulus-induced changes in blood flow observed in individual capillaries in layers 2 through 4 of rat neocortex. Proc Natl Acad Sci 95, 15741–15746.

[Kloppenburg et al., 2000] Kloppenburg, P., Zipfel, W. R., Webb, W. W. & Harris-Warrick, R. M. (2000). Highly localized Ca2+ accumulation revealed by multiphoton microscopy in an identified motoneuron, and its modulation by dopamine. J Neurosci 20, 2523–2533.

[Kuchibhotla et al., 2005] Kuchibhotla, K. V., Goldman, S. T., Lattarulo, C. R., Wu, H. Y., Hyman, B. T. & Bacskai, B. J. (2005). Abeta plaques lead to aberrant regulation of calcium homeostasis in vivo resulting in structural and functional disruption of neuronal networks. Neuron 17, 47–54.

[Kudo & Yamada, 1987] Kudo, N. & Yamada, T. (1987). N-methyl-D,L-aspartate-induced locomotor activity in a spinal cord-hindlimb muscle preparation of the newborn rat studied in vitro. Neurosci Lett 75, 43–48.

[Kuhn et al., 2008] Kuhn, B., Denk, W. & Bruno, R. M. (2008). In vivo two-photon voltage-sensitive dye imaging reveals top-down control of cortical layers 1 and 2 during wakefulness. Proc Natl Acad Sci USA 105, 7588–7593.

[Kwan et al., 2008] Kwan, A. C., Dombeck, D. A. & Webb, W. W. (2008). Polarized microtubule arrays in apical dendrites and axons. Proc Natl Acad Sci USA 105, 11370–11375.

[Lafreniere-Roula & McCrea, 2005] Lafreniere-Roula, M. & McCrea, D. A. (2005). Deletions of rhythmic motoneuron activity during fictive locomotion and scratch provide clues to the organization of the mammalian central pattern generator. J Neurophysiol 94, 1120–1132.

[Lakowicz, 1999] Lakowicz, J. R. (1999). Principles of Fluorescence Spectroscopy, 2nd Ed. Springer, New York, NY.

[Lee et al., 2006] Lee, E., Leng, L., Zhang, B., Kwong, L., Trojanowski, J., Abel, T. & Lee, V. (2006). Targeting amyloid-beta peptide (Abeta) oligomers by passive immunization with a conformation-selective monoclonal antibody improves learning and memory in Abeta precursor protein (APP) transgenic mice. J Biol Chem 281, 4292–4299.

[Leray et al., 2007] Leray, A., Lillis, K. & Mertz, J. (2007). Enhanced background rejection in thick tissue with differential-aberration two-photon microscopy. Biophys J 15, 1449–1458.

[Lev-Tov et al., 2000] Lev-Tov, A., Delvolvé, I. & Kremer, E. (2000). Sacrocaudal afferents induce rhythmic efferent bursting in isolated spinal cords of neonatal rats. J Neurophysiol 83, 888–894.

[Levene et al., 2004] Levene, M. J., Dombeck, D. A., Kasischke, K. A., Molloy, R. P. & Webb, W. W. (2004). In vivo multiphoton microscopy of deep brain tissue. J Neurophysiol 91, 1908–1912.

[Lewis et al., 2001] Lewis, J., Dickson, D. W., Lin, W. L., Chisholm, L., Corral, A., Jones, G., Yen, S. H., Sahara, N., Skipper, L., Yager, D., Eckman, C., Hardy, J., Hutton, M. & McGowan, E. (2001). Enhanced neurofibrillary degeneration in transgenic mice expressing mutant tau and APP. Science 293, 1487–1491.

[Li et al., 2007] Li, B., Chohan, M. O., Grundke-Iqbal, I. & Iqbal, K. (2007). Disruption of microtubule network by alzheimer abnormally hyperphosphorylated tau. Acta Neuropathol 113, 501–511.

[Lledo et al., 2006] Lledo, P. M., Alonso, M. & Grubb, M. S. (2006). Adult neurogenesis and functional plasticity in neuronal circuits. Nat Rev Neurosci 7, 179–193.

[Majewska et al., 2000] Majewska, A., Yiu, G. & Yuste, R. (2000). A custom-made two-photon microscope and deconvolution system. Pflugers Arch 441, 398–408.

[Marder & Bucher, 2001] Marder, E. & Bucher, D. (2001). Central pattern generators and the control of rhythmic movements. Curr Biol 11, R986–996.

[Matsuzaki et al., 2008] Matsuzaki, M., Ellis-Davies, G. C. & Kasai, H. (2008). Three-dimensional mapping of unitary synaptic connections by two-photon macro photolysis of caged glutamate. J Neurophysiol 99, 1535–1544.

[McCrea & Rybak, 2008] McCrea, D. A. & Rybak, I. A. (2008). Organization of mammalian locomotor rhythm and pattern generation. Brain Res Rev 57, 134–146.

[Mertz, 2005] Mertz, J. (2005). A practical guide: Building a two-photon laser-scanning microscope. In Imaging in Neuroscience and Development, (Yuste, R. & Konnerth, A., eds), pp. 71–74. Cold Spring Harbor Laboratory Press Cold Spring Harbor.

[Meyer-Luehmann et al., 2008] Meyer-Luehmann, M., Spires-Jones, T. L., Prada, C., Garcia-Alloza, M., de Calignon, A., Rozkalne, A., Koenigsknecht-Talboo, J., Holtzman, D. M., Bacskai, B. J. & Hyman, B. T. (2008). Rapid appearance and local

toxicity of amyloid-beta plaques in a mouse model of Alzheimer's disease. Nature 451, 720–724.

[Moreaux et al., 2000] Moreaux, L., Sandre, O. & Mertz, J. (2000). Membrane imaging by second-harmonic generation microscopy. J Opt Soc Am B 17, 1685–1694.

[Nishimura et al., 2007] Nishimura, N., Schaffer, C. B., Friedman, B., Lyden, P. D. & Kleinfeld, D. (2007). Penetrating arterioles are a bottleneck in the perfusion of neocortex. Proc Natl Acad Sci USA 104, 365–370.

[Oddo et al., 2003] Oddo, S., Caccamo, A., Shepherd, J. D., Murphy, M. P., Golde, T. E., Kayed, R., Metherate, R., Mattson, M. P., Akbari, Y. & LaFerla, F. M. (2003). Triple-transgenic model of Alzheimer's disease with plaques and tangles: intracellular Abeta and synaptic dysfunction. Neuron 39, 409–421.

[Oddo et al., 2006] Oddo, S., Vasilevko, V., Caccamo, A., Kitazawa, M., Cribbs, D. H. & LaFerla, F. M. (2006). Reduction of Abeta and tau, not soluable Abeta alone, ameliorates cognitive decline in transgenic mice with plaques and tangles. J Biol Chem 281, 39413–39423.

[Oheim et al., 2001] Oheim, M., Beaurepaire, E., Chaigneau, E., Mertz, J. & Charpak, S. (2001). Two-photon microscopy in brain tissue: parameters influencing the imaging depth. J Neurosci Methods 111, 29–37.

[Oron et al., 2005] Oron, D., Tal, E. & Silberberg, Y. (2005). Scanningless depth-resolved microscopy. Opt Express 13, 1468–1476.

[Ouzounov et al., 2002] Ouzounov, D. G., Moll, K. D., Foster, M. A., Zipfel, W. R., Webb, W. W. & Gaeta, A. L. (2002). Delivery of nanojoule femtosecond pulses through large-core microstructured fibers. Opt Lett 27, 1513–1515.

[Palero et al., 2006] Palero, J. A., de Bruijn, H. S., van der Ploeg-van den Heuvel, A., Sterenborg, H. J. & Gerritsen, H. C. (2006). In vivo nonlinear spectral imaging in mouse skin. Opt Express 14, 4395–4402.

[Piyawattanametha et al., 2006] Piyawattanametha, W., Barretto, R. P., Ko, T. H., Flusberg, B. A., Cocker, E. D., Ra, H., Lee, D., Solgaard, O. & Schnitzer, M. J. (2006). Fast-scanning two-photon fluorescence imaging based on a microelectromechanical systems two-dimensional scanning mirror. Opt Lett 31, 2018–2020.

[Poulet & Petersen, 2008] Poulet, J. F. A. & Petersen, C. C. H. (2008). Internal brain

state regulates membrane potential synchrony in barrel cortex of behaving mice. Nature 454, 881–885.

[Qiang et al., 2006] Qiang, L., Yu, W., Andreadis, A., Luo, M. & Baas, P. W. (2006). Tau protects microtubules in the axon from severing by katanin. J Neurosci 26, 3120–3129.

[Rakic et al., 1996] Rakic, P., Knyihar-Csillik, E. & Csillik, B. (1996). Polarity of microtubule assemblies during neuronal cell migration. Proc Natl Acad Sci USA 93, 9218–9222.

[Roberts, 1998] Roberts, A. (1998). Central circuits controlling locomotion in young frog tadpoles. Ann NY Acad Sci 860, 19–34.

[Rolls et al., 2007] Rolls, M. M., Satoh, D., Clyne, P. J., Henner, A. L., Uemura, T. & Doe, C. Q. (2007). Polarity and intracellular compartmentalization of Drosophila neurons. Neural Dev 2, 7.

[Roorda et al., 2004] Roorda, R., Hohl, T., Toledo-Crow, R. & Miesenbock, G. (2004). Video-rate nonlinear microscopy of neuronal membrane dynamics with genetically encoded probes. J Neurophysiol 92, 609–621.

[Rueckel et al., 2006] Rueckel, M., Mack-Bucher, J. A. & Denk, W. (2006). Adaptive wavefront correction in two-photon microscopy using coherence-gated wavefront sensing. Proc Natl Acad Sci USA 103, 17137–17142.

[Rybak et al., 2006a] Rybak, I. A., Shevtsova, N. A., Lafreniere-Roula, M. & McCrea, D. A. (2006a). Modelling spinal circuitry involved in locomotor pattern generation: insights from deletions during fictive locomotion. J Physiol 577, 617–639.

[Rybak et al., 2006b] Rybak, I. A., Stecina, K., Shevtsova, N. A. & McCrea, D. A. (2006b). Modelling spinal circuitry involved in locomotor pattern generation: insights from the effects of afferent stimulation. J Physiol 577, 641–658.

[Sabatini & Svoboda, 2000] Sabatini, B. & Svoboda, K. (2000). Analysis of calcium channels in single spines using optical fluctuation analysis. Nature 408, 589–593.

[Sacconi et al., 2006] Sacconi, L., Dombeck, D. A. & Webb, W. W. (2006). Overcoming photodamage in second-harmonic generation microscopy: Real-time optical recording of neuronal action potentials. Proc Natl Acad Sci USA 103, 3124–3129.

[Sakmann & Stuart, 1983] Sakmann, B. & Stuart, G. (1983). Patch-pipette recordings

from the soma, dendrites, and axon or neurons in brain slices. In Single-Channel Recording, 2nd ed., (Sakmann, B. & Neher, E., eds), pp. 199–211. Plenum Press New York.

[Sato et al., 2007] Sato, T. R., Gray, N. W., Mainen, Z. F. & Svoboda, K. (2007). The functional microarchitecture of the mouse barrel cortex. PLoS Biol 5, e189.

[Schaffer et al., 2006] Schaffer, C. B., Friedman, B., Nishimura, N., Schroeder, L. F., Tsai, P. S., Ebner, F. F., Lyden, P. D. & Kleinfeld, D. (2006). Two-photon imaging of cortical surface microvessels reveals a robust redistribution in blood flow after vascular occlusion. PLoS Biol 4, e22.

[Schwamborn et al., 2006] Schwamborn, J. C., Li, Y. & Puschel, A. W. (2006). GTPases and the control of neuronal polarity. Methods Enzymol 406, 715–727.

[Seitz et al., 2002] Seitz, A., Kojima, H., Oiwa, K., Mandelkow, E. M., Song, Y. H. & Mandelkow, E. (2002). Single-molecule investigation of the interference between kinesin, tau and MAP-2c. EMBO J 21, 4896–4905.

[Shemesh et al., 2008] Shemesh, O. A., Erez, H., Ginzburg, I. & Spira, M. E. (2008). Tau-induced traffic jam reflect organelles accumulation at points of microtubule polar mismatching. Traffic 9, 458–471.

[Shephard & Harris, 1998] Shephard, G. M. & Harris, K. M. (1998). Three-dimensional structure and composition of CA3-CA1 axons in rat hippocampal slices: implications for presynaptic connectivity and compartmentalization. J Neurosci 18, 8300–8310.

[Sillar, 1998] Sillar, K. T. (1998). Development and aminergic neuromodulation of a spinal locomotor network controlling swimming in Xenopus larvae. Ann NY Acad Sci 860, 318–332.

[Smith & Simmons, 2001] Smith, D. A. & Simmons, R. M. (2001). Models of motor-assisted transport of intracellular particles. Biophys J 80, 45–68.

[Spires et al., 2005] Spires, T. L., Meyer-Leuhmann, M., Stern, E. A., McLean, P. J., Skoch, J., Nguyen, P. T., Bacskai, B. J. & Hyman, B. T. (2005). Dendritic spine abnormalities in amyloid precursor protein transgenic mice demonstrated by gene transfer and intravital multiphoton microscopy. J Neurosci 25, 7278–7287.

[Spires-Jones et al., 2008] Spires-Jones, T. L., de Calignon, A., Matsui, T., Zehr, C., Pitstick, R., Wu, H.-Y., Osetek, J. D., Jones, P. B., Bacskai, B. J., Feany, M. B.,

Carlson, G. A., Ashe, K. H., Lewis, J. & Hyman, B. T. (2008). In vivo imaging reveals dissociation between caspase activation and acute neuronal death in tangle-bearing neurons. J Neurosci 28, 862–867.

[Stepanova et al., 2003] Stepanova, T., Slemmer, J., Hoogenraad, C. C., Lansbergen, G., Dortland, B., De Zeeuw, C. I., Grosveld, F., van Cappellen, G., Akhmanova, A. & Galjart, N. (2003). Visualization of microtubule growth in cultured neurons via the use of EB3-GFP (end-binding protein 3-green fluorescent protein). J Neurosci 23, 2655–2664.

[Steward & Worley, 2001] Steward, O. & Worley, P. F. (2001). Selective targeting of newly synthesized arc mrna to active synapses requires NMDA receptor activation. Neuron 30, 227–240.

[Stone et al., 2008] Stone, M. C., Roegiers, F. & Rolls, M. M. (2008). Microtubules have opposite orientation in axons and dendrites of Drosophila neurons. Mol Biol Cell 19, 4122–4129.

[Stosiek et al., 2003] Stosiek, C., Garaschuk, O., Holthoff, K. & Konnerth, A. (2003). In vivo two-photon calcium imaging of neuronal networks. Proc Natl Acad Sci USA 100, 7319–7324.

[Sutton & Schuman, 2006] Sutton, M. A. & Schuman, E. M. (2006). Dendritic protein synthesis, synaptic plasticity, and memory. Cell 127, 49–58.

[Svoboda et al., 1996] Svoboda, K., Tank, D. & Denk, W. (1996). Direct measurement of coupling between dendritic spines and shafts. Science 272, 716–719.

[Takahashi et al., 2007] Takahashi, D., Yu, W., Baas, P. W., Kawai-Hirai, R. & Hayashi, K. (2007). Rearrangement of microtubule polarity orientation during conversion of dendrites to axons in cultured pyramidal neurons. Cell Motil Cytoskel 64, 347–359.

[Takahashi et al., ress] Takahashi, R. H., Capetillo-Zarate, E., Lin, M. T., Milner, T. A. & Gouras, G. K. (2008 (in press)). Co-occurrence of Alzheimer's disease beta-amyloid and tau pathologies at synapses. Neurobiol Aging .

[Takahashi et al., 2002] Takahashi, R. H., Milner, T. A., Li, F., Nam, E. E., Edgar, M. A., Yamaguchi, H., Beal, M. F., Xu, H., Greengard, P. & Gouras, G. K. (2002). Intraneuronal Alzheimer Abeta42 accumulates in multivesicular bodies and is associated with synaptic pathology. Am J Pathol 161, 1869–1879.

[Takano et al., 2007] Takano, T., Han, X., Beane, R., Zlokovic, B. & Nedergaard, M.

(2007). Two-photon imaging of astrocytic Ca2+ signaling and the microvasculature in experimental mice models of Alzheimer's disease. Ann NY Acad Sci 1097, 40–50.

[Tallini et al., 2006] Tallini, Y. N., Ohkura, M., Choi, B. R., Ji, G., Imoto, K., Doran, R., Lee, J., Plan, P., Wilson, J., Xin, H. B., Sanbe, A., Gulick, J., Mathai, J., Robbins, J., Salama, G., Nakai, J. & Kotlikoff, M. I. (2006). Imaging cellular signals in the heart in vivo: Cardiac expression of the high-signal Ca2+ indicator GCaMP2. Proc Natl Acad Sci USA 103, 4753–4758.

[Thal et al., 2002] Thal, D. R., Ghebremedhin, E., Haass, C. & Schultz, C. (2002). UV light-induced autofluorescence of full-length Abeta-protein deposits in the human brain. Clin Neuropathol 21, 35–40.

[Thaler et al., 1999] Thaler, J., Harrison, K., Sharma, K., Lettieri, K., Kehrl, J. & Pfaff, S. L. (1999). Active suppression of interneuron programs within developing motor neurons revealed by analysis of homeodomain factor Hb9. Neuron 23, 675–697.

[Theer et al., 2003] Theer, P., Hasan, M. T. & Denk, W. (2003). Two-photon imaging to a depth of 1000 micron in living brains by use of a Ti:Al2O3 regenerative amplifier. Opt Lett 28, 1022–1024.

[Trachtenberg et al., 2002] Trachtenberg, J. T., Chen, B. E., Knott, G. W., Feng, G., Sanes, J. R., Welker, E. & Svoboda, K. (2002). Long-term in vivo imaging of experience-dependent synaptic plasticity in adult cortex. Nature 420, 788–794.

[Tsai et al., 2004] Tsai, J., Grutzendler, J., Duff, K. & Gan, W. B. (2004). Fibrillar amyloid deposition leads to local synaptic abnormalities and breakage of neuronal branches. Nat Neurosci 7, 1181–1183.

[Tsai et al., 2002] Tsai, P. S., Nishimura, N., Yoder, E. J., White, E. D. & Kleinfeld, D. (2002). Principles, design, and construction of a two-photon laser scanning microscope for in vitro and in vivo brain imaging. In Methods for In Vivo Optical Imaging, (Frostig, R., ed.), pp. 113–171. CRC Press New York.

[Tsien, 1999] Tsien, R. Y. (1999). Monitoring cell calcium. In Calcium as a Cellular Regulator, (Carafoli, E. & Klee, C., eds), pp. 28–54. Oxford University Press New York.

[Vale, 1996] Vale, R. D. (1996). Direct observation of single kinesin molecules moving along microtubules. Nature 380, 451–453.

[Vale, 2003] Vale, R. D. (2003). The molecular motor toolbox for intracellular transport. Cell 112, 467–480.

[Vishwasrao et al., 2005] Vishwasrao, H. D., Heikal, A. A., Kasischke, K. A. & Webb, W. W. (2005). Conformational dependence of intracellular NADH on metabolic state revealed by associated fluorescence anisotropy. J Biol Chem 280, 25119–25126.

[Vucinic & Sejnowski, 2007] Vucinic, D. & Sejnowski, T. J. (2007). A compact multiphoton 3D imaging system for recording fast neuronal activity. PLoS ONE 2, e699.

[Wachowiak & Cohen, 2001] Wachowiak, M. & Cohen, L. B. (2001). Representation of odorants by receptor neuron input to the mouse olfactory bulb. Neuron 32, 723–735.

[Wallace et al., 2008] Wallace, D. J., Borgloh, S. M., Astori, S., Yang, Y., Bausen, M., Kugler, S., Palmer, A. E., Tsien, R. Y., Sprengel, R., Kerr, J. N., Denk, W. & Hasan, M. T. (2008). Single-spike detection in vitro and in vivo with a genetic Ca2+ sensor. Nat Methods 5, 797–804.

[Whelan et al., 2000] Whelan, P., Bonnot, A. & O'Donovan, M. J. (2000). Properties of rhythmic activity generated by the isolated spinal cord of the neonatal mouse. J Neurophysiol 84, 2821–2833.

[Wichterle et al., 2002] Wichterle, H., Lieberam, I., Porter, J. A. & Jessell, T. M. (2002). Directed differentiation of embryonic stem cells into motor neurons. Cell 110, 385–397.

[Williams et al., 2005] Williams, R. M., Zipfel, W. R. & Webb, W. W. (2005). Interpreting second-harmonic generation images of collagen I fibrils. Biophys J 88, 1377–1386.

[Wilson & Brownstone, 2008] Wilson, J. M. & Brownstone, R. M. (2008). Hb9 interneurons: reply to Ziskind-Conhaim and Hinckley. J Neurophysiol 99, 1047–1049.

[Wilson et al., 2007a] Wilson, J. M., Cowan, A. I. & Brownstone, R. M. (2007a). Conditional rhythmicity of ventral spinal interneurons defined by expression of the Hb9 homeodomain protein. J Neurophysiol 98, 2370–2381.

[Wilson et al., 2007b] Wilson, J. M., Dombeck, D. A., Diaz-Rios, M., Harris-Warrick, R. M. & Brownstone, R. M. (2007b). Two-photon calcium imaging of network activity in XFP-expressing neurons in the mouse. J Neurophysiol 97, 3118–3125.

[Wilson et al., 2005] Wilson, J. M., Hartley, R., Maxwell, D. J., Todd, A. J., Lieberam, I., Kaltschmidt, J. A., Yoshida, Y. & Jessell, T. M. (2005). Conditional rhythmicity of ventral spinal interneurons defined by expression of the Hb9 homeodomain protein. J Neurosci 25, 5710–5719.

[Wise, 2005] Wise, F. (2005). Lasers for multiphoton microscopy. In Imaging in Neuroscience and Development, (Yuste, R. & Konnerth, A., eds), pp. 775–781. Cold Spring Harbor Laboratory Press Cold Spring Harbor.

[Yaksi & Friedrich, 2006] Yaksi, E. & Friedrich, R. W. (2006). Reconstruction of firing rate changes across neuronal populations by temporally deconvolved Ca2+ imaging. Nat Methods 3, 377–383.

[Zar, 1994] Zar, J. H. (1994). Biostatistical Analysis. Prentice-Hall, Englewood Cliffs, NJ.

[Zhong et al., 2007] Zhong, G., Masino, M. A. & Harris-Warrick, R. M. (2007). Persistent sodium currents participate in fictive locomotion generation in neonatal mouse spinal cord. J Neurosci 27, 4507–4518.

[Zhu et al., 2008] Zhu, C., Breslin, T. M., Harter, J. & Ramanujam, N. (2008). Model based and empirical spectral analysis for the diagnosis of breast cancer. Opt Express 16, 14961–14978.

[Zipfel et al., 2003a] Zipfel, W. R., Williams, R. M., Christie, R., Nikitin, A. Y., Hyman, B. T. & Webb, W. W. (2003a). Live tissue intrinsic emission microscopy using multiphoton-excited native fluorescence and second-harmonic generation. Proc Natl Acad Sci USA 100, 7075–7080.

[Zipfel et al., 2003b] Zipfel, W. R., Williams, R. M. & Webb, W. W. (2003b). Nonlinear magic: Multiphoton microscopy in the biosciences. Nat Biotechnol 21, 1369–1377.

[Ziskind-Conhaim & Hinckley, 2008] Ziskind-Conhaim, L. & Hinckley, C. A. (2008). Hb9 versus type 2 interneurons. J Neurophysiol 99, 1044–1046.

[Ziskind-Conhaim et al., 2008] Ziskind-Conhaim, L., Wu, L. & Wiesner, E. P. (2008). Persistent sodium current contributes to induced voltage oscillations in locomotor-related Hb9 interneurons in the mouse spinal cord. J Neurophysiol 100, 2254–2264.